



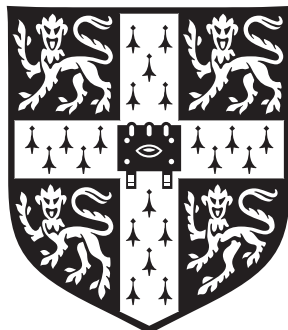
EXPLORING GRAVITY

WITH GRAVITATIONAL WAVES & STRONG-FIELD TESTS



Christopher P. L. Berry

Churchill College and Institute of Astronomy
UNIVERSITY OF CAMBRIDGE



This dissertation is submitted for the degree of
DOCTOR OF PHILOSOPHY

Supervisor: Jonathan R. Gair

18th July 2013

Declaration

This dissertation is the result of my own work and includes nothing which is the outcome of work done in collaboration, except where specifically indicated in the text. All concepts, results and data obtained by others are properly referenced. I have profited from discussion with and suggestions from a number of colleagues who are thanked in the acknowledgements. The use of “we” in the main text reflects my stylistic preference and nothing more.

This dissertation is not substantially the same as any that has been submitted for another degree, diploma or similar qualification. However, many of the results presented have been published as journal articles. Theses are:

Berry, C.P.L. & Gair, J.R.; Gravitational wave energy spectrum of a parabolic encounter; *Physical Review D*; **82**(10):107501(4); November 2010;
[arXiv:1010.3865 \[gr-qc\]](https://arxiv.org/abs/1010.3865)

which includes work included in section 2.5;

Berry, C.P.L. & Gair, J.R.; Linearized $f(R)$ gravity: Gravitational radiation and Solar System tests; *Physical Review D*; **83**(10):104022(19); May 2011;
[arXiv:1104.0819 \[gr-qc\]](https://arxiv.org/abs/1104.0819)

which includes work included in chapters 5 and 6;

Berry, C.P.L. & Gair, J.R.; Observing the Galaxy’s massive black hole with gravitational wave bursts; *Monthly Notices of the Royal Astronomical Society*; **429**(1):589–612; February 2013; [arXiv:1210.2778 \[astro-ph.HE\]](https://arxiv.org/abs/1210.2778)

which includes work included in chapters 2 and 3, and

Berry, C.P.L. & Gair, J.R.; Extreme-mass-ratio-bursts from extragalactic sources; *Monthly Notices of the Royal Astronomical Society*;
[arXiv:1306.0774 \[astro-ph.HE\]](https://arxiv.org/abs/1306.0774)

which includes work included in section 3.3.1.1 and chapter 4. Explicit citation to any of these indicates work done in collaboration. This is done in section 2.5.2, where the original derivation of equation (2.54) is due Jonathan Gair and I subsequently verified

this (correcting a minus sign and a factor of $\sqrt{2}$); in section 6.2, where the calculation of the epicyclic frequencies was done by Jonathan Gair, generalising an earlier result of mine for the non-spinning metric, and I checked this (again fixing a minus sign), and in section 6.2.1, where the gravitational wave constraints were calculated using code developed by Jonathan Gair.

This dissertation contains fewer than 60000 words.

Conventions

Throughout this work we will use the time-like sign convention of Landau & Lifshitz (1975):

1. The metric has signature $(+,-,-,-)$.
2. The Riemann tensor is defined as $R^{\mu}_{\nu\sigma\rho} = \partial_{\sigma}\Gamma^{\mu}_{\nu\rho} - \partial_{\rho}\Gamma^{\mu}_{\nu\sigma} + \Gamma^{\mu}_{\lambda\sigma}\Gamma^{\lambda}_{\rho\nu} - \Gamma^{\mu}_{\lambda\rho}\Gamma^{\lambda}_{\sigma\nu}$.
3. The Ricci tensor is defined as the contraction $R_{\mu\nu} = R^{\lambda}_{\mu\lambda\nu}$.

Greek indices are used to represent spacetime indices $\mu = \{0, 1, 2, 3\}$ (or $\mu = \{t, \tilde{r}, \theta, \phi\}$) and lowercase Latin indices are used for spatial indices $i = \{1, 2, 3\}$. Uppercase Latin indices from the beginning of the alphabet are used to label detectors: $A = \{\text{I}, \text{II}\}$ for *LISA*, which has three arms and acts as two detectors, and $A = \{\text{I}\}$ for *eLISA*, which has only two arms and so acts as a single detector. Lowercase Latin indices from the beginning of the alphabet are used for parameter space. Summation over repeated indices is assumed unless explicitly noted otherwise. In general, factors of the speed of light c and gravitational constant G are retained, except where explicitly noted.

Contents

Conventions	v
I Introduction	1
1 Gravitation and astrophysics	3
1.1 What goes up	3
1.1.1 Newton	3
1.1.2 Einstein	4
1.1.3 This work	5
1.2 Strong-field tests and gravitational waves	5
1.2.1 Field strength and existing tests	5
1.2.2 Gravitational radiation	7
1.3 Astrophysical compact objects	12
1.3.1 White dwarfs and neutron stars	12
1.3.2 Black holes	13
1.4 Modified gravity	16
II Astronomical systems	19
2 Extreme-mass-ratio burst waveforms	21
2.1 Massive black holes and extreme-mass-ratio events	21
2.2 Parabolic orbits in Kerr spacetime	22
2.2.1 The metric and geodesic equations	22
2.2.2 Integration variables and turning points	24
2.3 Waveform construction	25
2.3.1 The kludge approximation	25
2.3.2 The quadrupole–octupole formula	26
2.4 Signal detection and analysis	27
2.4.1 The LISA detector	27
2.4.2 Frequency domain formalism	28

2.4.3	The noise curve	29
2.4.4	Window functions	29
2.5	Energy spectra	30
2.5.1	Kludge spectrum	30
2.5.2	Peters and Mathews spectrum	31
2.5.3	Comparison	34
2.6	Summary	38
3	Parameter estimation and Galactic bursts	39
3.1	Waveforms and detectability	39
3.1.1	Model parameters	39
3.1.2	Waveforms and kludge coordinates	41
3.1.3	Signal-to-noise ratios	43
3.2	Parameter estimation	44
3.2.1	Fisher matrices	45
3.2.2	Markov chain Monte Carlo methods	47
3.3	Results for Galactic bursts	49
3.3.1	Distribution widths	50
3.3.2	Scientific potential	57
3.4	Summary and conclusions	59
4	Extragalactic bursts	61
4.1	Detectability of extragalactic bursts	61
4.2	Parameter estimation using extragalactic bursts	67
4.2.1	Parameter inference	67
4.2.2	Mapping the posterior distribution	68
4.2.3	Parameter uncertainties	70
4.3	Summary and conclusions	73
III	Understanding gravitation	75
5	Gravitational radiation in $f(R)$-gravity	77
5.1	Beyond general relativity: $f(R)$ modified gravity	77
5.2	Description of $f(R)$ -gravity	78
5.2.1	The action and field equations	78
5.2.2	Conservation of energy-momentum	81
5.3	Linearised theory	81
5.4	Gravitational radiation	84
5.5	Energy-momentum tensor	86
5.6	Summary	90

6 Observational constraints for $f(R)$-gravity	91
6.1 $f(R)$ -gravity with a source	91
6.1.1 The Newtonian limit	92
6.1.2 The weak-field metric	94
6.2 Epicyclic frequencies	95
6.2.1 Gravitational wave constraints	97
6.3 Solar System and laboratory tests	99
6.3.1 Light bending and the post-Newtonian parameter γ	99
6.3.2 Planetary precession	101
6.3.3 Fifth-force tests	103
6.4 Discussion of $f(R)$ -gravity	104
IV Conclusion	107
V Appendices	109
A The signal inner product	111
A.1 Preliminaries	111
A.1.1 The Fourier transform	111
A.1.2 The Wiener–Khinchin theorem	111
A.2 Defining the inner product	112
A.2.1 Gaussian noise	112
A.2.2 Noise power spectral density	114
B Windowing and Fourier analysis	115
B.1 Spectral leakage	115
B.2 Window functions	116
B.3 Influence on results	118
C Semirelatativistic fluxes	121
D The loss cone	129
References	133

Part I

Introduction

Chapter 1

Gravitation and astrophysics

1.1 What goes up...

1.1.1 Newton

Gravity is one of the fundamental forces of nature; familiar as the force that keeps the Earth in orbit about the Sun and makes falling off a log so easy. Newton (1999, book 3) was the first to realise that gravitation could explain both apples falling from trees and the motion of astronomical bodies. In the *Principia*, first published in 1687, he outlined a gravitational force that scaled as the inverse of the square of the distance between centres of mass and was proportional to the product of the masses of the bodies. In modern notation, the force is

$$F = \frac{Gm_1m_2}{r^2}, \quad (1.1)$$

for distance r , masses m_1 and m_2 , and gravitational constant G . This theory has been hugely successful. Not only is it still taught in schools today, but it is also used for astronomical research. Newton's law of universal gravitation has proved accurate in describing orbital motions. However, there have been observations that did not fit its predictions.

In the early nineteenth century, the motion of Uranus was found to deviate from its expected trajectory. Rather than seeking to modify the theory, Le Verrier (1846, *troisième partie*) and Adams (1896, papers 1 and 2) calculated the properties of a perturbing object that could explain the motion. They predicted the existence of an unseen mass, a new planet; this was subsequently observed within a degree of Le Verrier's hypothesised position (Le Verrier 1846, *cinquième partie*) and became known as Neptune.

Newtonian gravity survived the trial of Uranus' orbit, but it could not explain the perihelion precession of Mercury. Le Verrier (1859, *chapitre XV, section quatrième*) first noticed the anomaly. A new inner planet was suggested, but this time it could not be found. What was needed was a modified theory of gravitation: the Newtonian theory is insufficient in the stronger gravity close to the Sun (Einstein 1997, document 24).

1.1.2 Einstein

The new extended theory was General Relativity (GR), developed by Einstein in the 1910s (Einstein 1997). This describes gravity as the effect of the curvature of spacetime, which is now a dynamical entity. Particles naturally travel along geodesics of spacetime, which may appear curved; the curvature of spacetime itself is sourced from the energy-momentum it contains: matter tells spacetime how to curve, and spacetime tells matter how to move (Misner *et al.* 1973, section 1.1). This is encapsulated within the Einstein field equations (Einstein 1997, documents 22 and 25)

$$R_{\mu\nu} - \frac{1}{2}Rg_{\mu\nu} = \frac{8\pi G}{c^4}T_{\mu\nu}, \quad (1.2)$$

where $g_{\mu\nu}$ is the metric, $R_{\mu\nu}$ and R are the Ricci tensor and scalar (Misner *et al.* 1973, section 8.7; Wald 1984, section 3.2), c is the speed of light, and $T_{\mu\nu}$ is the energy-momentum tensor. GR reduces to its Newtonian counter-part in the weak-field limit, or conversely, it extends Newtonian gravity to stronger gravitational fields.

Since its inception, GR has successfully passed every observational test (Will 1993, 2006). However, astronomers have not been idle, and the twentieth century has yielded further surprises.

Observations of the velocity dispersions of galaxies in clusters are higher than those calculated from the quantity of luminous matter (e.g., Zwicky 1937). Similarly, measurements of the rotation curves of galaxies do not match the expected profile (Babcock 1939). Gravitational lensing of galaxy clusters confirms that their gravity is dominated by an unseen component (Bergmann *et al.* 1990; Clowe *et al.* 2006). This has been interpreted as motivation for introducing dark matter, a new component of the Universe that gravitates but does not interact with electromagnetic (EM) radiation. Dark matter has become central to our understanding of cosmology (e.g., Springel *et al.* 2006); it is needed to explain structure formation: without it we could not form galaxies from the small over-densities inferred from the homogeneity of the cosmic microwave background (CMB; White & Rees 1978; Liddle & Lyth 1993). Although we know the properties required of dark matter and we can estimate the required quantity, we do not have a definite candidate for a dark matter particle (Bertone *et al.* 2005). Its true nature remains a mystery.

Observations of type IA supernovae have revealed that the Universe is not only expanding, but is accelerating (Riess *et al.* 1998; Perlmutter *et al.* 1999a). This acceleration has been attributed to the influence of dark energy (Perlmutter *et al.* 1999b; Peebles & Ratra 2003). The nature of dark energy is even more mysterious than that of dark matter. The simplest explanation is to introduce a cosmological constant Λ ; this modifies the Einstein field equations to become (Einstein 1997, document 43)

$$R_{\mu\nu} - \frac{1}{2}Rg_{\mu\nu} - \Lambda g_{\mu\nu} = \frac{8\pi G}{c^4}T_{\mu\nu}. \quad (1.3)$$

This model has been highly successful in explaining the evolution of the Universe, but we still do not know if a cosmological constant is the true explanation and if so, why it has its particular value (Carroll 2001).

Despite its long history, we still do not know everything about gravity. There are still discoveries to be made. Gravity is the weakest of the fundamental forces and so is difficult to study in the laboratory. Yet it dominates on astronomical scales; understanding gravity is crucial to understanding the cosmos. We have learnt much about the workings of the Universe through improving our understanding of gravity, and the motivation for developing new theories of gravitation has often come from astronomical observations. Gravitation and astrophysics are intimately linked.

1.1.3 This work

This thesis is divided into two strands. The first is concerned with what we could learn about astrophysical systems from gravitational probes; the second is concerned with what we can learn about gravity from astronomical observations. We shall consider strong-field tests and, in particular, gravitational waves (GWs). The former part concentrates on what we could hope to learn about massive black holes (MBHs) and their surrounding stellar environment from extreme-mass-ratio bursts (EMRBs). The latter looks at modifications to gravity in the metric $f(R)$ theory.

1.2 Strong-field tests and gravitational waves

The deviations from Newtonian theory were first noted in the gravitational field close to the Sun, the strongest accessible in the Solar System. GR has now been tested in stronger fields (Will 2006), but there are still more extreme systems to be explored. It is here that we expect any deviations to manifest. We know that our understanding of GR in the strongest fields is, at least, incomplete, as black holes (BHs) feature singularities at their centres, where the theory breaks down (Misner *et al.* 1973, section 34.6; Wald 1984, chapter 9). Even if we do not find any deviations from GR, it is still worthwhile to check its validity, if only as a matter of scientific principle.

1.2.1 Field strength and existing tests

In order to parametrize the strength of gravity, Psaltis (2008) introduces two characteristic quantities: the dimensionless potential or compactness (Yunes & Siemens 2013)

$$\varepsilon = \frac{GM}{rc^2}, \quad (1.4)$$

and the dimensionful curvature

$$\xi = \frac{GM}{r^3 c^2}, \quad (1.5)$$

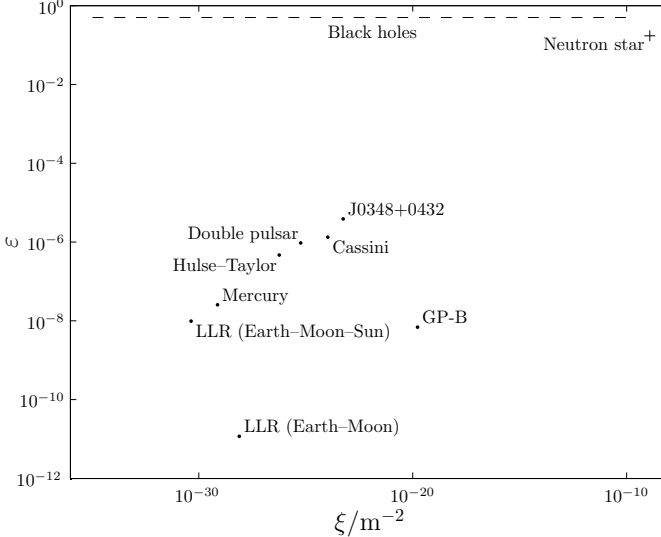


Figure 1.1 Astrophysical tests of GR parametrised by the compactness and curvature scales they probe, adapted from Psaltis (2008). The dashed line indicates the Schwarzschild radius $r_S = 2GM/c^2$ for BHs of mass $5\text{--}10^7 M_\odot$ and the cross indicates the surface of a NS.

where M is the gravitating mass and r a characteristic distance. These are larger for stronger fields. The potential ranges from $\varepsilon \simeq 0$ in weak fields to $\varepsilon \sim \mathcal{O}(1)$ near the surface of a neutron star (NS) or a BH event horizon. It is useful in defining post-Newtonian expansions. The curvature ξ approximates the form of the Ricci scalar, which is fundamental to GR. It is necessary to pick a particular reference scale to define when the curvature becomes large; however, it is a useful gauge of the strength of a gravitational field in a geometric theory because it is the lowest order measure that cannot be eliminated by a coordinate transformation (Hobson *et al.* 2006, chapter 7).

Using these two parameters, we can map out the possible tests of GR. Figure 1.1 shows a selection of current astrophysical tests. Included are:

- The classic perihelion precession of Mercury (Hobson *et al.* 2006, section 10.2; Will 1993, section 7.3; Pitjeva 2009);
- Doppler tracking of the Cassini spacecraft (Bertotti *et al.* 2003) which measures the time delay of light travelling passed the Sun (Will 1993, section 7.2);
- Lunar laser ranging (LLR; Bender *et al.* 1973; Williams *et al.* 2012) which provides precise measurements of the orbits of the Earth–Moon and Earth–Moon–Sun systems (Will 1993, section 8.1);
- Gravity Probe B (GP-B; Everitt *et al.* 2009, 2011) which produced measurements of the geodetic drift and frame-dragging (Will 1993, section 9.1);
- A selection of binary pulsars (Taylor 1993; Stairs 2003), specifically the Hulse–Taylor binary (PSR B1913+16; Hulse & Taylor 1975; Weisberg *et al.* 2010), which

was the first discovered and the first system to show the influence of GWs; PSR J0348+0432 (Antoniadis *et al.* 2013) which includes a $2M_{\odot}$ pulsar, and the double pulsar system (Breton *et al.* 2008; Kramer & Stairs 2008).

For comparison, we have also plotted the parameters for the surface of a neutron star and the Schwarzschild radius of BHs of various masses. BHs range in mass from a few M_{\odot} (Özel *et al.* 2010) to several billion M_{\odot} (Hlavacek-Larrondo *et al.* 2012), although, for clarity, we have only plotted up to $10^7 M_{\odot}$. To probe the strongest fields, we need a way of probing the spacetime of compact objects (COs) like NSs and BHs.

In addition to the astrophysical tests of gravity, it is possible to make precision tests in the laboratory (Kapner *et al.* 2007; Adelberger *et al.* 2009; Wagner *et al.* 2012). Whilst these are limited to using small masses, they do allow careful control of the system that is not possible in astronomy. Neither the astrophysical nor the laboratory tests performed so far show any discrepancy from the predictions of GR (Will 2006).

1.2.2 Gravitational radiation

One particularly promising method of exploring strong-field regions would be to observe GWs. These are predicted in any relativistic theory of gravity, where changes in the gravitational field must propagate at finite speed (Schutz 1984). Within GR they are tiny ripples in the spacetime metric (Misner *et al.* 1973, section 35.1; Landau & Lifshitz 1975, section 107). They are generated by systems with a time-varying mass quadrupole; significant gravitational radiation originates from regions where spacetime is highly dynamic and the objects are extremely relativistic. This is precisely the strong-field domain we are interested in investigating.

Some intuition about GWs can be obtained from the more familiar EM waves (Landau & Lifshitz 1975, sections 46–48 and 66–67; Jackson 1999, sections 7.1 and 9.1–9.3). These are oscillations of the electric and magnetic fields produced by accelerating charges whilst GWs are oscillations of the spacetime metric produced by accelerating masses. EM waves may be sourced by a time-varying charge dipole; as a consequence of conservation of momentum there is no time-varying mass dipole, so GWs are sourced by the mass quadrupole (Hobson *et al.* 2006, section 18.5; Rindler 2006, section 15.4). Both waves propagate at the speed of light and have two (transverse) polarizations: for GWs these represent two orthogonal patterns of stretching and squeezing as shown in figure 1.2 (Dirac 1996, section 34; Hobson *et al.* 2006, section 18.4)

Visible light has been used by astronomers for millennia. In the twentieth century, the useful spectrum was extended through infrared to radio, and from ultraviolet to X-rays and gamma rays (Longair 2006, chapter 7). In the twenty-first century, we hope to move from EM to gravitational radiation. GWs encode valuable information about their sources, information that is accessible by other means.

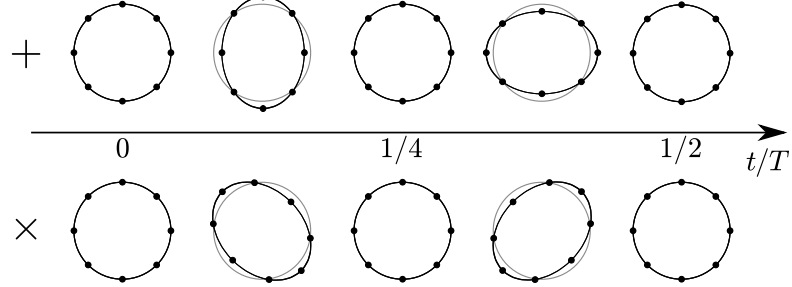


Figure 1.2 The effect the two GW polarizations (plus + and cross \times) on a ring of free particles as a function of time. The propagation direction is perpendicular to the ring. The wave period is T .

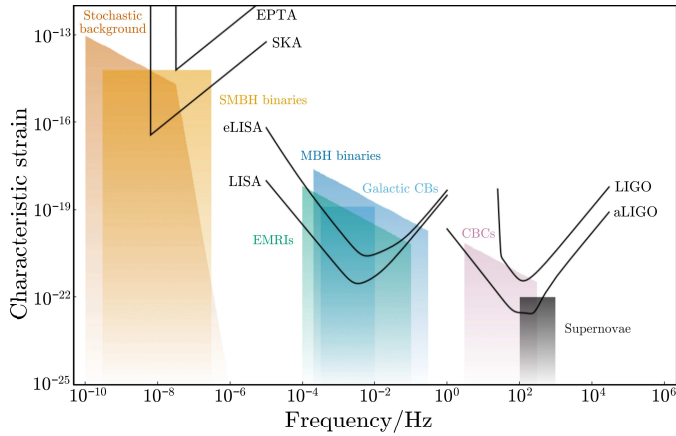


Figure 1.3 The spectrum of GWs. Sources (see section 1.2.2.2) are indicated by their characteristic amplitude as measured on Earth, detectors (see section 1.2.2.1) are characterised by their sensitivity curves. Adapted from <http://www.ast.cam.ac.uk/~rhc26/sources/>.

Just like EM waves, GWs come in a range of frequencies. The frequency is set by the scale of the source system: typically more massive objects have longer associated time-scales and so produce lower frequency radiation. Figure 1.3 show the GW spectrum with illustrative detectors and sources. Detectors are sensitive to specific frequency bands, the range of which is set by their size. The spectrum may be divided into: the extremely low frequency (ELF; not shown in the figure) regime, $\sim 10^{-18}\text{--}10^{-15}$ Hz, which may indirectly detected through observations of the polarization of the CMB (e.g., Hu & White 1997; Kamionkowski & Stebbins 1997); the very low frequency (VLF) regime, $\sim 10^{-9}\text{--}10^{-6}$ Hz, which is accessible to pulsar timing arrays (PTAs); the low frequency (LF) regime, $\sim 10^{-6}\text{--}1$ Hz, which could be measured by space-borne detectors, and the high frequency (HF) regime, $\sim 1\text{--}10^4$ Hz, which is the target range for ground-based detectors. Individual detectors are discussed in section 1.2.2.1 and some example sources are introduced in section 1.2.2.2.

While GWs are an exciting source of information, it will be beneficial to compare

with results from other techniques, to maximise the data available for inferences, and to check models. For example, very long baseline interferometry (VLBI) may be used to image the vicinity of a BH’s horizon, or X-ray observations could be used to investigate BH accretion discs (Psaltis *et al.* 2008).

1.2.2.1 Gravitational wave detection

As yet no GWs have been directly detected, although their existence has been inferred from the loss of energy and angular momentum from binary pulsars (Stairs 2003). ... There are a number of experiments designed to directly observe GWs (Riles 2013). Modern detectors attempt to measure the minute changes in distance induced by a passing GW (Thorne 1987, section 9.5; Hobson *et al.* 2006, section 18.9). The amplitude of a GW is characterised by a strain: the fractional change in length resulting from the perturbation from the background spacetime.

The Laser Interferometer Gravitational-wave Observatory (LIGO; Abramovici *et al.* 1992) and the European Gravitational Observatory’s Virgo detector (Acernese *et al.* 2008), which work in collaboration, are currently being upgraded to their advanced configurations (aLIGO and aVirgo) and are expected to make the first detection shortly after recommencing operation around 2015 (Harry 2010; Accadia *et al.* 2011).¹ These are ground-based interferometers that detect passing GWs by measuring the induced difference in the length of their two arms (Pitkin *et al.* 2011). They are sensitive to frequencies in the range $\sim 10\text{--}10^4$ Hz, with peak sensitivity at about 100 Hz. The LIGO and Virgo detectors are supported by GEO 600, a smaller interferometric experiment that incorporates prototype technologies (Willke *et al.* 2002, 2006). LIGO has two sites, one in Hanford, Washington and one in Livingston, Louisiana. The Hanford observatory has two detectors, one half the arm-length of the other. There is an agreement to move the smaller detector to a location in India (Unnikrishnan 2013). The LIGO-India detector, operated by the Indian Initiative in Gravitational Observations (IndIGO), will provide a longer baseline between detectors, giving improved sky location and sky coverage (Schutz 2011).

A further ground-based interferometer is under construction in Japan. The Kamioka Gravitational Wave Detector (KAGRA), formerly the Large-scale Cryogenic Gravitational Wave Telescope (LCGT; Kuroda *et al.* 1999; Kuroda 2010) will operate underground in the Kamioka mine. It lags several years behind the other detectors, aiming to start observations in 2017–2018, but will employ more sophisticated noise-reduction techniques such as cryogenic cooling (Somiya 2012).

Ground-based GW astronomy may eventually be continued by the construction of the Einstein Telescope, an ambitious idea to construct an underground detector with 10 km

¹An optimistic hope is to celebrate the centenary of Einstein’s 1916 prediction of gravitation waves (Einstein 1997, document 32) with the first direct detection.

arms (Punturo *et al.* 2010; Hild *et al.* 2011; Sathyaprakash *et al.* 2012). Its location would provide shielding from seismic noise, allowing it to observe frequencies 10– 10^4 Hz. There is no definite time-line for this concept.

There is another contender for the first detection: pulsar timing arrays (McWilliams *et al.* 2012; Sesana 2013b). These infer the presence of a GW from periodic delays in the arrival times of the highly regular millisecond pulses. In effect, the pulsars are used to create a detector with galactic-scale arms (Hellings & Downs 1983). They are sensitive to frequencies of $\sim 10^{-9}$ – 10^{-7} Hz. An international collaboration of European, North American and Australian radio telescopes is already in possession of the necessary instruments to detect GWs (Hobbs *et al.* 2010).² The completion of the Square Kilometre Array (SKA; Dewdney *et al.* 2009) shall augment the search, greatly increasing sensitivity (Kramer *et al.* 2004).

Between the HF range of the ground-based detectors and the VLF range of pulsar timing, lies a band that could be accessible to space-based interferometers. These are not limited by seismic noise and are free to have much longer arms than the ground-based detectors, making them sensitive to low frequencies. The paradigm detector is the Laser Interferometer Space Antenna (LISA; Bender *et al.* 1998; Danzmann & Rüdiger 2003). This is a constellation of three satellites in a circular, heliocentric orbit forming a three-armed interferometer. Each arm is 5×10^9 m, and the orbit trails 20° behind the Earth. The detector is sensitive to a range of frequencies $\sim 10^{-5}$ – 1 Hz, having peak sensitivity around 10^{-3} – 10^{-2} Hz.

LISA developed as a joint NASA–ESA mission. In 2011 NASA withdrew for financial reasons leaving ESA to investigate reduced cost missions. The resulting descoped concept is the evolved Laser Interferometer Space Antenna (eLISA; Jennrich *et al.* 2011; Amaro-Seoane *et al.* 2012).³ This shares the same basic components as LISA but only has two arms and lags 9° behind the Earth. The arms are 1×10^9 m; this shifts the peak sensitivity to marginally higher frequencies, around 10^{-2} Hz. Overall the noise curve is raised relative to LISA giving eLISA reduced sensitivity.

At the time of writing, there is no currently funded mission. However, LISA Pathfinder, a technology demonstration mission, is due for launch in 2015 (Anza *et al.* 2005; Antonucci *et al.* 2012). Hopefully, a full mission shall follow in the subsequent decade.⁴

In addition to the LISA family, there are other proposed space-borne detectors. The Japanese Deci-hertz Interferometer Gravitational Wave Observatory (DECIGO; Kawamura *et al.* 2006, 2011) consists of constellations of satellites similar to LISA, but

²The International Pulsar Timing Array (IPTA) consortium consists of the European Pulsar Timing Array (EPTA), the North American Nanohertz Observatory for Gravitational Waves (NANOGrav) and the Parkes Pulsar Timing Array (PPTA) consortia.

³This was submitted to the ESA for their L1 mission selection as the New Gravitational-wave Observatory (NGO).

⁴At the time of writing a science theme has been submitted to ESA for their L2/3 mission selection.

with arms of 100 km. It will fill the gap between the LISA family and the ground-based detectors, being most sensitive to frequencies 0.1–10 Hz. DECIGO is imagined for launch in 2027, pending the success of two pathfinder missions (Ando *et al.* 2010).

There have even been suggestions for successors to LISA (Crowder & Cornish 2005). The Advanced Laser Interferometer Antenna (ALIA) and the Big Bang Observer (BBO) are both popular concepts. Compared to the LISA family, they have shorter arms, making them sensitive to higher frequencies, and better sensitivities. They may be more comparable to DECIGO Yagi & Seto (2011). These designs are highly speculative.

1.2.2.2 Gravitational wave sources

GWs can be emitted by a variety of systems. To produce detectable signals the source must consist of extremely massive objects moving at a significant fraction of the speed of light. The quintessential source is a binary. These inspiral as a result of GW emission and eventually merge. There is a wide range of binary systems, examples include:

- Compact binaries (CBs) made up of two closely-orbiting stellar-mass COs, most commonly white dwarfs (WDs). These are the end result of the stellar evolution of a binary star system (Postnov & Yungelson 2006). Wider CBs in the Galaxy are a source for space-borne detectors. These are so common in that some may form an unresolvable foreground (Nelemans 2009); others would be guaranteed sources allowing us to verify the functionality of the detector (Stroeer & Vecchio 2006). At the end of their inspiral, the system merges in a CB coalescence (CBC). This produces a target signal for ground-based detectors (Abadie *et al.* 2010) as well as a potential EM counterpart (Webbink 1984; Iben, Jr. & Tutukov 1984; Metzger *et al.* 2010; Rezzolla *et al.* 2011; Nakar & Piran 2011, e.g.). Observations of CBs will help us to understand stellar evolution, in particular common envelope evolution (Ivanova *et al.* 2013).
- MBH binaries consisting of two BHs with masses $\gtrsim 10^5 M_\odot$ (Sesana 2013a); BHs at the upper end of the mass spectrum ($\gtrsim 10^8\text{--}10^9 M_\odot$) are sometimes referred to as supermassive black holes (SMBHs). MBHs are found in the centre of galaxies (Lynden-Bell 1969; Ferrarese & Ford 2005). When galaxies merge, their MBHs also spiral together (Volonteri *et al.* 2003; Schnittman 2013). The inspiral, merger and subsequent ring-down of the new MBH are all promising sources of GWs (Flanagan & Hedges 1998). Mergers are potentially the loudest GW signals. The combination of many inspirals should result in a stochastic background observable with PTAs (Sesana *et al.* 2008).
- Extreme-mass-ratio (EMR) systems of a stellar-mass CO orbiting an MBH. They evolve slowly as a consequence of their large mass-ratio (Glampedakis 2005; Barack 2009). EMR systems with highly eccentric orbits produce a burst of GWs as they

pass through periapse; these are EMRBs and are in frequency range of a LISA-like detector (Rubbo *et al.* 2006). Near circular orbits, as are expected to form in the last few years of inspiral prior to plunge, emit continuously within LISA's frequency band. These signals are extreme mass-ratio inspirals (EMRIs; Amaro-Seoane *et al.* 2007). EMRIs can be observed over many orbits, allowing exquisitely high signal-to-noise ratios (SNRs) to accumulate. This makes them excellent probes of the background geometry permitting precise measurements of the system parameters and tests of GR (Babak *et al.* 2011, e.g.,).

In addition to binaries, there are other potential sources of GWs. Supernovae are highly energetic, asymmetric explosions when a giant star ejects its outer envelope and as its core collapses to a NS or BH; these generate HF bursts of GWs (Dimmelmeier *et al.* 2002; Kotake *et al.* 2006). Rotating NSs are a source of continuous HF GWs if they posses some degree on axial asymmetry (Abbott *et al.* 2007; Prix 2009). More speculatively, early Universe processes, such as inflation (Grishchuk 2005) or a first-order phase transition (Binétruy *et al.* 2012), could have created GWs. Cosmic strings have also been hypothesised as a potential source (Damour & Vilenkin 2005; Binétruy *et al.* 2012). These relic GWs have been predicted across a range of frequencies and their discovery would be an exciting probe of the Universe before the emission of the CMB. Measuring the properties of GWs can tell us both about the source and the nature of gravity.

1.3 Astrophysical compact objects

To probe regions of strong gravity we need massive COs. These are provided in nature through the remnants of stellar evolution (Shapiro & Teukolsky 1983, section 1.1). Depending upon its mass, a star may end its life as a WD, NS or BH. More massive BHs can be found, having grown through other means.

1.3.1 White dwarfs and neutron stars

The least massive stars ($\sim 0.6\text{--}8M_{\odot}$) end their lives as WDs (Poelarends *et al.* 2008). These are made of electron-degenerate matter that form from the cores of former stars once their outer envelopes are lost (Althaus *et al.* 2010). WDs' faint luminosity comes from thermal emission. Eventually they cool, dimming and becoming black dwarfs (Shapiro & Teukolsky 1983, section 4.2); because of the long cooling times, no black dwarfs have yet formed.

WDs have maximum mass set by electron degeneracy pressure. This is known as the Chandrasekhar limit as is around $1.4M_{\odot}$ (Shapiro & Teukolsky 1983, section 3.4; Nomoto 1987; Timmes *et al.* 1996). Above this the WD will collapse under its weight until neutron degeneracy pressure takes over to balance the gravitational forces. We

then have a remnant NS or, if the mass is too large for neutron degeneracy to support, a BH (Woosley *et al.* 2002; Langer 2012).

NS form from stars of initial masses $\gtrsim 8-12M_{\odot}$ (Woosley *et al.* 2002; Poelarends *et al.* 2008; Langer 2012). They are made of nuclear density materials. The behaviour of matter under these extreme conditions is not well understood, leading to a plethora of different equations of state (Lattimer 2012). Probing the strong-field regions around NSs could not only provide a test of our understanding of gravitation, but also elucidate the properties of extremely dense matter (e.g., Read *et al.* 2009; Özel & Psaltis 2009; Lackey *et al.* 2012).

The maximum mass of a NS depends upon its equation of state (Shapiro & Teukolsky 1983, section 9.3). Hence there is no definitive theoretical prediction.⁵ The largest current estimate for a NS mass is $2.74 \pm 0.21M_{\odot}$ (Freire *et al.* 2008; Özel *et al.* 2012). Once the maximum NS mass is exceeded the gravitational force becomes overwhelming and the material is crushed down to become a BH (Shapiro & Teukolsky 1983, section 12.1). The initial stellar mass required for a star to end its life as a BH is uncertain, but is estimated to be $\gtrsim 25M_{\odot}$ (Woosley *et al.* 2002; Tauris *et al.* 2011).

1.3.2 Black holes

BHs are fascinating objects: beautifully simple but with many complexities in their interactions. The first BH was suggest by Michell (1784). This is not the same as the object that we understand today, but a Newtonian analogue: a star so massive that its escape velocity exceed the speed of light. The first general relativistic BH was the much celebrated Schwarzschild solution (Schwarzschild 1916). Discovered shortly after Einstein’s publication of his general theory, this was the first exact solution other than flat spacetime. It is the metric for the space surrounding a spherically symmetric distribution of matter. It also describes a non-rotating, uncharged BH. A BH is a region of spacetime where gravity is so intense that the exists an event horizon, beyond which nothing can escape (Misner *et al.* 1973, section 33.1). The nature of BHs not fully comprehended until many years after Schwarzschild published his metric; astrophysicists had to first realise the existence of WDs and NSs before they could accept the concept of completely collapsed objects (Israel 1987).

Following on from Schwarzschild’s discovery, came the solution of Reissner and Nordström for an electrically charged BH (Reissner 1916; Nordström 1918). There was then a long hiatus before Kerr’s discovery of the metric for a rotating BH (Kerr 1963). The set of BH solutions was completed by the discovey of the Kerr–Newman metric for charged, rotating BH (Newman *et al.* 1965). According to the no-hair theorem, any BH should

⁵The most famous upper mass is the Tolman–Oppenheimer–Volkoff limit (Tolman 1939; Oppenheimer & Volkoff 1939). This model is known to be inadequate as the calculated mass is too small.

be described completely by just its mass M_\bullet , spin and electric charge (Israel 1967, 1968; Carter 1971; Hawking 1972a; Robinson 1975). We expect the charge of an astrophysical BH to be negligible, hence we only need two parameters to describe the BHs of nature (Chandrasekhar 1992, sections 36 and 51).

Astrophysical BHs are grouped by their mass. We shall discuss three partitions: stellar-mass BHs, intermediate-mass BHs (IMBHs) and MBHs. MBHs are of major interest in this work and we pay them special attention.

The spin parameter a is related to the BH's angular momentum J by

$$J = M_\bullet ac; \quad (1.6)$$

it is often convenient to use the dimensionless spin

$$a_* = \frac{cJ}{GM_\bullet^2}. \quad (1.7)$$

The spin has a range of possible values $0 \leq |a_*| \leq 1$ (Chandrasekhar 1992, section 66). A spin $a_* = 0$ corresponds to non-rotating BH. In general a BH shall have some angular momentum, and we shall be mostly concerned with the Kerr solution.

1.3.2.1 Stellar-mass black holes

Stellar-mass BHs are an endpoint of stellar evolution, the product of the collapse of giant stars too massive to form NSs (Postnov & Yungelson 2006). These have masses of order of a solar mass: observations show a distribution of $\sim 5\text{--}10M_\odot$ (Özel *et al.* 2010; Farr *et al.* 2011).

1.3.2.2 Intermediate mass black holes

IMBHs bridge the gap between the other two classes. They are less well studied than the others, and lack concrete observational confirmation (Miller 2009), but have been proposed as a tentative explanation for some ultraluminous X-ray sources (Feng & Soria 2011). They potentially represent an intermediate stage in the evolution of MBHs (Graham & Scott 2013).

1.3.2.3 Massive black holes

MBHs have masses $\sim 10^5\text{--}10^{10}M_\odot$. Many, if not all, galactic nuclei have harboured an MBH during their evolution (Lynden-Bell & Rees 1971; Soltan 1982; Rees 1984). Observations have shown that there exist well-defined correlations between the MBHs' masses and the properties of their host galaxies, such as: bulge mass (Kormendy & Richstone 1995; Häring & Rix 2004; Graham 2012); luminosity (Magorrian *et al.* 1998; Marconi & Hunt 2003; Graham & Scott 2013); velocity dispersion (Ferrarese & Merritt 2000; Gebhardt *et al.* 2000; Tremaine *et al.* 2002; Graham *et al.* 2011); light concentration (Graham *et al.* 2001),

Sérsic index (Graham & Driver 2007; Savorgnan *et al.* 2013), and, for spiral galaxies, pitch angle (Seigar *et al.* 2008; Berrier *et al.* 2013). These suggest coeval evolution of the MBH and galaxy (Peng 2007; Jahnke & Macciò 2011), possibly with feedback mechanisms coupling the two (Haiman & Quataert 2004; Volonteri & Natarajan 2009). The MBH and the surrounding spheroidal component share a common history, such that the growth of one can inform us about the growth of the other.

The best opportunity to study MBHs comes from the compact object in our own galactic centre (GC), which is coincident with Sagittarius A* (Sgr A*). Through careful monitoring of stars orbiting the GC, this has been identified as an MBH of mass $M_\bullet \simeq 4 \times 10^6 M_\odot$ at a distance of only $R_0 \simeq 8$ kpc (Gillessen *et al.* 2009; Meyer *et al.* 2012).

The masses of other MBHs has been determined using a selection of techniques. Aside from being inferred from the correlations enumerated above, they can be measured directly using stellar or gas dynamical observations (Macchetto *et al.* 1997; van der Marel *et al.* 1998; Gebhardt *et al.* 2003, e.g.,) or maser measurements of the velocity of a circumnuclear disc (Miyoshi *et al.* 1995, e.g.,). After measuring the masses of MBHs we are left with the question of their spins.

The spin of an MBH is determined by several competing processes. An MBH accumulates mass and angular momentum through accretion (Volonteri 2010; King & Nixon 2013). Accretion from a gaseous disc shall spin up the MBH, potentially leading to high spin values (Volonteri *et al.* 2005), while a series of randomly orientated accretion events leads to a low spin value: we expect an average value $|a_*| \sim 0.1\text{--}0.3$ (King & Pringle 2006; King *et al.* 2008). The MBH also grows through mergers (Yu & Tremaine 2002; Malbon *et al.* 2007). Minor mergers with smaller BHs can decrease the spin (Hughes & Blandford 2003; Gammie *et al.* 2004), while a series of major mergers, between similar mass MBHs, would lead to a likely spin of $|a_*| \sim 0.7$ (González *et al.* 2007; Berti *et al.* 2007; Berti & Volonteri 2008). Measuring the spin of MBHs shall help us understand the relative importance of these processes, and perhaps shall give a glimpse into their host galaxies' pasts.

Elliptical and spiral galaxies are believed to host MBHs of differing spins because of their different evolutions: we expect MBHs in elliptical galaxies to have on average higher spins than MBHs in spiral galaxies, where random, small accretion episodes have played a more important role (Volonteri *et al.* 2007; Sikora *et al.* 2007).

It has been suggested that the spin of the Galaxy's MBH could be inferred from careful observation of the orbits of stars within a few milliparsecs of the GC (Merritt *et al.* 2010), although this is complicated because of perturbations due to other stars, or from observations of quasi-periodic oscillations in the luminosity of flares believed to originate from material orbiting close to the innermost stable orbits (Genzel *et al.* 2003; Bélanger *et al.* 2006; Trippe *et al.* 2007; Hamaus *et al.* 2009; Kato *et al.* 2010), though there are difficulties in interpreting these results (Psaltis 2008).

A further possibility is to use VLBI to resolve features of the size of the order

of the event horizon (Doeleman *et al.* 2008; Fish *et al.* 2011). The Galactic MBH, as a consequence of its mass and proximity, is the prime candidate, subtending about 50 μ as on the sky (Broderick *et al.* 2009b; Johannsen *et al.* 2012). With this capability, it would be possible to directly image accretion flows down to the horizon and also observe the MBH’s shadow. This is the dark region surrounding the BH from which no light can reach the observer; it is bounded by the innermost photon orbit (Chandrasekhar 1992, section 63). The position of the horizon and the exact shape of the shadow are determined by the metric. By measuring them it may be possible to measure the spin and inclination of the BH (Hioki & Maeda 2009), assuming it is Kerr, check whether it is an over-extreme Kerr BH (Bambi & Freese 2009), or even probe deviations from Kerr (Johannsen & Psaltis 2010a, b). The shape of the shadow of a Kerr BH is shown in figure 1.4. The shadow remains near circular for spin values $a \lesssim 0.9M_\bullet$ regardless of inclination even though the Kerr spacetime is highly non-spherically symmetric (Johannsen & Psaltis 2010b). Weak constraints already exist from VLBI observations (Broderick *et al.* 2009a, 2011); these determine that the spin is likely not high: $|a_*| = 0\text{--}0.64$ at 68% confidence and $|a_*| = 0\text{--}0.86$ at 95% confidence. Determining the spin to high precision is difficult.

The spins of MBHs in active galactic nuclei have been inferred using X-ray observations of Fe K emission lines (Miller 2007; McClintock *et al.* 2011). So far this has been done for a handful of other galaxies’ MBHs, as shown in table 1.1. Estimates for the spin cover a range of values up to the maximal value for an extremal Kerr black hole. Typical values are in the intermediate range of $a_* \sim 0.7$ and above with an uncertainty of about 10% on each measurement. There may be an observational bias toward high spin values (Brenneman *et al.* 2011).

1.4 Modified gravity

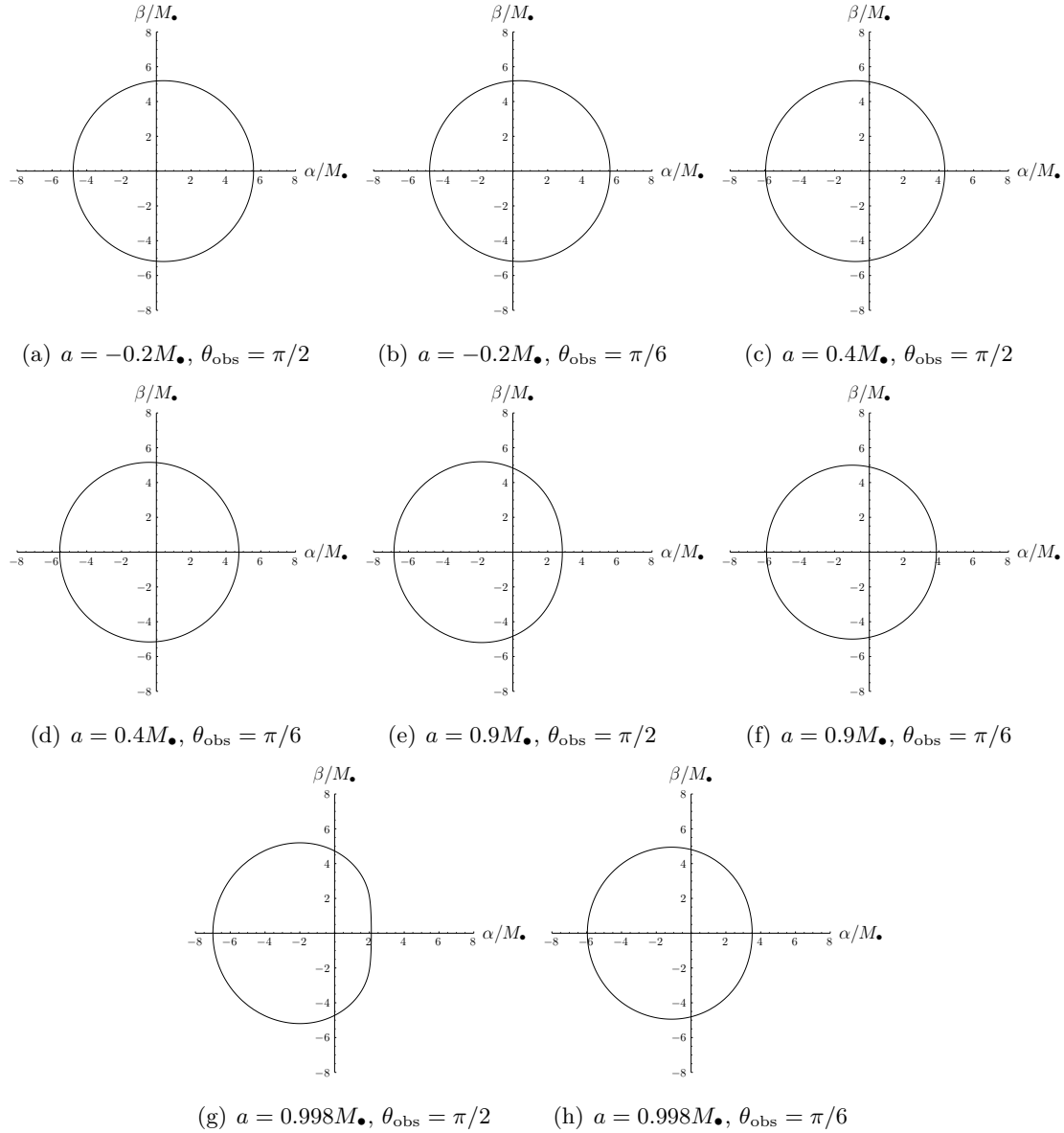


Figure 1.4 Apparent shape of the shadow of a Kerr BH viewed at infinity. α and β are the position coordinates projected onto the celestial sphere, and θ_{obs} is the polar coordinate of the observer (Chandrasekhar 1992, section 63). When $\theta_{\text{obs}} = 0, \pi$ we look along the spin axis and see a circular shadow because of axisymmetry.

AGN	a_*	Study
1H 0323+342	> 0.37	Walton <i>et al.</i> (2013)
1H 0419–577	> 0.89	Walton <i>et al.</i> (2013)
1H 0707–495	≥ 0.976	Zoghbi <i>et al.</i> (2010)
3C 120	$0.994^{+0.002}_{-0.003}$	Lohfink <i>et al.</i> (2013)
3C 382	< 0.81	Walton <i>et al.</i> (2013)
Ark 120	$0.74^{+0.19\dagger}_{-0.50}$	Nardini <i>et al.</i> (2011)
	$0.64^{+0.19}_{-0.11}$	Walton <i>et al.</i> (2013)
Ark 564	$0.96^{+0.01}_{-0.07}$	Walton <i>et al.</i> (2013)
Fairall 9	$0.60 \pm 0.07^*$	Schmoll <i>et al.</i> (2009)
	$0.44^{+0.04}_{-0.11}$	Patrick <i>et al.</i> (2011b)
	$0.39^{+0.48}_{-0.30}$	Emmanoulopoulos <i>et al.</i> (2011)
	$0.67^{+0.10}_{-0.11}$	Patrick <i>et al.</i> (2011a)
	$0.52^{+0.19}_{-0.15}$	Lohfink <i>et al.</i> (2012)
	$0.82^{+0.09}_{-0.19}$	Walton <i>et al.</i> (2013)
IRAS 00521–7054	$0.97^{+0.03}_{-0.13}$	Tan <i>et al.</i> (2012)
IRAS 13224–3809	$0.988 \pm 0.001^*$	Fabian <i>et al.</i> (2013)
MCG–6–30–15	$0.989^{+0.009}_{-0.002}$	Brenneman & Reynolds (2006)
	$0.86^{+0.01}_{-0.02}$	de la Calle Pérez <i>et al.</i> (2010)
	$0.49^{+0.20}_{-0.12}$	Patrick <i>et al.</i> (2011a)
Mrk 79	0.7 ± 0.1	Gallo <i>et al.</i> (2011)
Mrk 110	$0.96^{+0.03}_{-0.07}$	Walton <i>et al.</i> (2013)
Mrk 335	$0.70^{+0.12}_{-0.01}$	Patrick <i>et al.</i> (2011b)
	$0.83^{+0.09}_{-0.13}$	Walton <i>et al.</i> (2013)
Mrk 359	$0.66^{+0.30}_{-0.54}$	Walton <i>et al.</i> (2013)
Mrk 509	$0.78^{+0.03}_{-0.04}$	de la Calle Pérez <i>et al.</i> (2010)
	$0.36^{+0.20}_{-0.37}$	Walton <i>et al.</i> (2013)
Mrk 841	> 0.52	Walton <i>et al.</i> (2013)
Mrk 1018	$0.58^{+0.36}_{-0.54}$	Walton <i>et al.</i> (2013)
NGC 1365	≥ 0.84	Risaliti <i>et al.</i> (2013)
NGC 3783	$\geq 0.88^\dagger$	Brenneman <i>et al.</i> (2011)
	< 0.32	Patrick <i>et al.</i> (2011a)
NGC 4051	< 0.94	Patrick <i>et al.</i> (2011a)
NGC 7469	$0.69^{+0.09}_{-0.09}$	Patrick <i>et al.</i> (2011b)
	$0.64^{+0.13}_{-0.20}$	Walton <i>et al.</i> (2013)
PDS 456	> 0.96	Walton <i>et al.</i> (2013)
PKS 0558–504	> 0.95	Walton <i>et al.</i> (2013)
RBS 1124	> 0.97	Walton <i>et al.</i> (2013)
SWIFT J0501.9–3239	> 0.99	Walton <i>et al.</i> (2013)
SWIFT J2127.4+5654	0.6 ± 0.2	Miniutti <i>et al.</i> (2009)
	$0.70^{+0.10}_{-0.14}$	Patrick <i>et al.</i> (2011b)
Ton S180	$0.92^{+0.03}_{-0.11}$	Walton <i>et al.</i> (2013)
UGC 6728	> 0.71	Walton <i>et al.</i> (2013)

Table 1.1 Measurements of MBH spin from iron emission lines. Confidence levels are 90% except where indicated otherwise: an asterisk (*) is used for 68% and an obelisk (†) is used for 99%. The scatter in results indicates the complexities of modelling the accretion disc.

Part II

Astronomical systems

Chapter 2

Extreme-mass-ratio burst waveforms

2.1 Massive black holes and extreme-mass-ratio events

An exciting means of inferring information about MBHs is through GWs emitted when COs, such as stellar-mass BHs, NSs, WDs or low mass main sequence (MS) stars, pass close by (Sathyaprakash & Schutz 2009). A space-borne detector, such as LISA, is designed to be able to detect GWs in the frequency range of interest for these encounters (Danzmann & Rüdiger 2003; Jennrich *et al.* 2011; Amaro-Seoane *et al.* 2012). The identification of waves requires a set of accurate waveform templates covering parameter space. Much work has already been done on the waveforms generated when companion objects inspiral towards an MBH (Glampedakis 2005; Barack 2009); as they orbit, the GWs carry away energy and angular momentum, causing the orbit to shrink until eventually the object plunges into the MBH. These systems are typically formed following two-body encounters so that the initial orbits are highly eccentric; a burst of radiation is emitted during each periapse passage. These are extreme mass-ratio bursts (EMRBs; Rubbo *et al.* 2006). Assuming that the companion is not scattered from its orbit, and does not plunge straight into the MBH, its orbit evolves, becoming more circular, and it shall begin to continuously emit significant gravitational radiation in the frequency range of a LISA-like space-borne detector. The resulting signals are extreme mass-ratio inspirals (EMRIs; Amaro-Seoane *et al.* 2007).

Studies of these systems have usually focused upon the phase when the orbit is close to plunge and completes a large number of cycles in the detector's frequency band, allowing a high signal-to-noise ratio (SNR) to be accumulated. Here, we investigate high eccentricity orbits. These are the initial bursting orbits from which an EMRI may evolve, and are the consequence of scattering from two-body encounters. The event rate for the detection of such EMRBs with LISA has been estimated to be as high as 15 yr^{-1} (Rubbo *et al.* 2006), although this has been subsequently revised downwards to the order of 1 yr^{-1} (Hopman *et al.* 2007). The event rate is dominated by bursts from the Galactic Centre (GC). Even if only a single burst is detected during a mission, this

is still an exciting possibility since the information carried by the GW should give an unparalleled probe of the structure of spacetime of the GC.

To model bursts we make the simplifying assumption that all these orbits are marginally bound, or parabolic, since highly eccentric orbits appear almost indistinguishable from an appropriate parabolic orbit. Here “parabolic” and “eccentricity” refer to the energy of the geodesic and not to the geometric shape of the orbit.¹ Following such a trajectory an object may make just one pass of the MBH or, if the periapsis distance is small enough, it may complete a number of rotations. Such an orbit is referred to as zoom–whirl (Glampedakis & Kennefick 2002).

We begin our investigation of the properties of EMRBs as a means of studying MBHs by constructing approximate waveforms. To do so we integrate the geodesic equations for a parabolic orbit in Kerr spacetime (section 2.2); we assume that the orbiting body is a test particle, such that it does not influence the underlying spacetime, and that the orbital parameters evolve negligibly during the orbit such that they may be held constant. We use this trajectory to construct an approximate numerical kludge (NK) waveform (Babak *et al.* 2007) as explained in section 2.3. In section 2.4 we establish what the LISA detectors would measure and how the signal would be analysed. Since there does not exist a definite mission design, we use the classic LISA design for the majority of this work. It is hoped that any future missions shall have comparable sensitivity, and studies using the LISA design are sensible benchmarks for comparison. In a few places we look at the detectability of bursts using eLISA. We confirm the accuracy of the kludge waveforms in section 2.5 by comparing the energy flux to fluxes calculated using other approaches. The typical error introduced by the NK approximation may be a few percent, but this worsens as the periapsis approaches the last non-plunging orbit.

Having established the accuracy of our NK waveforms, we study what information can be extracted from them. Exactly what can be inferred depends upon the orbit. We begin in chapter 3 by looking at EMRBs from the GC as the Galaxy’s MBH is the most promising to study. Finding promising results, we extend our study to extragalactic sources in chapter 4. ...

2.2 Parabolic orbits in Kerr spacetime

2.2.1 The metric and geodesic equations

Astrophysical BHs are described by the Kerr metric (Kerr 1963). In standard Boyer–Lindquist coordinates the line element is (Boyer & Lindquist 1967; Hobson *et al.* 2006, section 13.7)

$$ds^2 = \frac{\varrho^2 \Delta}{\Sigma^2} c^2 dt^2 - \frac{\Sigma \sin^2 \theta}{\varrho^2} (d\phi - \omega dt)^2 - \frac{\varrho^2}{\Delta} dr^2 - \varrho^2 d\theta^2, \quad (2.1)$$

¹Marginally bound Keplerian orbits (in flat spacetime) are parabolic in both senses.

where we have introduced functions

$$\varrho^2 = r^2 + a^2 \cos^2 \theta, \quad (2.2a)$$

$$\Delta = r^2 - \frac{2GM_\bullet r}{c^2} + a^2, \quad (2.2b)$$

$$\Sigma = (r^2 + a^2)^2 - a^2 \Delta \sin^2 \theta, \quad (2.2c)$$

$$\omega = \frac{2GM_\bullet ar}{c\Sigma}. \quad (2.2d)$$

For the remainder of this section we use natural units with $G = c = 1$.

Geodesics are parametrized by three conserved quantities (aside from the particle's mass μ): energy (per unit mass) E , specific angular momentum about the symmetry axis (the z -axis) L_z , and Carter constant Q (Carter 1968; Chandrasekhar 1992, section 62). The geodesic equations are

$$\varrho^2 \frac{dt}{d\tau} = a(L_z - aE \sin^2 \theta) + \frac{r^2 + a^2}{\Delta} T, \quad (2.3a)$$

$$\varrho^2 \frac{dr}{d\tau} = \pm \sqrt{V_r}, \quad (2.3b)$$

$$\varrho^2 \frac{d\theta}{d\tau} = \pm \sqrt{V_\theta}, \quad (2.3c)$$

$$\varrho^2 \frac{d\phi}{d\tau} = \frac{L_z}{\sin^2 \theta} - aE + \frac{a}{\Delta} T, \quad (2.3d)$$

where we have introduced potentials

$$T = E(r^2 + a^2) - aL_z, \quad (2.4a)$$

$$V_r = T^2 - \Delta \left[r^2 + (L_z - aE)^2 + Q \right], \quad (2.4b)$$

$$V_\theta = Q - \cos^2 \theta \left[a^2 (1 - E^2) + \frac{L_z^2}{\sin^2 \theta} \right], \quad (2.4c)$$

and τ is proper time. The signs of the r and θ equations may be chosen independently.

For a parabolic orbit $E = 1$; the particle is at rest at infinity. This simplifies the geodesic equations. It also allows us to give a simple interpretation for the Carter constant: this is defined as

$$Q = L_\theta^2 + \cos^2 \theta \left[a^2 (1 - E^2) + \frac{L_z^2}{\sin^2 \theta} \right], \quad (2.5)$$

where L_θ is the (non-conserved) specific angular momentum in the θ -direction ($V_\theta = L_\theta^2$).

For $E = 1$ we have

$$Q = L_\theta^2 + \cot^2 \theta L_z^2 = L_\infty^2 - L_z^2; \quad (2.6)$$

here L_∞ is the total specific angular momentum at infinity, where the metric is asymptotically flat (de Felice 1980).² This is as in Schwarzschild spacetime.

²Rosquist *et al.* (2009) discuss the interpretation of Q in the limit $G \rightarrow 0$, corresponding to a flat spacetime.

2.2.2 Integration variables and turning points

In integrating the geodesic equations, difficulties can arise because of the presence of turning points, when the sign of the r or θ geodesic equation changes. The radial turning points are at the periapsis r_p and at infinity. We locate the periapsis by finding the roots of

$$V_r = 2M_\bullet r^3 - (L_z^2 + Q) r^2 + 2M_\bullet [(L_z - a)^2 + Q] r - a^2 Q = 0. \quad (2.7)$$

This has three roots, which we shall denote $\{r_1, r_2, r_p\}$; the periapsis r_p is the largest real root.³

We avoid the difficulties associated with the turning point by introducing angular variables that always increase with proper time (Drasco & Hughes 2004): inspired by Keplerian orbits, we parametrize our trajectory by

$$r = \frac{p}{1 + e \cos \psi}, \quad (2.8)$$

where $e = 1$ is the eccentricity $p = 2r_p$ is the semilatus rectum and ψ is the relativistic anomaly (Darwin 1961). As ψ covers its range from $-\pi$ to π , r traces out a complete orbit. The geodesic equation for ψ is

$$\varrho^2 \frac{d\psi}{d\tau} = \left\{ M_\bullet \left[2r_p - (r_1 + r_2)(1 + \cos \psi) + \frac{r_1 r_2}{2r_p} (1 + \cos \psi)^2 \right] \right\}^{1/2}. \quad (2.9)$$

Parametrizing an orbit by its periapsis and eccentricity has the additional benefit of allowing easier comparison with its flat-space equivalent (Gair *et al.* 2005).

The θ motion is usually bounded, with $\theta_0 \leq \theta \leq \pi - \theta_0$; in the event that $L_z = 0$ the particle follows a polar orbit and θ covers its full range (Wilkins 1972). The turning points are given by

$$V_\theta = Q - \cot^2 \theta L_z^2 = 0. \quad (2.10)$$

Changing variable to $\xi = \cos^2 \theta$, we have a maximum value $\xi_0 = \cos^2 \theta_0$ given by

$$\xi_0 = \frac{Q}{Q + L_z^2} = \frac{Q}{L_\infty^2}. \quad (2.11)$$

See figure 2.1 for a geometrical visualization. Introducing a second angular variable (Hughes 2000; Drasco & Hughes 2004)

$$\xi = \xi_0 \cos^2 \chi. \quad (2.12)$$

Over one 2π period of χ , θ oscillates from its minimum value to its maximum and back. The geodesic equation for χ is

$$\varrho^2 \frac{d\chi}{d\tau} = \sqrt{Q + L_z^2}. \quad (2.13)$$

³The apoapsis is not a (fourth) root to this equation as we have removed it by taking $E = 1$ before solving. This turning point can be found by setting the unconstrained expression for V_r equal to zero, and then solving for $E(r)$; taking the limit $r \rightarrow \infty$ gives $E \rightarrow 1$ (Wilkins 1972).

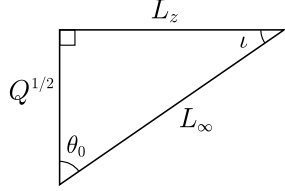


Figure 2.1 The angular momenta L_∞ , L_z and \sqrt{Q} define a right-angled triangle. The acute angles are θ_0 , the extremal value of the polar angle, and ι , the orbital inclination (Ryan 1996; Glampedakis *et al.* 2002).

2.3 Waveform construction

We can now calculate the geodesic trajectory. The orbiting body is assumed to follow this track exactly; we ignore evolution due to the radiation of energy and angular momentum, which should be negligible for EMRBs. From this trajectory we calculate the waveform using a semirelativistic approximation (Ruffini & Sasaki 1981): we assume the particle moves along the Kerr geodesic, but radiates as if it were in flat spacetime. This quick-and-dirty technique is known as a numerical kludge (NK), and has been shown to approximate well results computed by more accurate methods (Babak *et al.* 2007). It is often compared to a bead travelling along a wire. The shape of the wire is set by the Kerr geodesic, but the bead moves along in flat space.

2.3.1 The kludge approximation

Numerical kludge approximations aim to encapsulate the main characteristics of a waveform by using the exact particle trajectory (ignoring inaccuracies from radiative effects and from the particle's self-force), whilst saving on computational time by using approximate waveform generation techniques.

We build an equivalent flat-space trajectory by identifying the Boyer–Lindquist coordinates with a set of flat-space coordinates. We consider two choices:

1. Identify the Boyer–Lindquist coordinates with flat-space spherical polars $\{r_{\text{BL}}, \theta_{\text{BL}}, \phi_{\text{BL}}\} \rightarrow \{r_{\text{sph}}, \theta_{\text{sph}}, \phi_{\text{sph}}\}$, then define flat-space Cartesian coordinates (Gair *et al.* 2005; Babak *et al.* 2007)

$$\mathbf{x} = \begin{pmatrix} r_{\text{sph}} \sin \theta_{\text{sph}} \cos \phi_{\text{sph}} \\ r_{\text{sph}} \sin \theta_{\text{sph}} \sin \phi_{\text{sph}} \\ r_{\text{sph}} \cos \theta_{\text{sph}} \end{pmatrix}. \quad (2.14)$$

2. Identify the Boyer–Lindquist coordinates with flat-space oblate-spheroidal coordinates

$\{r_{\text{BL}}, \theta_{\text{BL}}, \phi_{\text{BL}}\} \rightarrow \{r_{\text{ob}}, \theta_{\text{ob}}, \phi_{\text{ob}}\}$ so that the flat-space Cartesian coordinates are

$$\mathbf{x} = \begin{pmatrix} \sqrt{r_{\text{ob}}^2 + a^2} \sin \theta_{\text{ob}} \cos \phi_{\text{ob}} \\ \sqrt{r_{\text{ob}}^2 + a^2} \sin \theta_{\text{ob}} \sin \phi_{\text{ob}} \\ r_{\text{ob}} \cos \theta_{\text{ob}} \end{pmatrix}. \quad (2.15)$$

These are appealing because in the limit that $G \rightarrow 0$, where the gravitating mass goes to zero, the Kerr metric in Boyer–Lindquist coordinates reduces to the Minkowski metric in oblate-spheroidal coordinates.

The two coincide for $a \rightarrow 0$ or $r \rightarrow \infty$.

There is no well motivated argument that either coordinate system must yield an accurate GW; their use is justified *post facto* by comparison with results obtained from more accurate, and computationally intensive, methods (Gair *et al.* 2005; Babak *et al.* 2007). The ambiguity in assigning flat-space coordinates reflects the inconsistency of the semirelativistic approximation: the geodesic trajectory was calculated for the Kerr geometry; by moving to flat spacetime we lose the reason for its existence. This should not be regarded as a major problem; it is an artifact of the basic assumption that the shape of the trajectory is important for determining the character of the radiation, but the curvature of the spacetime in the vicinity of the source is not. By binding the particle to the exact geodesic, we ensure that the waveform has spectral components at the correct frequencies, but by assuming flat spacetime for generation of GWs they shall not have the correct amplitudes.

2.3.2 The quadrupole–octupole formula

Now we have a flat-space particle trajectory $x_{\text{P}}^{\mu}(\tau)$, we may apply a flat-space wave generation formula. We use the quadrupole–octupole formula to calculate the gravitational strain (Bekenstein 1973; Press 1977; Yunes *et al.* 2008)

$$h^{jk}(t, \mathbf{x}) = -\frac{2G}{c^6 r} \left(\ddot{I}^{jk} - 2n_i \ddot{S}^{ijk} + n_i \ddot{M}^{ijk} \right)_{t' = t-r/c}, \quad (2.16)$$

where an over-dot represents differentiation with respect to time t , t' is the retarded time, $r = |\mathbf{x} - \mathbf{x}_{\text{P}}|$ is the radial distance, \mathbf{n} is the radial unit vector, and the mass quadrupole I^{jk} , current quadrupole S^{ijk} and mass octupole M^{ijk} are defined by

$$I^{jk}(t') = \int x'^j x'^k T^{00}(t', \mathbf{x}') d^3 x'; \quad (2.17a)$$

$$S^{ijk}(t') = \int x'^j x'^k T^{0i}(t', \mathbf{x}') d^3 x'; \quad (2.17b)$$

$$M^{ijk}(t') = \frac{1}{c} \int x'^i x'^j x'^k T^{00}(t', \mathbf{x}') d^3 x', \quad (2.17c)$$

for energy-momentum tensor $T^{\mu\nu}$. This is correct for a slowly moving source. It is the familiar quadrupole formula (Misner *et al.* 1973, section 36.10; Hobson *et al.* 2006,

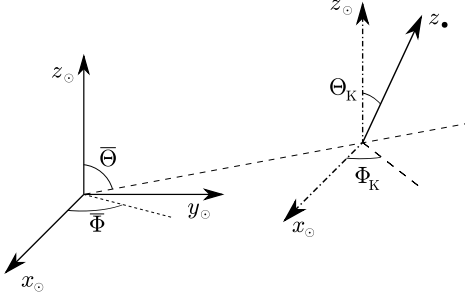


Figure 2.2 The relationship between the MBH’s coordinate system x_\bullet^i and the SS coordinate system x_\odot^i . The MBH’s spin axis is aligned with the z_\bullet -axis. The orientation of the MBH’s x - and y -axes is arbitrary. We choose x_\bullet to be orthogonal to the direction to the SS.

section 17.9), derived from linearized theory, plus the next order terms. For a point mass, $T^{\mu\nu}$ contains a δ -function which allows easy evaluation of the integrals.

Since we are only interested in GWs, we use the transverse-traceless (TT) gauge (Misner *et al.* 1973, box 35.1).

2.4 Signal detection and analysis

2.4.1 The LISA detector

The classic LISA design is a three arm, space-borne laser interferometer (Bender *et al.* 1998; Danzmann & Rüdiger 2003). The arms form an equilateral triangle that rotates as the system’s centre of mass follows a circular, heliocentric orbit, trailing 20° behind the Earth. eLISA has a similar design, but has only two arms, which are shorter in length, and trails 9° behind the Earth (Jennrich *et al.* 2011).

To describe the detector configuration, and to transform from the MBH coordinate system to those of the detector, we use three coordinate systems: those of the BH at the GC x_\bullet^i ; ecliptic coordinates centred at the solar system (SS) barycentre x_\odot^i , and coordinates that co-rotate with the detector x_d^i . The MBH’s coordinate system and the SS coordinate system are depicted in figure 2.2. The mission geometry for LISA and eLISA is shown in figure 2.3. We define the detector coordinates such that the detector-arms lie in the x_d - y_d plane as in Cutler (1998). We have computed the waveforms in the MBH’s coordinates, but it is simplest to describe the measured signal using the detector’s coordinates.

The strains measured in the three arms can be combined such that LISA behaves as a pair of 90° interferometers at 45° to each other, with signals scaled by $\sqrt{3}/2$ (Cutler 1998). We denote the two detectors as I and II and use vector notation $\mathbf{h}(t) = (h_I(t), h_{II}(t)) = \{h_A(t)\}$ to represent signals from both detectors. As eLISA only has two arms it functions as a single detector, in this case $\{h_A(t)\} = h_I(t)$.

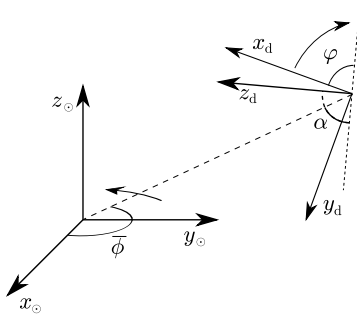


Figure 2.3 The relationship between the detector coordinates x_d^i and the ecliptic coordinates of the SS x_\odot^i (Bender *et al.* 1998; Jennrich *et al.* 2011). The detector inclination is $\alpha = 60^\circ$.

2.4.2 Frequency domain formalism

Having constructed the GW $\mathbf{h}(t)$ that shall be incident upon the detector, we may consider how to analyse the waveform and extract the information it contains. We briefly recap GW signal analysis, with application to LISA. A more complete discussion can be found in Finn (1992) and Cutler & Flanagan (1994). Adaption for eLISA requires a substitution of the noise distribution, and the removal of the sum over data channels, since it would only have one.

The measured strain $\mathbf{s}(t)$ is the combination of the signal and the detector noise

$$\mathbf{s}(t) = \mathbf{h}(t) + \mathbf{n}(t); \quad (2.18)$$

we assume the noise $n_A(t)$ is stationary and Gaussian, and that noise in the two detectors is uncorrelated, but shares the same characterisation (Cutler 1998).

The properties of the noise allow us to define a natural inner product and associated distance on the space of signals (Cutler & Flanagan 1994)

$$(\mathbf{g}|\mathbf{k}) = 2 \int_0^\infty \frac{\tilde{g}_A^*(f)\tilde{k}_A(f) + \tilde{g}_A(f)\tilde{k}_A^*(f)}{S_n(f)} df, \quad (2.19)$$

introducing Fourier transforms

$$\tilde{g}(f) = \mathcal{F}\{g(t)\} = \int_{-\infty}^{\infty} g(t) \exp(2\pi ift) dt, \quad (2.20)$$

and $S_n(f)$ is the noise spectral density. The inner product is derived in appendix A. The signal-to-noise ratio is approximately

$$\rho[\mathbf{h}] = (\mathbf{h}|\mathbf{h})^{1/2}. \quad (2.21)$$

The probability of a particular realization of noise $\mathbf{n}(t) = \mathbf{n}_0(t)$ is

$$p(\mathbf{n}(t) = \mathbf{n}_0(t)) \propto \exp\left[-\frac{1}{2}(\mathbf{n}_0|\mathbf{n}_0)\right]. \quad (2.22)$$

Thus, if the incident waveform is $\mathbf{h}(t)$, the probability of measuring signal $\mathbf{s}(t)$ is

$$p(\mathbf{s}(t)|\mathbf{h}(t)) \propto \exp\left[-\frac{1}{2}(\mathbf{s} - \mathbf{h}|\mathbf{s} - \mathbf{h})\right]. \quad (2.23)$$

2.4.3 The noise curve

LISA's noise has two sources: instrumental noise and confusion noise, primarily from WD binaries. The latter may be divided into contributions from galactic and extragalactic binaries. In this work we use the noise model of Barack & Cutler (2004). The shape of the noise curve can be seen in figure 2.4. The instrumental noise dominates at both high and low frequencies. The confusion noise is important at intermediate frequencies, and is responsible for the cusp around 10^{-3} Hz. eLISA shares the same sources of noise, but is less affected by confusion (Jennrich *et al.* 2011). Its sensitivity regime is shifted to higher frequencies because of the shorter arm length.

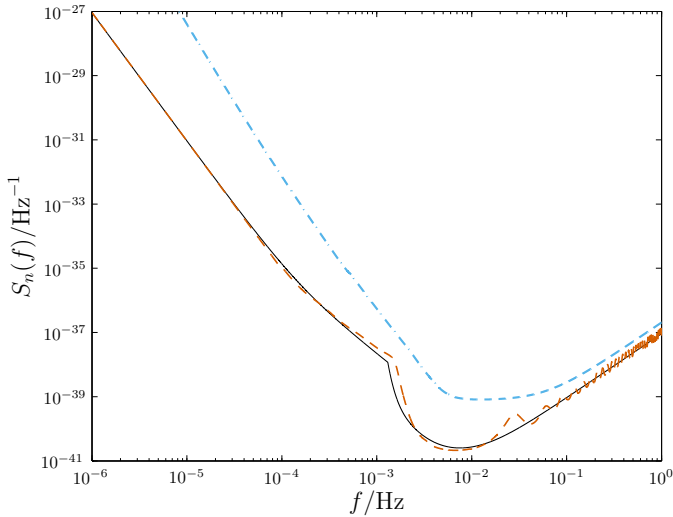


Figure 2.4 The detector noise curves. The solid line indicates the analytic approximation of Barack & Cutler (2004) used in this work. For comparison, the dashed line is from the online LISA sensitivity curve generator (<http://www.srl.caltech.edu/~shane/sensitivity/>; Larson, Hiscock & Hellings 2000; Larson, Hellings & Hiscock 2002). For bursts from the Galactic Centre we are most interested in the low-frequency region where the two curves are the same. The dot-dashed line shows the eLISA noise curve.

2.4.4 Window functions

There is one remaining complication regarding signal analysis: as we are Fourier transforming a finite signal we encounter spectral leakage; a contribution from large amplitude spectral components leaks into surrounding components (sidelobes), obscuring and distorting the spectrum at these frequencies (Harris 1978). This is an inherent problem with finite signals; it shall be as much of a problem when analysing signals from an actual mission as it is here. To mitigate, but unfortunately not eliminate, these effects, the time-domain signal can be multiplied by a window function. These are discussed in detail in appendix B. We adopt the Nuttall four-term window with continuous first derivative (Nuttall 1981) for our results. This should not affect the accuracy of our

conclusions.

2.5 Energy spectra

To check the NK waveforms, we compare the energy spectra calculated from these with those obtained from the classic treatment of Peters & Mathews (1963) and Peters (1964). This calculates GW emission for Keplerian orbits in flat spacetime, assuming only quadrupole radiation. The spectrum produced should be similar to that obtained from the NK in weak fields, that is for large periapses; we do not expect an exact match because of the differing input physics and varying approximations.

In addition to using the energy spectrum, we also use the total energy flux. This contains less information than the spectrum; however, Martel (2004) has calculated results for parabolic orbits in Schwarzschild spacetime using time-domain BH perturbation theory. These should be more accurate than results calculated using the Peters and Mathews formalism.

As we are considering Schwarzschild spacetime, the two NK coordinate choices coincide and there is no need to differentiate between them. In general, we do not intend to use the kludge waveforms to calculate an accurate energy flux: this would be inconsistent as we assume the orbits do not evolve with time. We only calculate the energy flux as a sanity check, to confirm that the kludge approximation is consistent with other approaches.

2.5.1 Kludge spectrum

A GW in the TT gauge has an effective energy-momentum tensor (Misner *et al.* 1973, section 35.15)

$$T_{\mu\nu} = \frac{c^4}{32\pi G} \left\langle \partial_\mu h_{ij} \partial_\nu h^{ij} \right\rangle, \quad (2.24)$$

where $\langle \dots \rangle$ indicates averaging over several wavelengths or periods. The energy flux through a sphere of radius R is

$$\frac{dE}{dt} = \frac{c^3}{32\pi G} R^2 \int d\Omega \left\langle \frac{dh_{ij}}{dt} \frac{dh^{ij}}{dt} \right\rangle, \quad (2.25)$$

with $\int d\Omega$ representing integration over all solid angles. From equation (2.16) the waves have a $1/r$ dependence; if we define

$$h_{ij} = \frac{H_{ij}}{r}, \quad (2.26)$$

we see the flux is independent of R , as required for energy conservation, and

$$\frac{dE}{dt} = \frac{c^3}{32\pi G} \int d\Omega \left\langle \frac{dH_{ij}}{dt} \frac{dH^{ij}}{dt} \right\rangle. \quad (2.27)$$

Integrating to find the total energy emitted

$$E = \frac{c^3}{32\pi G} \int d\Omega \int_{-\infty}^{\infty} dt \frac{dH_{ij}}{dt} \frac{dH^{ij}}{dt}. \quad (2.28)$$

Since we are considering all time, the localization of the energy is no longer of importance and it is unnecessary to average over several periods. Switching to Fourier representation $\tilde{H}_{ij}(f) = \mathcal{F}\{H_{ij}(t)\}$,

$$E = \frac{\pi c^3}{4G} \int d\Omega \int_0^{\infty} df f^2 \tilde{H}^{ij}(f) \tilde{H}_{ij}^*(f), \quad (2.29)$$

using $\tilde{H}_{ij}^*(f) = \tilde{H}_{ij}(-f)$ as the signal is real. From this we identify the energy spectrum as

$$\frac{dE}{df} = \frac{\pi c^3}{4G} \int d\Omega f^2 \tilde{H}^{ij}(f) \tilde{H}_{ij}^*(f). \quad (2.30)$$

2.5.2 Peters and Mathews spectrum

For an orbit of eccentricity e with periapse radius r_p , Peters & Mathews (1963) give the power radiated into the n -th harmonic of the orbital angular frequency as

$$P(n) = \frac{32}{5} \frac{G^4}{c^5} \frac{M_\bullet^2 \mu^2 (M_\bullet + \mu) (1 - e)^5}{r_p^5} g(n, e), \quad (2.31)$$

where the function $g(n, e)$ is defined in terms of Bessel functions of the first kind

$$g(n, e) = \frac{n^4}{32} \left\{ \left[J_{n-2}(ne) - 2eJ_{n-1}(ne) + \frac{2}{n} J_n(ne) + 2eJ_{n+1}(ne) - J_{n+2}(ne) \right]^2 + (1 - e^2) [J_{n-2}(ne) - 2J_n(ne) + J_{n+2}(ne)]^2 + \frac{4}{3n^2} [J_n(ne)]^2 \right\}. \quad (2.32)$$

The Keplerian orbital frequency is

$$\omega_1^2 = \frac{G(M_\bullet + \mu)(1 - e)^3}{r_p^3} = (1 - e)^3 \omega_c^2, \quad (2.33)$$

where ω_c is defined as the angular frequency of a circular orbit of radius r_p . The energy radiated per orbit into the n -th harmonic, that is at frequency $\omega_n = n\omega_1$, is

$$E(n) = \frac{2\pi}{\omega_1} P(n); \quad (2.34)$$

as $e \rightarrow 1$ for a parabolic orbit, $\omega_1 \rightarrow 0$ as the orbital period becomes infinite. The energy radiated per orbit is then the total energy radiated. The spacing of harmonics is $\Delta\omega = \omega_1$, giving energy spectrum

$$\frac{dE}{d\omega} \Big|_{\omega_n} \omega_1 = E(n). \quad (2.35)$$

Changing to linear frequency $2\pi f = \omega$,

$$\frac{dE}{df} \Big|_{f_n} = \frac{128\pi^2}{5} \frac{G^3}{c^5} \frac{M_\bullet^2 \mu^2}{r_p^2} (1 - e)^2 g(n, e) \quad (2.36)$$

$$= \frac{4\pi^2}{5} \frac{G^3}{c^5} \frac{M_\bullet^2 \mu^2}{r_p^2} \ell(n, e), \quad (2.37)$$

where the function $\ell(n, e)$ is defined in the last line. For a parabolic orbit, we must take the limit of $\ell(n, e)$ as $e \rightarrow 1$.

We simplify $\ell(n, e)$ using the recurrence formulae (Watson 1995, section 2.12)

$$J_{\nu-1}(z) + J_{\nu+1}(z) = \frac{2\nu}{z} J_\nu(z) \quad (2.38)$$

$$J_{\nu-1}(z) - J_{\nu+1}(z) = 2J'_\nu(z), \quad (2.39)$$

and eliminate n using

$$n = \frac{\omega_n}{\omega_1} = (1 - e)^{-3/2} \tilde{f}, \quad (2.40)$$

where $\tilde{f} = \omega_n/\omega_c = f_n/f_c$ is a dimensionless frequency. To find the limit we define two new functions (Berry & Gair 2010)

$$A(\tilde{f}) = \lim_{e \rightarrow 1} \left\{ \frac{J_n(ne)}{(1 - e)^{1/2}} \right\}; \quad B(\tilde{f}) = \lim_{e \rightarrow 1} \left\{ \frac{J'_n(ne)}{1 - e} \right\}. \quad (2.41)$$

To give a well-defined energy spectrum, both of these must be finite.

The Bessel function has an integral representation

$$J_\nu(z) = \frac{1}{\pi} \int_0^\pi \cos(\nu\vartheta - z \sin \vartheta) d\vartheta; \quad (2.42)$$

we want the limit of this for $\nu \rightarrow \infty$, $z \rightarrow \infty$, with $z \leq \nu$. Using the stationary phase approximation, the dominant contribution to the integral comes from the regime in which the argument of the cosine is approximately zero (Watson 1995, sections 8.2, 8.43):

$$J_\nu(z) \sim \frac{1}{\pi} \int_0^\pi \cos\left(\nu\vartheta - z\vartheta + \frac{z}{6}\vartheta^3\right) d\vartheta \quad (2.43)$$

$$\sim \frac{1}{\pi} \int_0^\infty \cos\left(\nu\vartheta - z\vartheta + \frac{z}{6}\vartheta^3\right) d\vartheta; \quad (2.44)$$

this last expression is an Airy integral and has a standard form (Watson 1995, section 6.4)

$$\int_0^\infty \cos(t^3 + xt) dt = \frac{\sqrt{x}}{3} K_{1/3} \left(\frac{2x^{3/2}}{3^{3/2}} \right), \quad (2.45)$$

where $K_\nu(z)$ is a modified Bessel function of the second kind. Using this to evaluate the limit gives

$$J_\nu(z) \sim \frac{1}{\pi} \sqrt{\frac{2(\nu - z)}{3z}} K_{1/3} \left(\frac{2^{3/2}}{3} \sqrt{\frac{(\nu - z)^3}{z}} \right). \quad (2.46)$$

For our case,

$$J_n(ne) \sim \frac{1}{\pi} \sqrt{\frac{2}{3}} (1 - e)^{1/2} K_{1/3} \left(\frac{2^{3/2} \tilde{f}}{3} \right), \quad (2.47)$$

and the first limiting function is well defined,

$$A(\tilde{f}) = \frac{1}{\pi} \sqrt{\frac{2}{3}} K_{1/3} \left(\frac{2^{3/2} \tilde{f}}{3} \right). \quad (2.48)$$

To find the derivative we combine equations (2.39) and (2.46), and expand to lowest order yielding

$$J'_n(ne) \sim -\frac{1}{2\pi}\sqrt{\frac{2}{3}}(1-e)\left[2^{3/2}K'_{1/3}\left(\frac{2^{3/2}\tilde{f}}{3}\right) + \frac{1}{\tilde{f}}K_{1/3}\left(\frac{2^{3/2}\tilde{f}}{3}\right)\right]. \quad (2.49)$$

We may re-express the derivative using the recurrence formula (Watson 1995, section 3.71)

$$K_{\nu-1}(z) + K_{\nu+1}(z) = -2K'_\nu(z) \quad (2.50)$$

to give

$$J'_n(ne) \sim \frac{1-e}{\sqrt{3}\pi}\left[K_{-2/3}\left(\frac{2^{3/2}\tilde{f}}{3}\right) + K_{4/3}\left(\frac{2^{3/2}\tilde{f}}{3}\right) - \frac{1}{\sqrt{2}\tilde{f}}K_{1/3}\left(\frac{2^{3/2}\tilde{f}}{3}\right)\right]. \quad (2.51)$$

And so finally we obtain the well-defined

$$B(\tilde{f}) = \frac{1}{\sqrt{3}\pi}\left[K_{-2/3}\left(\frac{2^{3/2}\tilde{f}}{3}\right) + K_{4/3}\left(\frac{2^{3/2}\tilde{f}}{3}\right) - \frac{1}{\sqrt{2}\tilde{f}}K_{1/3}\left(\frac{2^{3/2}\tilde{f}}{3}\right)\right]. \quad (2.52)$$

Having obtained expressions for $A(\tilde{f})$ and $B(\tilde{f})$ in terms of standard functions, we can calculate the energy spectrum for a parabolic orbit. From equation (2.37)

$$\frac{dE}{df} = \frac{4\pi^2}{5}\frac{G^3}{c^5}\frac{M_\bullet^2\mu^2}{r_p^2}\ell\left(\frac{f}{f_c}\right), \quad (2.53)$$

where we have used the limit

$$\ell(\tilde{f}) = \left[8\tilde{f}^2B(\tilde{f}) - 2\tilde{f}A(\tilde{f})\right]^2 + \left(128\tilde{f}^4 + \frac{4\tilde{f}^2}{3}\right)\left[A(\tilde{f})\right]^2. \quad (2.54)$$

This agrees with the $e = 1$ result of Turner (1977), which was computed by direct integration along unbound orbits. Figure 2.5 shows how $\ell(n, e)$ changes with eccentricity including our result for a parabolic encounter. Although more power is radiated into higher harmonics, the peak of the spectrum does not move much: it is always between $f = f_c$ and $f = 2f_c$, with $f = 2f_c$ for $e = 0$ and $f \simeq 1.637f_c$ for $e = 1$.

2.5.2.1 Total Energy

To check the validity of this limit we can calculate the total energy radiated by integrating equation (2.53) over all frequencies, or by summing the energy radiated into each harmonic. These must yield the same result. Summing:

$$E_{\text{sum}} = \frac{64\pi}{5}\frac{G^3}{c^5}\frac{M_\bullet^2\mu^2}{r_p^2}\omega_c(1-e)^{7/2}\sum_n g(n, e), \quad (2.55)$$

where we have used equations (2.31), (2.33) and (2.34). Peters & Mathews (1963) provide the result

$$\sum_n g(n, e) = \frac{1 + (73/24)e^2 + (37/96)e^4}{(1-e^2)^{7/2}}. \quad (2.56)$$

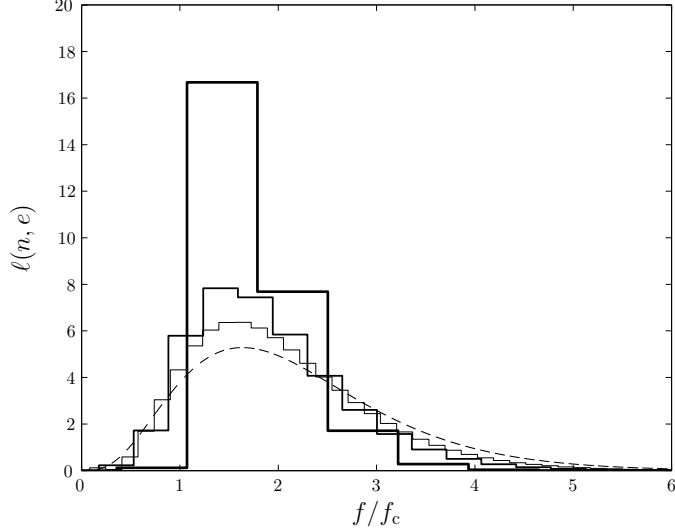


Figure 2.5 The relative energy (per orbit) spectrum $\ell(n, e)$ for $e = 0.2$ (heavy line), $e = 0.5$ (medium line), $e = 0.7$ (light line), and the limiting result for $e = 1$ (dashed line) versus frequency. Compare with figure 3 of Peters & Mathews (1963).

Using this,

$$E_{\text{sum}} = \frac{64\pi}{5} \frac{G^3}{c^5} \frac{M_\bullet^2 \mu^2}{r_p^2} \omega_c \frac{1 + (73/24)e^2 + (37/96)e^4}{(1+e)^{7/2}}, \quad (2.57)$$

which is perfectly well behaved as $e \rightarrow 1$,

$$E_{\text{sum}} = \frac{85\pi}{2^{5/2}3} \frac{G^3}{c^5} \frac{M_\bullet^2 \mu^2}{r_p^2} \omega_c. \quad (2.58)$$

Integrating the energy spectrum equation (2.53) gives

$$E_{\text{int}} = \frac{2\pi}{5} \frac{G^3}{c^5} \frac{M_\bullet^2 \mu^2}{r_p^2} \omega_c \int_0^\infty \ell(\tilde{f}) d\tilde{f}. \quad (2.59)$$

The integral can be evaluated numerically as

$$\int_0^\infty \ell(\tilde{f}) d\tilde{f} = 12.5216858\dots = \frac{425}{2^{7/2}3}. \quad (2.60)$$

The two total energies are consistent, $E_{\text{int}} = E_{\text{sum}}$.

2.5.3 Comparison

Two energy spectra are plotted in figure 2.6 for orbits with periapses of $r_p = 15.0r_g$, $30.0r_g$ and $60.0r_g$. The two spectra appear to be in good agreement, showing the same general shape in the weak-field limit. The NK spectrum is more tightly peaked, but is always within a factor of 2 at the apex. The peak of the spectrum is shifted to a marginally higher frequency in the NK spectrum primarily because of the addition of the current quadrupole and mass octupole terms.

Comparing the total energy fluxes, ratios of the various energies are plotted in figure 2.7. We introduce an additional energy here, the quadrupole NK energy $E_{\text{NK(Q)}}$.

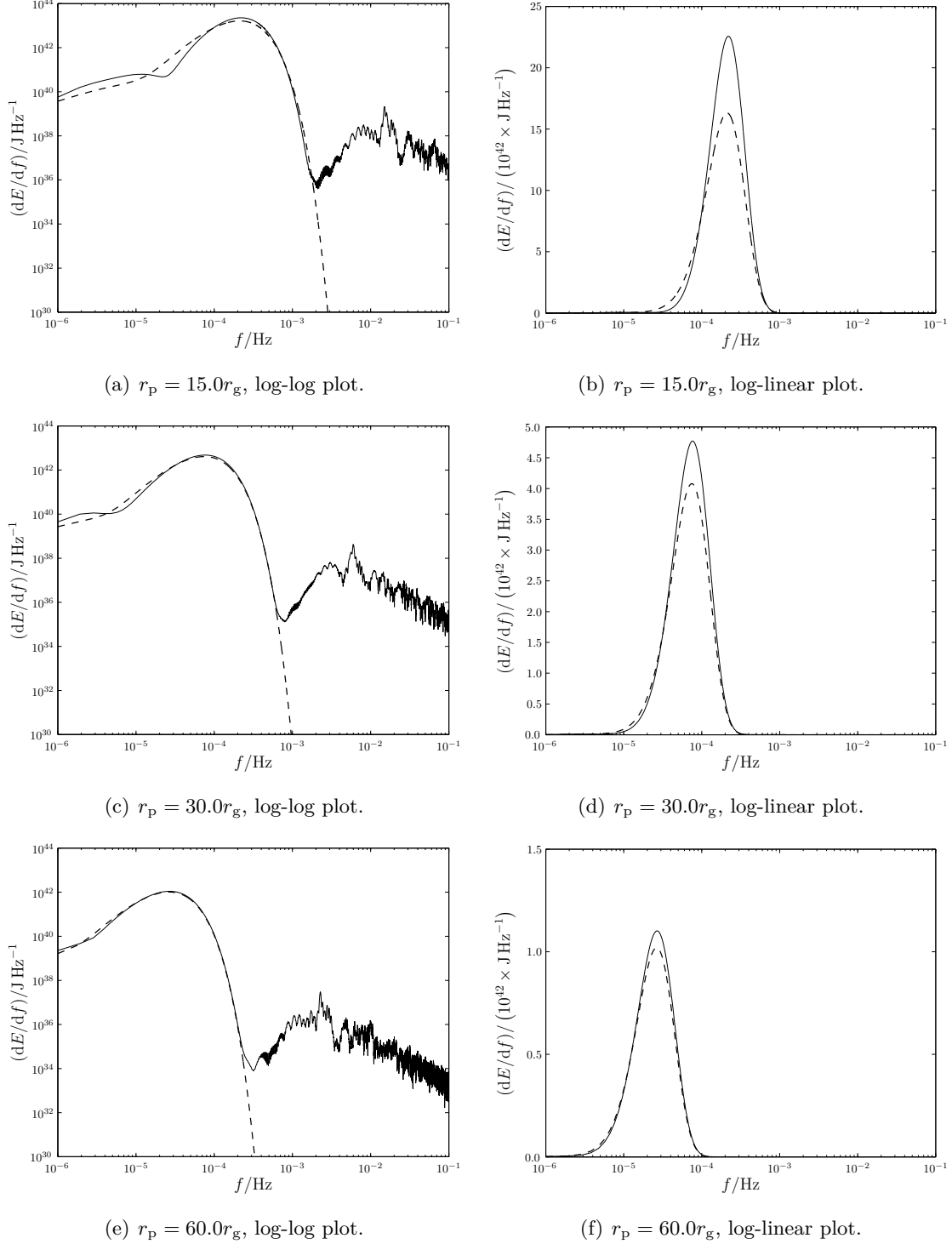


Figure 2.6 Energy spectra for a parabolic orbit of a $\mu = 10M_\odot$ object about a Schwarzschild BH with $M_\bullet = 4.31 \times 10^6 M_\odot$. The spectra calculated from the NK waveform is shown by the solid line and the Peters and Mathews flux is indicated by the dashed line. The NK waveform includes octupole contributions. The high frequency tail is the result of spectral leakage.

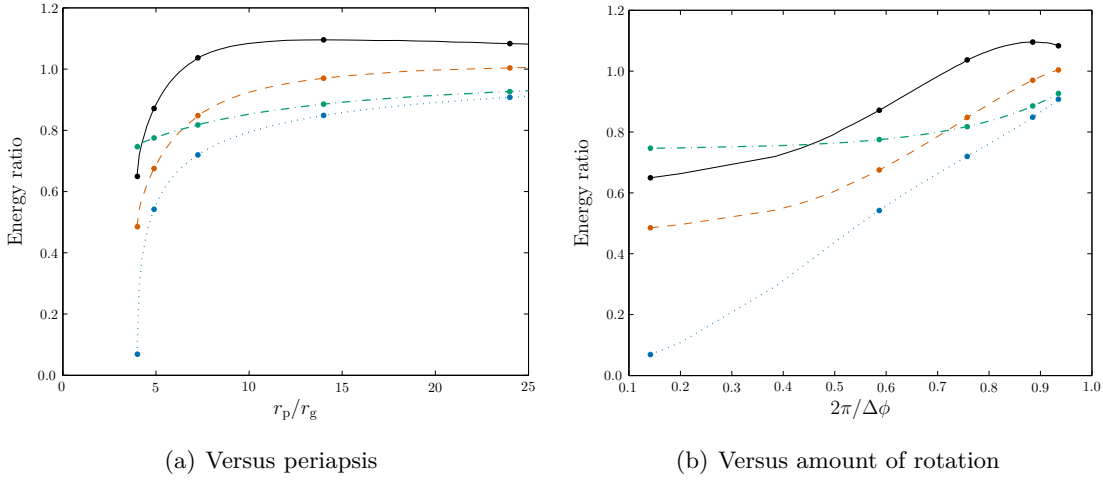


Figure 2.7 Ratios of energies as a function of periapsis r_p and 2π divided by the total angle of rotation in one orbit $\Delta\phi$ ($2\pi/\Delta\phi = 1$ for a Keplerian orbit). The solid line shows the ratio of the numerical kludge and Martel energies E_{NK}/E_M ; the dashed line shows the ratio of the NK energy calculated using only the mass quadrupole term and the Martel energy $E_{NK(Q)}/E_M$; the dot-dashed line shows the ratio of the quadrupole and quadrupole-octupole NK energies $E_{NK(Q)}/E_{NK}$, and the dotted line shows the ratio of the Peters and Mathews and quadrupole NK energies $E_{PM}/E_{NK(Q)}$. The spots show the mapping between the two abscissa scales. Compare with figure 4 of Gair *et al.* (2005).

This allows easier comparison with the Peters and Mathews energy which includes only quadrupole radiation. It can be calculated in three ways:

1. Inserting the waveform $\tilde{h}(f)$ generated including only the mass quadrupole term in equation (2.16) into equation (2.29) and integrating. This is equivalent to the method used to calculate E_{NK} .
 2. Numerically integrating the quadrupole GW luminosity (Misner *et al.* 1973, section 36.7; Hobson *et al.* 2006, section 18.7)

$$E = \frac{G}{5c^9} \int \ddot{\mathcal{I}}_{ij} \ddot{\mathcal{I}}^{ij} dt, \quad (2.61)$$

where $I_{ij} = I_{ij} - (1/3)I\delta_{ij}$ is the reduced mass quadrupole tensor. We can obtain this from equation (2.28), by integrating over all angles when the waveform only contains the mass quadrupole component. This has the advantage of avoiding the effects of spectral leakage or the influence of window functions.

3. Using the analytic expressions for the integral equation (2.61) from appendix A of Gair *et al.* (2005). The expressions are included in appendix C.

All three agree to within computational error. No difference is visible on the scale plotted in figure 2.7. This demonstrates the validity of the code.

We have used the amount of rotation $\Delta\phi$ as a convenient measure for the abscissa. For an equatorial orbit in Kerr spacetime,

$$\Delta\phi = 2 \int_{r_p}^{\infty} \frac{d\phi}{dr} dr = \sqrt{\frac{2}{M_\bullet}} L_z \int_{r_p}^{\infty} \frac{r^2 - 2M_\bullet(1-a/L_z)r}{(r^2 - 2M_\bullet r + a^2)w} dr, \quad (2.62)$$

where

$$w^2 = r^3 - \frac{L_z^2}{2M_\bullet} r^2 + (L_z - a)^2 r; \quad (2.63)$$

L_z is the specific angular momentum about the z -axis; a is the spin parameter, and we have adopted units with $G = c = 1$. We shall find it useful to define

$$r_\pm = M_\bullet \pm \sqrt{M_\bullet^2 - a^2}, \quad (2.64)$$

and the two nonzero roots of the cubic w^2

$$r_{p,1} = \frac{L_z^2}{4M_\bullet} \pm \sqrt{\frac{L_z^4}{16M_\bullet^2} - (L_z - a)^2}; \quad (2.65)$$

the periapsis is the larger root $r_p > r_1$. This equation implicitly gives L_z as a function of r_p . The integral may be rewritten as

$$\Delta\phi = \sqrt{\frac{2}{M}} L_z \int_{r_p}^{\infty} \frac{1}{w} \left(1 + \frac{\alpha_+}{r - r_+} + \frac{\alpha_-}{r - r_-} \right) dr, \quad (2.66)$$

where

$$\alpha_\pm = \pm \frac{2M_\bullet r_\pm - a^2 L_z}{2L_z \sqrt{M^2 - a^2}}. \quad (2.67)$$

This may be evaluated using elliptic integrals (Gradshteyn & Ryzhik 2000, 3.131.8, 3.137.8)

$$\Delta\phi = 2L_z \sqrt{\frac{2}{r_p M}} \left[\frac{\alpha_+}{r_+} \Pi \left(\frac{r_+}{r_p} \middle| \frac{r_1}{r_p} \right) + \frac{\alpha_-}{r_-} \Pi \left(\frac{r_-}{r_p} \middle| \frac{r_1}{r_p} \right) \right], \quad (2.68)$$

where $\Pi(n|m) = \int_0^{\pi/2} d\vartheta / (1 - n \sin^2 \vartheta) \sqrt{1 - m \sin^2 \vartheta}$ is the complete elliptic integral of the third kind. In the limit of $a \rightarrow 0$ we recover the Schwarzschild result (Cutler & Flanagan 1994)

$$\Delta\phi = 2L_z \sqrt{\frac{2}{r_p M}} K \left(\frac{r_1}{r_p} \right), \quad (2.69)$$

where $K(m) = \int_0^{\pi/2} d\vartheta / \sqrt{1 - m \sin^2 \vartheta}$ is the complete elliptic integral of the first kind.

The ratios all tend towards one in the weak field, as required, but differences become more pronounced in the strong field. The NK energy is larger than the Peters and Mathews result E_{PM} . This behaviour has been seen before for high eccentricity orbits about a non-spinning BH (Gair *et al.* 2005). It may be explained by considering the total path length for the different orbits: the Peters and Mathews spectrum assumes a Keplerian orbit, the orbit in Kerr geometry rotates more than this. The greater path length leads to increased emission of GWs and a larger energy flux. Our bead must travel further along its wire. A good proxy for the path length is the angle of rotation

$\Delta\phi$; this is 2π for a Keplerian orbit, in Kerr the angle should be 2π in the limit of an infinite periapsis, whereas for a periapsis small enough that the orbit shows zoom-whirl behaviour, the total angle may be many times 2π . There is a reasonable correlation between the amount of rotation $2\pi/\Delta\phi$ and the ratio of energies.

Error in the NK energy compared with the time-domain BH perturbation theory results of Martel comes from two sources: the neglecting of higher order multipole contributions and the ignoring of background curvature. The contribution of the former can be estimated by looking at the difference in the NK energy by including the current quadrupole and mass octupole terms. From figure 2.7 we see that these terms give a negligible contribution in the weak field, but the difference is $\sim 20\%$ in the strong field. This explains why the Martel energy E_M is greater in the strong field, as it includes contributions from all multipoles. Neglecting the background curvature increases the NK energy relative to E_M . This partially cancels out the error introduced by not including higher order terms: this accidentally leads to $E_{NK(Q)}$ being more accurate than E_{NK} for $r_p \gtrsim 10r_g$ (Tanaka *et al.* 1993).

From the level of agreement we may be confident that the NK waveforms are a reasonable approximation. The difference in energy flux is only greater than 10% for very strong fields $r_p \simeq 4r_g$; since this is dependent on the square of the waveform, typical accuracy in the waveform may be $\sim 5\%$ (Gair *et al.* 2005; Tanaka *et al.* 1993).

2.6 Summary

We have outlined an approximate method of generating gravitational waveforms for extreme-mass-ratio bursts. This assumes that the orbits are parabolic and employs a numerical kludge approximation. The waveforms created appear to be consistent with results obtained using Peters and Mathews waveforms for large periapses, indicating that they have the correct weak-field form. The NK approach should be superior to that of Peters and Mathews in the strong-field regime as it uses the exact geodesics of the Kerr spacetime. Comparisons with energy fluxes from BH perturbation theory indicate that typical waveform accuracy may be of order 5%, but this is worse for orbits with small periapses and may be $\sim 20\%$.

In the following chapters we use these waveforms to access what information can be extracted from EMRBs about their source systems, in particular the mass and spin of the MBH. We shall focus on the Galaxy's MBH as this is the most promising candidate for sourcing EMRBs.

Chapter 3

Parameter estimation and Galactic bursts

Extreme-mass-ratio bursts could provide a means of investigating the properties of MBHs with a space-borne detector. In the previous chapter we constructed approximate burst waveforms. We now begin to investigate their properties. To be useful for astronomy EMRBs must be: (i) detectable, (ii) informative and (iii) likely to happen. If bursts are not detectable, they can be of no use. If they are detectable but not informative, then at best they could only tell us that there are objects on highly eccentric orbits. This could be interesting if we observe enough to do statistics, but this depends upon the event rate. If the event rate is too low, then even if EMRBs are wonderfully informative they are unlikely to be of practical use. EMRBs must fulfill all three criteria to be a viable tool for learning about MBHs.

In this chapter we start to address the first two criteria. We begin by concentrating on the Galaxy's MBH; as it is our local MBH, it is the most promising candidate. In section 3.1 we look at our NK waveforms and determine that they could be detectable. We give fiducial power-law fits for SNR as a function of periapse radius, which are useful for back-of-the-envelope estimates. We explain how to extract the information from the bursts in section 3.2. Results estimating the measurement precision are then presented in section 3.3.

3.1 Waveforms and detectability

3.1.1 Model parameters

The waveform depends on the properties of the MBH; the CO and its orbit, and the detector. We assume the position of the detector is known. This is specified by $\bar{\phi}$ and φ . We chose the initial position so $\bar{\phi} = 0$ when $\varphi = 0$ (Cutler 1998); this does not

qualitatively influence our results.¹

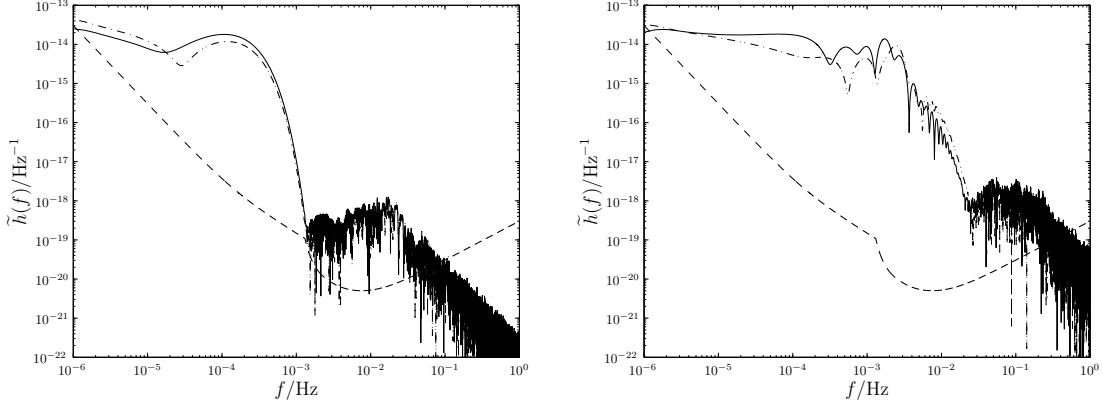
We also treat the sky position of the MBH, given by $\bar{\Theta}$ and $\bar{\Phi}$, as known. These are taken as the coordinates of Sgr A*, as the radio source is expected to be within $20r_g$ of the MBH (Reid *et al.* 2003; Doeleman *et al.* 2008). We use the J2000.0 coordinates (Reid *et al.* 1999; Yusef-Zadeh *et al.* 1999). These change with time due to the rotation of the SS about the GC; the proper motion is about 6 mas yr^{-1} , mostly in the plane of the galaxy (Reid *et al.* 1999; Backer & Sramek 1999; Reid *et al.* 2003). The position is already determined to high accuracy and an EMRB can only give weak constraints on source position, hence we shall not try to infer it.²

For our model, the input parameters left to infer are:

1. The MBH's mass M_\bullet . This is currently well constrained by the observation of stellar orbits about Sgr A* (Ghez *et al.* 2008; Gillessen *et al.* 2009), with the best estimate being $M_\bullet = (4.31 \pm 0.36) \times 10^6 M_\odot$. This depends upon the galactic centre distance R_0 as $M_\bullet = (3.95 \pm 0.06|_{\text{stat}} \pm 0.18|_{R_0, \text{stat}} \pm 0.31|_{R_0, \text{sys}}) \times 10^6 M_\odot (R_0/8 \text{ kpc})^{2.19}$, where the errors are statistical, independent of R_0 ; statistical from the determination of R_0 , and systematic from R_0 respectively.
2. The spin parameter a_* . Naively this could be anywhere in the range $|a_*| < 1$; however it is possible to place an upper bound by contemplating spin-up mechanisms. Considering the torque from radiation emitted by an accretion disc, and swallowed by a BH, it can be shown that $|a_*| \lesssim 0.998$ (Thorne 1974). Magnetohydrodynamical simulations of accretion discs produce a smaller maximum value of $|a_*| \sim 0.95$ (Gammie *et al.* 2004). The actual spin value could be much lower than this upper bound depending upon the MBH's evolution.
- 3, 4. The orientation angles for the MBH spin Θ_K and Φ_K . These are defined in the ecliptic coordinate system from figure 2.3.
5. The ratio of the SS-GC distance R_0 and the CO mass μ , which we denote as $\zeta = R_0/\mu$. This scales the amplitude of the waveform. Bursts, unlike inspirals, do not undergo orbital evolution, hence we cannot break the degeneracy in R_0 and μ , and they cannot be inferred separately. The distance, like M_\bullet , is constrained by stellar orbits, the best estimate being $R_0 = 8.33 \pm 0.35 \text{ kpc}$ (Gillessen *et al.* 2009). The mass of the orbiting particle depends upon the type of object: whether it is an MS star, WD, NS or BH. Since we shall not know the μ precisely, we shall not be able to infer anything more about the distance to the GC.
- 6, 7. The angular momentum of the CO. This can be described using either $\{L_z, Q\}$ or

¹See Jani *et al.* (2013) for a discussion of the possibilities for optimising the choice of the initial phase.

²For comparison, an EMRI, which should be more informative, can only give sky localisation to $\sim 10^{-3}$ steradians (Barack & Cutler 2004; Huerta & Gair 2009).



(a) Waveform for $a_* \simeq 0.12$, $r_p \simeq 15.6r_g$ and $i \simeq 2.1$. The SNR for the spherical polar kludge waveform (plotted) is $\rho[\mathbf{h}_{\text{sph}}] \simeq 451$, for the oblate-spheroidal kludge it is $\rho[\mathbf{h}_{\text{ob}}] \simeq 451$ (agreement to 0.01%).

(b) Waveform for $a_* \simeq 0.74$, $r_p \simeq 3.2r_g$ and $i \simeq 1.2$. The SNR for the spherical polar kludge waveform (plotted) is $\rho[\mathbf{h}_{\text{sph}}] \simeq 70600$, for the oblate-spheroidal kludge it is $\rho[\mathbf{h}_{\text{ob}}] \simeq 74900$.

Figure 3.1 Example burst waveforms from the galactic centre. The strain $\tilde{h}_I(f)$ is indicated by the solid line, $\tilde{h}_{II}(f)$ by the dot-dashed line, and the noise curve by the dashed line. The kludge has been formulated using spherical polar coordinates.

$\{L_\infty, i\}$. We employ the latter, as the total angular momentum and inclination are less tightly correlated. Assuming spherical symmetry, we expect $\cos i$ to be uniformly distributed.

- 8–10. A set of coordinates to specify the trajectory. These could be positions at an arbitrary time. We use the angular phases at perapse, ϕ_p and χ_p (which determines θ_p), as well as the time of perapse t_p .

We are therefore interested in constraining $d = 10$ parameters. We shall use λ to represent the set of these d parameters.

Of paramount importance are the mass and spin. Together, these fully describe the MBH, all the information regarding its formation and growth must be inferred from these parameters. As we have a good estimate of the mass, to gain a complete description of the MBH we have only to measure its spin; this shall give us insight into its history and role in the evolution of the Galaxy.

3.1.2 Waveforms and kludge coordinates

Figure 3.1 shows example waveforms to demonstrate some of the possible variations in the signal. All these assume the standard mass and position for the MBH as well as a $\mu = 10M_\odot$ orbiting CO; other (randomly chosen) orbital parameters are specified in the captions. Radii are given in terms of the gravitational radius $r_g = GM_\bullet/c^2$.

The plotted waveforms use the spherical polar coordinate system for the NK. Using

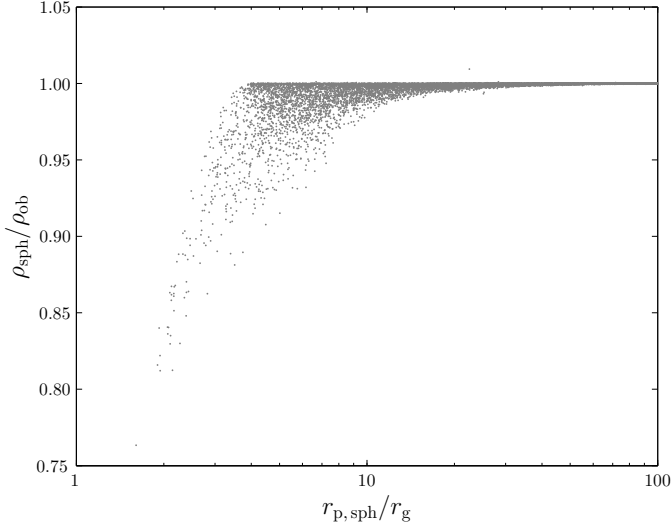


Figure 3.2 Ratio of SNR for a waveform calculated using spherical polar coordinates to that for a waveform using oblate-spheroidal coordinates.

oblate-spheroidal coordinates makes a small difference. On the scale shown here the only discernible difference would be in figure 3.1(b); the maximum difference in that waveform (outside the high-frequency tail) is $\sim 10\%$. In the other cases the difference is entirely negligible (except in the high-frequency tail, which is not of physical significance). This behaviour is typical; for the closest orbits, with the most extreme spin parameters, the maximum difference in the waveforms may be $\sim 30\%$. The difference is largely confined to the higher frequency components, which are most sensitive to the parts of the trajectory closer to the MBH: the change in flat-space radius for the same Boyer–Lindquist radial coordinate causes a slight shift in the shape of the spectrum. Enforcing the same flat-space periapsis gives worse agreement across the spectrum.

To examine the effect of the coordinate choice, we compare SNRs calculated using the alternative schemes for a selection of orbits. The orbits have periapse distances uniformly distributed in log-space between the innermost orbit and $100r_g$. Each had a spin and orbital inclination randomly chosen from distributions uniform in a_* and $\cos \iota$.³ For every periapse, five SNRs were calculated, each having a different set of ancillary parameters specifying the relative orientation of the MBH, the orbital phase and the position of the detector, drawn from appropriate uniform distributions. We take the mean of $\ln \rho$ for each set of ancillary parameters.⁴ The MBH parameters were fixed as for the GC.

The ratio of the two SNRs is shown in figure 3.2. The difference from the coordinate

³The innermost orbit depends upon a_* and ι , hence these are drawn first.

⁴The logarithm is a better quantity to work with since the SNR is a positive-definite quantity that may be distributed over a range of magnitudes (MacKay 2003, sections 22.1, 23.3). Using median values yields results that are quantitatively similar.

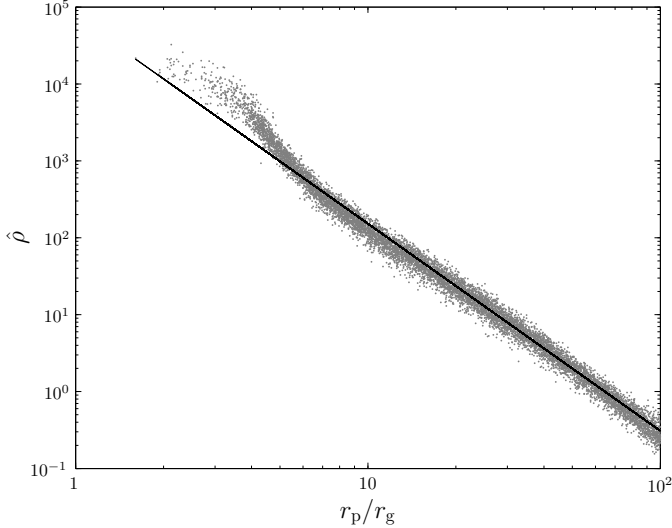


Figure 3.3 Mass-normalised SNR as a function of periapse radius for LISA. The plotted points are the values obtained by averaging over each set of ancillary parameters. The best fit line is $\log(\hat{\rho}) = -2.69 \log(r_p/r_g) + 4.88$. This is fitted to orbits with $r_p > 13.0r_g$.

systems is only apparent for orbits with very small periapses. There is agreement to 10% down to $r_p \simeq 4r_g$; the maximal difference may be expected to be $\sim 20\%$, this is for periapses that are only obtainable for high spin values.

Since the deviation in the two waveforms is only apparent for small periapses, when the kludge approximation is least applicable, we conclude that the choice of coordinates is unimportant. The potential error of order 10% is no greater than that inherent in the NK approximation (see section 2.5). Without an accurate waveform template to compare against, we do not know if there is a preferable choice of coordinates. We adopt spherical coordinates for easier comparison with existing work.

3.1.3 Signal-to-noise ratios

The detectability of a burst depends upon its SNR. To characterise the variation of ρ we calculated SNRs for a range of orbits. These were generated as in section 3.1.2, we used $\sim 10^4$ different periapse distances.

The bursts were calculated for a $1M_\odot$ CO. From equation (2.16), the amplitude of the waveform is proportional to the CO mass μ , and so ρ is also proportional to μ ; a $10M_\odot$ object would be ten times louder on the same orbit. To make results mass independent, we work in terms of a mass-normalised SNR

$$\hat{\rho}[\mathbf{h}] = \left(\frac{\mu}{M_\odot} \right)^{-1} \rho[\mathbf{h}]. \quad (3.1)$$

There exists a correlation between the periapse radius and SNR, as shown in figure 3.3. Closer orbits produce louder bursts. To reflect this trend, we have fitted a simple fiducial

power law,

$$\log \rho \simeq -2.7 \log \left(\frac{r_p}{r_g} \right) + \log \left(\frac{\mu}{M_\odot} \right) + 4.9, \quad (3.2)$$

which is indicated by the straight line.⁵ This was done by maximising the likelihood, assuming $\ln \rho$ has a Gaussian distribution with standard deviation derived from the scatter because of variation in the ancillary parameters. The power law is a good fit only for larger periapses. The shape is predominately determined by the noise curve. The change in the trend reflects the transition from approximately power law behaviour to the bucket of the noise curve. Hence, we fit a power law to orbits with a characteristic frequency of $f_* = \sqrt{GM_\bullet/r_p} < 1 \times 10^{-3}$ Hz, to avoid spilling into the bucket.⁶ Changing the cut-off within a plausible region alters the fit coefficients by around 0.1.⁷

The SNR shows no clear correlation with the other parameters (excluding μ). However, the SNR is sensitive to the orbital parameters, in particular the initial position, and may vary by an order of magnitude.

Setting a threshold of $\rho = 10$, a $1M_\odot$ ($10M_\odot$) object would be expected to be detectable if the periapse distance is less than $27r_g$ ($65r_g$). Hopman *et al.* (2007), assuming a threshold of $\rho = 5$, used an approximate form for the SNR based upon the quadrupole component of a circular orbit; their model, with updated parameters for the MBH, predicts bursts would be detectable out to $66r_g$ ($135r_g$). This is overly optimistic.

Following a similar approach, we may repeat this analysis for eLISA. The SNR as a function of periapse is shown in figure 3.4. There is again a strong correlation that may be approximated as a power law. The bucket of the noise curve is less apparent as it is shifted to slightly higher frequencies. We have fitted

$$\log \rho \simeq -2.9 \log \left(\frac{r_p}{r_g} \right) + \log \left(\frac{\mu}{M_\odot} \right) + 3.9, \quad (3.3)$$

which is indicated by the straight line. This was done in exactly the same as for LISA. Again, there is no clear correlation with any other orbital parameters.

The SNR is lower for eLISA. As a consequence, bursts are detectable across a smaller range of periapses. Using the threshold $\rho = 10$, a $1M_\odot$ ($10M_\odot$) object would be expected to be detectable if the periapse distance is less than $10r_g$ ($21r_g$). This is a reduction of about a factor of three compared to LISA.

3.2 Parameter estimation

Having detected a signal, we are interested in what we can learn about the source. We have an inference problem that can be solved by an application of Bayes' Theorem

⁵Using oblate-spheroidal coordinates instead of spherical polars gives a fit consistent to within 0.1% as we have excluded the closest orbits.

⁶The form of f_* can be derived on dimensional grounds, but it is explained in more detail in section 4.1.

⁷The power law exponent -2.7 is inconsistent with $-13/4$ as predicted by the approximate model of Hopman *et al.* (2007). This is the result of their approximate waveform model.

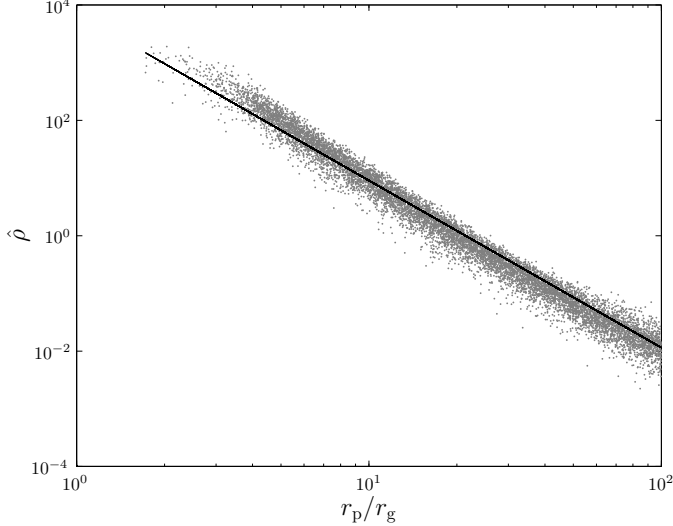


Figure 3.4 Mass-normalised SNR as a function of periapse radius for eLISA. The plotted points are the values obtained by averaging over each set of ancillary parameters. The best fit line is $\log(\hat{\rho}) = -2.90 \log(r_p/r_g) + 3.85$. This is fitted to orbits with $r_p > 13.0r_g$.

(Jaynes 2003, chapter 4): the probability distribution for our parameters given that we have detected the signal $\mathbf{s}(t)$ is given by the posterior

$$p(\boldsymbol{\lambda}|\mathbf{s}(t)) = \frac{p(\mathbf{s}(t)|\boldsymbol{\lambda})p(\boldsymbol{\lambda})}{p(\mathbf{s}(t))}. \quad (3.4)$$

Here $p(\mathbf{s}(t)|\boldsymbol{\lambda})$ is the likelihood of the parameters, $p(\boldsymbol{\lambda})$ is the prior probability distribution for the parameters, and the evidence $p(\mathbf{s}(t)) = \int p(\mathbf{s}(t)|\boldsymbol{\lambda}) d^d\lambda$ is, for our purposes, a normalising constant. The likelihood depends upon the realization of noise. If parameters $\boldsymbol{\lambda}_0$ define a waveform $\mathbf{h}_0(t) = \mathbf{h}(t; \boldsymbol{\lambda}_0)$, the probability that we observe signal $\mathbf{s}(t)$ GW is given by equation (2.23), so the likelihood is

$$p(\mathbf{s}(t)|\boldsymbol{\lambda}_0) \propto \exp \left[-\frac{1}{2} (\mathbf{s} - \mathbf{h}_0 | \mathbf{s} - \mathbf{h}_0) \right]. \quad (3.5)$$

If we were to define this as a probability distribution for the parameters $\boldsymbol{\lambda}$, the modal values are the maximum-likelihood (ML) parameters $\boldsymbol{\lambda}_{\text{ML}}$. The waveform $\mathbf{h}(t; \boldsymbol{\lambda}_{\text{ML}})$ is the signal closest to $\mathbf{s}(t)$, where distance is defined using the inner product (2.19) (Cutler & Flanagan 1994).

To discover if any parameters can be accurately inferred, we must characterise the form of the posterior. We discuss two approaches for mapping the shape of the posterior: Fisher matrices and Markov chain Monte Carlo (MCMC) sampling.

3.2.1 Fisher matrices

In the limit of a high SNR, we may approximate (Vallisneri 2008)

$$p(\mathbf{s}(t)|\boldsymbol{\lambda}_0) \propto \exp \left[-\frac{1}{2} (\partial_a \mathbf{h} | \partial_b \mathbf{h}) (\lambda^a - \langle \lambda^a \rangle_\ell) (\lambda^b - \langle \lambda^b \rangle_\ell) \right], \quad (3.6)$$

where the mean is defined as

$$\langle \lambda^a \rangle_\ell = \frac{\int \lambda^a p(\mathbf{s}(t)|\boldsymbol{\lambda}) d^d \lambda}{\int p(\mathbf{s}(t)|\boldsymbol{\lambda}) d^d \lambda}. \quad (3.7)$$

In the high SNR limit, this is the ML value $\langle \lambda^a \rangle_\ell = \lambda_{\text{ML}}^a$. The quantity

$$\Gamma_{ab} = (\partial_a \mathbf{h} | \partial_b \mathbf{h}) \quad (3.8)$$

is the Fisher information matrix (FIM). It controls the variance of the likelihood distribution.

The form of the posterior distribution depends upon the nature of the prior information. If we have an uninformative prior, such that $p(\boldsymbol{\lambda})$ is a constant, the posterior distribution is determined by the likelihood. In the high SNR limit, we obtain a Gaussian with variance-covariance matrix

$$\boldsymbol{\Sigma} = \boldsymbol{\Gamma}^{-1}. \quad (3.9)$$

The FIM therefore gives the uncertainty associated with the inferred parameters, in this case the ML values.

If the prior restricts the allowed range for a parameter, as is the case for the spin a_* , then the posterior is a truncated Gaussian, and $\boldsymbol{\Gamma}^{-1}$ may no longer represent the variance-covariance.

If the prior is approximately Gaussian with variance-covariance matrix $\boldsymbol{\Sigma}_0$, the posterior is also Gaussian.⁸ The posterior variance-covariance is (Cutler & Flanagan 1994; Vallisneri 2008)

$$\boldsymbol{\Sigma} = (\boldsymbol{\Gamma} + \boldsymbol{\Sigma}_0^{-1})^{-1}. \quad (3.10)$$

From this the inverse FIM $\boldsymbol{\Gamma}^{-1}$ is an upper bound on the size of the posterior covariance matrix.⁹

The FIM gives a quick way of estimating the range of the posterior. It is widely used because of this. However, it is only appropriate when the approximation of equation (3.6) holds. This is known as the linearised-signal approximation (LSA), where higher order derivatives are neglected. To assess the validity of this, Vallisneri (2008) recommends use of the maximum-mismatch (MM) criterion

$$\ln r = -\frac{1}{2} \left(\Delta \lambda^a \partial_a \mathbf{h}_{\text{ML}} - \Delta \mathbf{h} \Big| \Delta \lambda^b \partial_b \mathbf{h}_{\text{ML}} - \Delta \mathbf{h} \right). \quad (3.11)$$

Here $\Delta \boldsymbol{\lambda}$ is the displacement to some point on the 1σ surface

$$\Delta \boldsymbol{\lambda} = \boldsymbol{\lambda}_{1\sigma} - \boldsymbol{\lambda}_{\text{ML}}, \quad (3.12)$$

⁸If we only know the typical value and spread of a parameter, a Gaussian is the maximum entropy prior (Jaynes 2003, section 7.11): the prior that is least informative given what we know.

⁹It is also the Cramér-Rao bound on the error covariance of an unbiased estimator (Cutler & Flanagan 1994; Vallisneri 2008). Thus it represents the frequentist error: the lower bound on the covariance for an unbiased parameter estimator $\boldsymbol{\lambda}_{\text{est}}$ calculated from an infinite set of experiments with the same signal $\mathbf{h}(t)$ but different realisations of the noise $\mathbf{n}(t)$.

and $\Delta \mathbf{h}$ is the corresponding change in the waveform

$$\Delta \mathbf{h} = \mathbf{h}(\boldsymbol{\lambda}_{1\sigma}) - \mathbf{h}(\boldsymbol{\lambda}_{\text{ML}}). \quad (3.13)$$

The 1σ surface is defined from the inverse of the FIM. If higher order terms are indeed negligible, the MM criterion is small. We check this by picking a random selection of points on the 1σ surface and evaluating $|\ln r|$. If this is smaller than a fiducial value ($|\ln r| = 0.1$) over the majority (90%) of the surface we consider the LSA sufficiently justified.

We calculated FIMs for a wide range of orbits and checked the MM criterion. We found that for the overwhelming majority the test failed: the LSA is not appropriate. This behaviour was seen even for orbits with $\rho \sim 10^3\text{--}10^4$.¹⁰ Higher order terms are important, and cannot be neglected.

EMRBs have a short duration and accordingly are not the most informative of signals. Therefore, the 1σ surface as defined by considering only the LSA terms is large. Taking such a step in parameter space moves the signal beyond the region of linear changes.

What constitutes high SNR depends upon the signal; it is not enough for $\rho > 1$. As stressed by Vallisneri (2008), it is essential to check the MM criterion for individual waveforms: the threshold for the LSA to become applicable could be much greater than naively thought.

As we cannot be confident in FIM results, we abandon this approach in favour of using Markov chain Monte Carlo simulations to explore constraints from different regions of parameter space. These are computationally more expensive, but do not rely on any approximations.

3.2.2 Markov chain Monte Carlo methods

MCMC methods are widely used for inference problems; they are a family of algorithms for integrating over complicated distributions and are efficient for high-dimensional problems (MacKay 2003, chapter 29). Parameter space is explored by constructing a chain of N samples. The distribution of points visited by the chain maps out the underlying distribution; this becomes asymptotically exact as $N \rightarrow \infty$. Samples are added sequentially, if the current state is $\boldsymbol{\lambda}_n$ a new point $\boldsymbol{\lambda}^*$ is drawn and accepted with probability

$$\mathcal{A} = \min \left\{ \frac{\pi(\boldsymbol{\lambda}^*) \mathcal{L}(\boldsymbol{\lambda}^*) \mathcal{Q}(\boldsymbol{\lambda}_n; \boldsymbol{\lambda}^*)}{\pi(\boldsymbol{\lambda}_n) \mathcal{L}(\boldsymbol{\lambda}_n) \mathcal{Q}(\boldsymbol{\lambda}_n; \boldsymbol{\lambda}^*)}, 1 \right\}, \quad (3.14)$$

setting $\boldsymbol{\lambda}_{n+1} = \boldsymbol{\lambda}^*$, where $\mathcal{L}(\boldsymbol{\lambda})$ is the likelihood, in our case from equation (3.5); $\pi(\boldsymbol{\lambda})$ is the prior, and \mathcal{Q} is a proposal distribution. If the move is not accepted $\boldsymbol{\lambda}_{n+1} = \boldsymbol{\lambda}_n$. This is the Metropolis-Hastings algorithm (Metropolis *et al.* 1953; Hastings 1970).

¹⁰In this study, to increase ρ we must reduce the periapse distance; this also reduces the region where the LSA is valid as parameter dependencies become more non-linear. If we had the luxury of increasing ρ by moving the GC closer, things could be different.

Waiting long enough yields an exact posterior, but it is desirable for the MCMC to converge quickly. This requires a suitable choice for the proposal distribution, which can be difficult, since we do not yet know the shape of the target distribution.

One method to define the proposal is to use the previous results in the chain and refine \mathcal{Q} by learning from these. Such approaches are known as adaptive methods. Updating using previous points means that the chain is no longer Markovian. Care must be taken to ensure that ergodicity is preserved and convergence obtained (Roberts & Rosenthal 2007; Andrieu & Thoms 2008). To avoid this complication, we follow Haario *et al.* (1999), and use the adapting method as a burn in phase. We have an initial phase where the proposal is updated based upon accepted points. After this we fix the proposal and proceed as for a standard MCMC. By only using samples from the second part, we guarantee that the chain is Markovian and ergodic, whilst still enjoying the benefits of a tailor-made proposal. After only a finite number of samples we cannot assess the optimality of this (Andrieu & Thoms 2008), but the method is still effective.

To tune \mathcal{Q} , we use an approach based upon the adaptive Metropolis algorithm (Haario *et al.* 2001). The proposal is taken to be a multivariate normal distribution centred upon the current point, the covariance of which is

$$\mathbf{C} = s(\mathbf{V}_n + \varepsilon\mathbf{C}_0), \quad (3.15)$$

where \mathbf{V}_n is the covariance of the accepted points $\{\boldsymbol{\lambda}_1, \dots, \boldsymbol{\lambda}_n\}$, s is a scaling factor that controls the step size, ε is a small positive constant (typically 2.5×10^{-3}), and \mathbf{C}_0 is a constant matrix included to ensure ergodicity.

Our adaptation is run in three phases. The initial phase is to get the chain moving. For this $\mathbf{C}_0^{\text{init}}$ is a diagonal matrix with elements calibrated from initial one dimensional MCMCs. This finishes after N_{init} accepted points.

For the second phase, we use the proposal covariance from the initial phase \mathbf{C}^{init} for $\mathbf{C}_0^{\text{main}}$. We reset the covariance of the accepted points so that it only includes points from this phase. This is the main adaptation phase and lasts until N_{main} points have been accepted.

In the final adaptation phase we restart the chain at the true parameter values. We no longer update the shape of the covariance (\mathbf{V}_n remains fixed), but adjust the step size s to tune the acceptance rate; it is then fixed, along with everything else, for the final MCMC.

Throughout the adaptation, we update the step size s after every 100 trial points (whether or not they are accepted). While updating, the covariance \mathbf{V}_n changes after every 10^3 trial points. We set $N_{\text{init}} = 5 \times 10^4$ and $N_{\text{main}} = 4.5 \times 10^5$.

We initially aimed for an acceptance rate of 0.234; this is optimal for a random walk Metropolis algorithm with some specific high-dimensional target distributions (Roberts *et al.* 1997; Roberts & Rosenthal 2001). In many cases we found better convergence when aiming for a lower acceptance rate, say 0.1. This is not unexpected: the optimal rate may

be lower than 0.234 when the parameters are not independent and identically distributed (Bédard 2007, 2008b,a). In practice, the final acceptance rate is (almost always) lower than the target rate as the use of a multivariate Gaussian for the proposal distribution is rarely a good fit at the edges of the posterior. Consequently, the precise choice for the target acceptance rate is unimportant as long as it is of the correct magnitude. Final rates are typically within a factor of 2 of the target value. As an initial choice, we set $s = 2.38^2/d$, which is the optimal choice if \mathbf{C} was the true target covariance for a high dimensional target of independent and identically distributed parameters (Gelman *et al.* 1996; Roberts *et al.* 1997; Roberts & Rosenthal 2001; Haario *et al.* 2001).¹¹

To assess the convergence of the MCMC we check the trace plot (the parameters' values throughout the run) for proper mixing, that the one and two dimensional posterior plots fill out to a smooth distribution, and that the distribution widths tend towards consistent values.

3.3 Results for Galactic bursts

To asses the utility of EMRBs for parameter estimation, we studied bursts from a range of orbits with periapses uniformly distributed in logarithmic space between the innermost orbit and $16r_g$. Parameters were chosen as in section 3.1.2. The MBH was assumed to have the standard mass and position and the CO was chosen to be $10M_\odot$, as the most promising candidates for EMRBs would be BHs: they are massive and hence produce higher SNR bursts, they are more likely to be on close orbits as a consequence of mass segregation (Bahcall & Wolf 1977; Alexander & Hopman 2009), and they cannot be tidally disrupted.

The results of the MCMC runs show strong and complex parameter dependencies. Some example results are shown in figure 3.5, 3.6 and 3.7. The first is well-behaved. It is almost Gaussian, but we see some asymmetries and imperfections. There are also strong degeneracies, indicated by needle-like distributions. This is a fairly standard example: there are runs which are closer to being Gaussian (especially at higher SNR), and equally there are tighter correlations. The lenticular $M_\bullet - L_\infty$ degeneracy is common.

The second shows banana-like degeneracies. These are not uncommon; there are varying degrees of curvature. The more complicated shape makes it harder for the MCMC to converge, so the final distribution is not as smooth as for the first example. The curving degeneracies also bias the one dimensional marginalisations away from the true values.

The third shows more intricate behaviour. This is more rare, but indicates the variety of shapes that is obtainable. Again the convergence is more difficult, so the distributions

¹¹Reasonably good results may be obtained by fixing s at this value, and not adjusting to fine tune the acceptance rate.

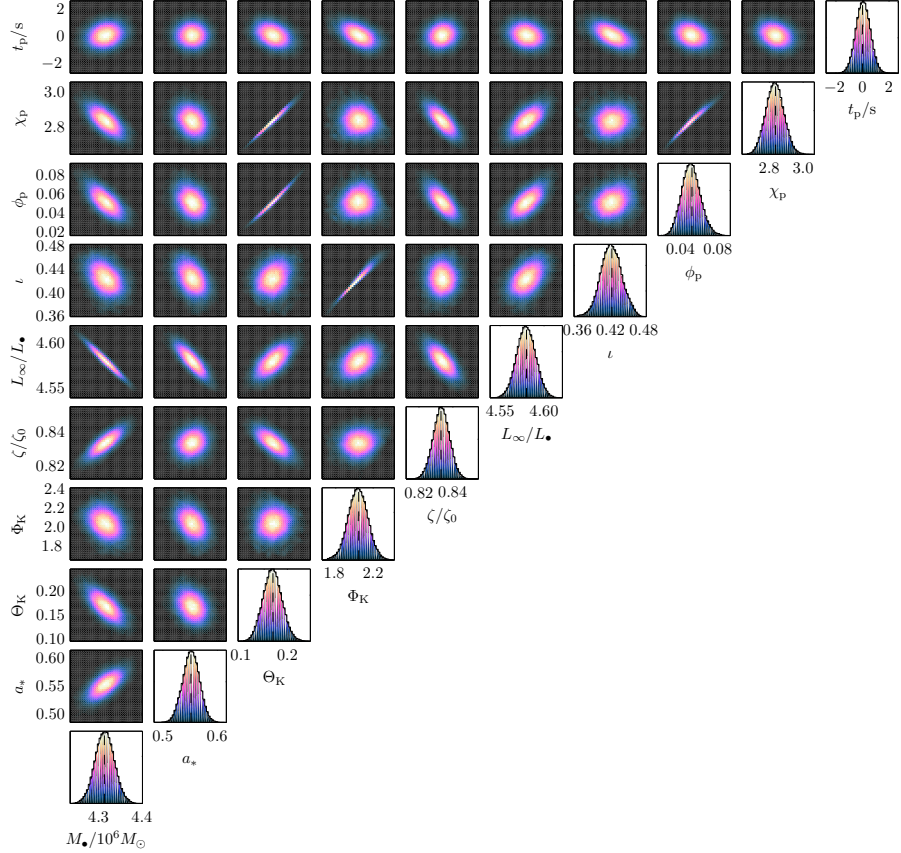


Figure 3.5 Marginalised one- and two-dimensional posteriors. The scales are identical in both sets of plots. The dotted line indicates the true value. These distributions are fairly cromulent and well converged. Angular momentum is in units of $L_\bullet = GM_\bullet c^{-1}$ and the scaled distance is in units of $\zeta_0 = 1M_\odot^{-1}$ kpc. The input orbit has $r_p \simeq 8.54r_g$ and $\rho \simeq 916$.

are rougher around the edges; there is also some biasing due to the curving degeneracies.

Our results do not incorporate any priors (save to keep them within realistic ranges); we have not folded in the existing information we have, for example, about the MBH's mass. Therefore, the resulting distributions characterise what we could learn from EMRBs alone. By the time a space-borne GW detector finally flies, we will have much better constraints on some parameters.

It is possible to place good constraints from the closest orbits. These can provide sufficient information to give beautifully behaved posteriors although significant correlation between parameters persists.

3.3.1 Distribution widths

3.3.1.1 Characterising distributions

Having recovered the posterior distribution it is necessary to quantify the accuracy to which parameters could be measured. If the posterior were Gaussian, this can be done

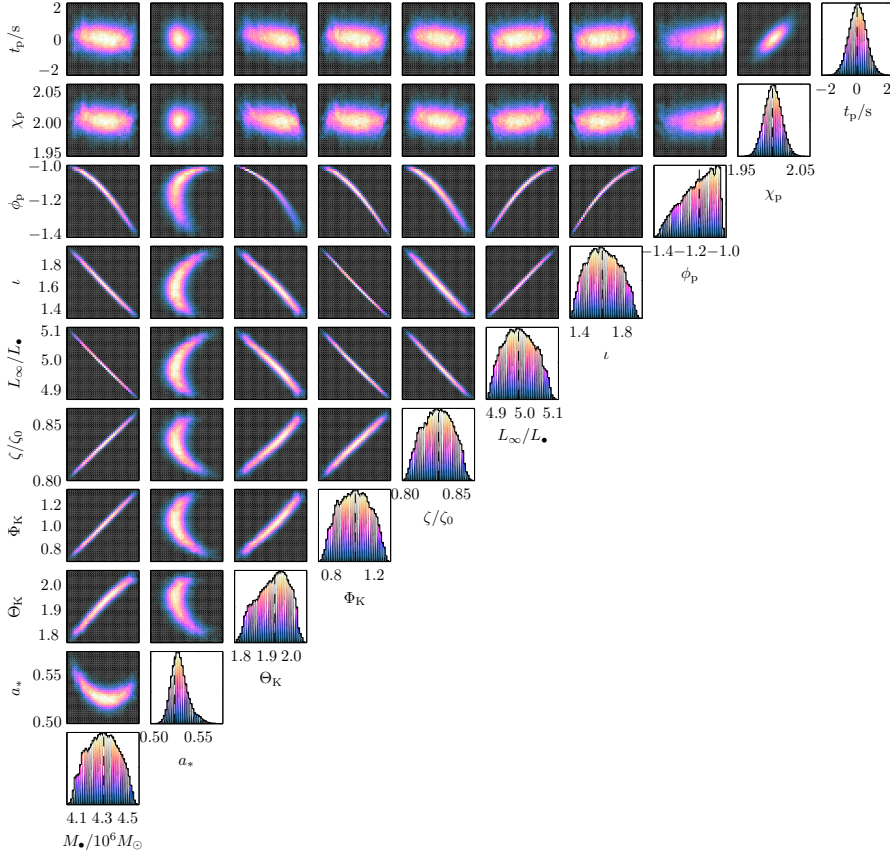


Figure 3.6 Marginalised one- and two-dimensional posteriors. The conventions are the same as in figure 3.5. These distributions show definite non-gaussianity. The input orbit has $r_p \simeq 9.86r_g$ and $\rho \simeq 1790$.

just by using the standard deviation σ_{SD} . An alternative is to use the range that encloses a given probability, but this is misleading if the distribution is multimodal. A robust means of characterising the width is by using a k -dimensional (k -d) tree.

A k -d tree is a type of binary space partitioning tree (de Berg *et al.* 2008, sections 5.2, 12.1, 12.3). It is constructed by splitting the parameter space into two by finding the median point in one dimension. The two pieces are then split by finding their medians in another dimension. This continues recursively until the desired number of partitions, known as leaves, has been created. When applied to a sampled probability distribution, a k -d tree has smaller leaves in the regions of high probability which are of most interest (Weinberg 2012). It builds a natural decomposition of the parameter space, giving a means of binning samples.

For a given probability p , the corresponding confidence region is the smallest area of parameter space in which we expect that the true values lie with that probability. A simple means of constructing a confidence range is to find the smallest combination of k -d tree leaves that contain the desired probability. To do this we rank the leaves by size; the smallest corresponds to the highest probability area and is the starting point for the

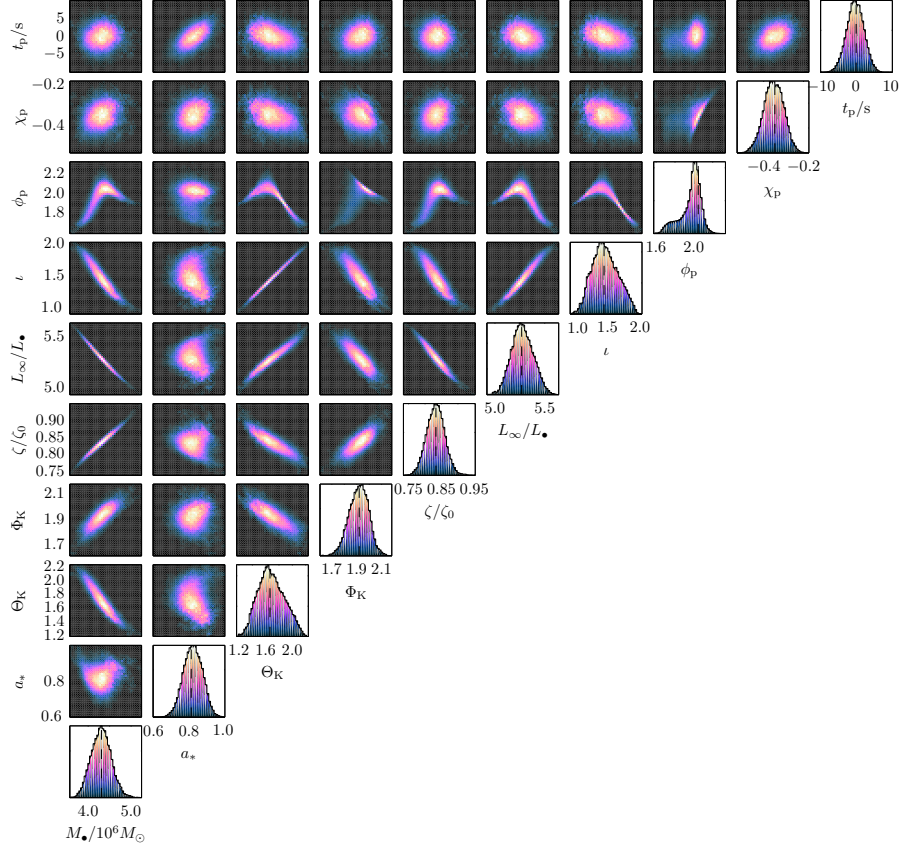


Figure 3.7 Marginalised one- and two-dimensional posteriors. The conventions are the same as in figure 3.5. These distributions show complicated degeneracies. The input orbit has $r_p \simeq 11.60r_g$ and $\rho \simeq 590$.

confidence range. We continue adding the next smallest leaf until the total probability enclosed is p . Summing the areas of the leaves gives an estimate for the range.

However, this approach is biased. Whenever a random fluctuation in the sampling gives an excess of points in one area the overdensity leads to a smaller leaf size and then the preferential inclusion of that leaf in the confidence interval. Conversely, an underdensity leads to a larger leaf that is liable to be external to the confidence range. If there are a small number of points per leaf we shall overstate our confidence as the constructed range is too small.¹²

Biassing may be avoided by using a two-step method which separates the creation and ordering of the partitions from the building of the confidence range (Sidery *et al.* 2013). This is done by dividing our data into two disjoint random samples.¹³ The first is

¹²This can be visualised by considering the simple example of dividing in two samples from a one dimensional uniform distribution. We would expect one partition to be more densely populated than the other because of random fluctuations, and we shall always pick this smaller leaf as our $p = 0.5$ confidence range. As the number of points increases we expect that this bias would decrease.

¹³We split our data into two equal parts. This may not be the optimal rationing, but is a sensible first guess. Some preliminary experimentation shows that it is not too important, provided that the splitting

used to construct the k -d tree in the standard way. The leaves are then ordered by size. We then use the second set to populate the leaves. We again start with the smallest leaf and work down the ranking until the encompassed probability is p . The total range is the estimate for the p confidence level.

The first step creates bins that are of appropriate resolution. We therefore have the benefit of using a k -d tree. By using an independent set of points to build the confidence level, we eliminate any bias because there should be no correlation in fluctuations between the two sets. Any leaves that are too small are expected to receive a below average number of points in the second step and any that are too large are expected to receive more. This corrects the expectation for the confidence level.

In this case, we are interested in the confidence levels for the marginalised distributions for each parameter. We therefore construct 1-d trees, which are easily implemented. We have a large number of points and low dimensionality so biasing should not be an issue. To characterise our distributions we find the $p = 0.68$ confidence range and take the half-width of this, which we denote as $\sigma_{0.68}$.

3.3.1.2 Parameter uncertainties

Characteristic distribution widths σ_{SD} and $\sigma_{0.68}$ are shown in figure 3.8. Filled circles are used for runs that appear to have converged. Open circles are for those yet to converge, but which appear to be approaching an equilibrium state; widths should be accurate to within a factor of a few. For guidance, the dotted line corresponds to the current measurement uncertainty for M_\bullet ; the dashed lines are σ_{SD} from uniform priors for a_* , Φ_K , ϕ_p , χ_p , $\cos \Theta_K$ and $\cos \iota$, and the dot-dashed line are the equivalent $\sigma_{0.68}$. We have no expectations for the width of the MBH mass distribution with respect to the current value. However, we would expect that the recovered distributions for the other parameters are narrower than for the case of complete ignorance; this bound does seem to be respected. The two widths, σ_{SD} and $\sigma_{0.68}$, typically agree better at smaller periapses and higher SNRs as would be expected for more Gaussian distributions.

The widths show a trend of decreasing with decreasing periapsis or increasing SNR, but there is a large degree of scatter. There does not appear to be a strong dependence upon any single input parameter, with the exception of the spin. The widths for ι , Θ_K , Φ_K , ϕ_p and χ_p increase for smaller spin magnitudes. The dependence is shown in figure 3.9. These parameters are defined with reference to the coordinate system established by the spin axis: for $a_* = 0$ we have spherical symmetry and there would be ambiguity in defining them. Therefore, it makes sense that they can be more accurately determined for larger spin magnitudes. The width for a_* , however, shows no clear correlation.

Comparing our MCMC and FIM results, we see there can be significant differences.

is not too unbalanced. The point at which this occurs depends upon the underlying distribution.

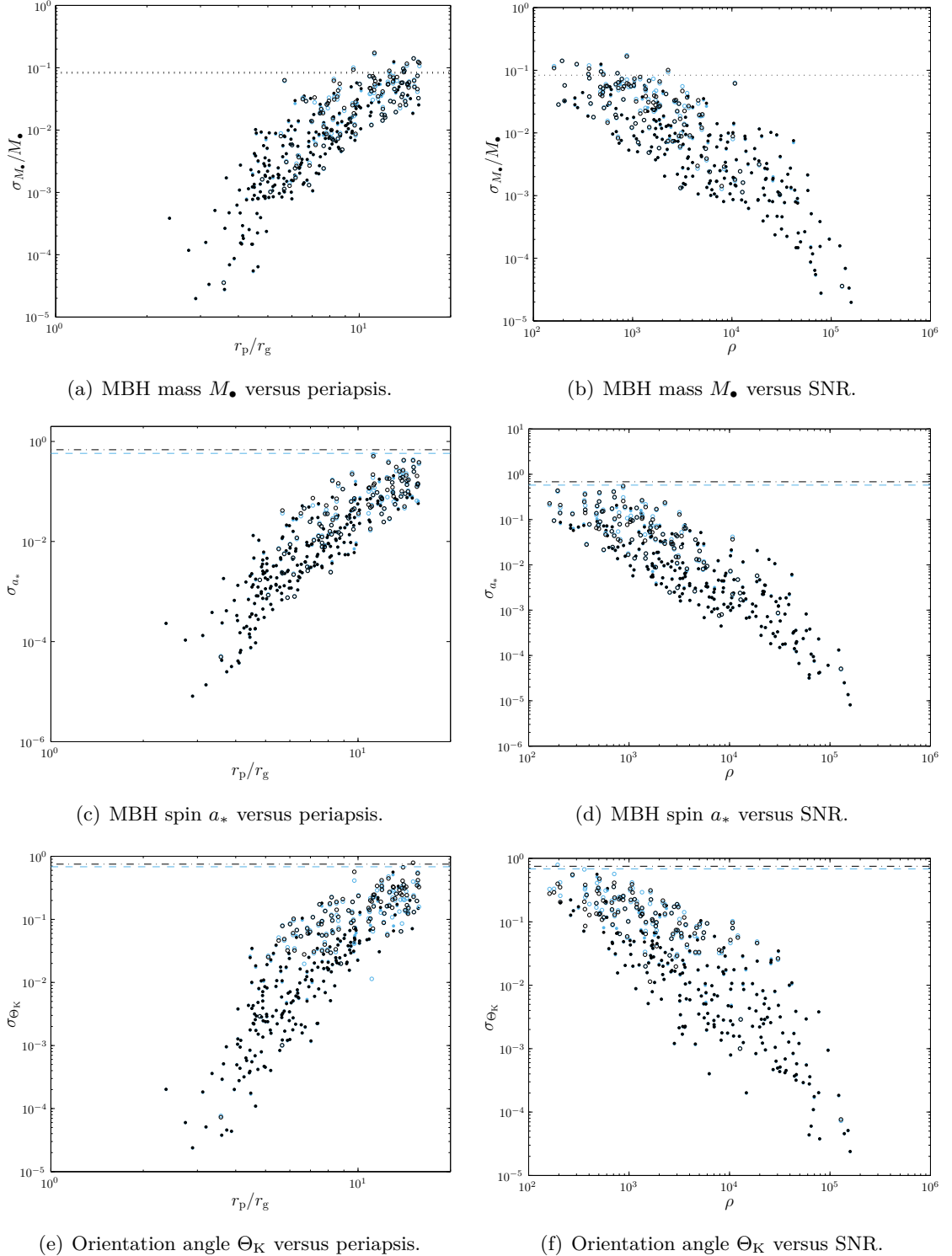


Figure 3.8 Distribution widths as functions of periaxis r_p and SNR ρ . The light blue points are used for the standard deviation, the black for the 68-percentile half-width. The filled circles are converged runs and the open circles for those yet to converge. The dotted line is the current uncertainty for M_\bullet . The dashed line is the standard deviation for an uninformative prior and the dot-dashed line is the equivalent 68-percentile half-width.

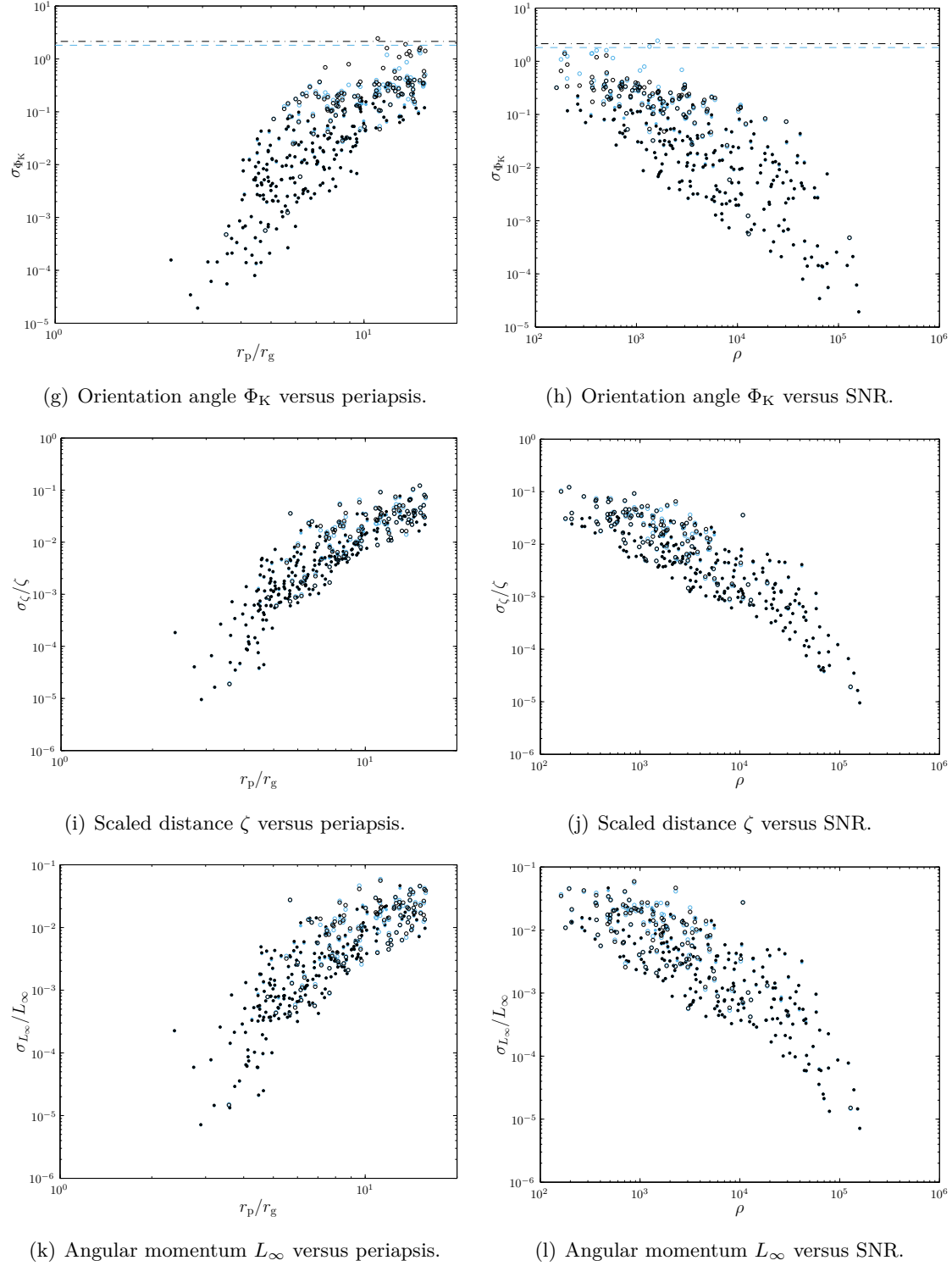


Figure 3.8 (Continued) Distribution widths as functions of periapse r_p and SNR ρ .

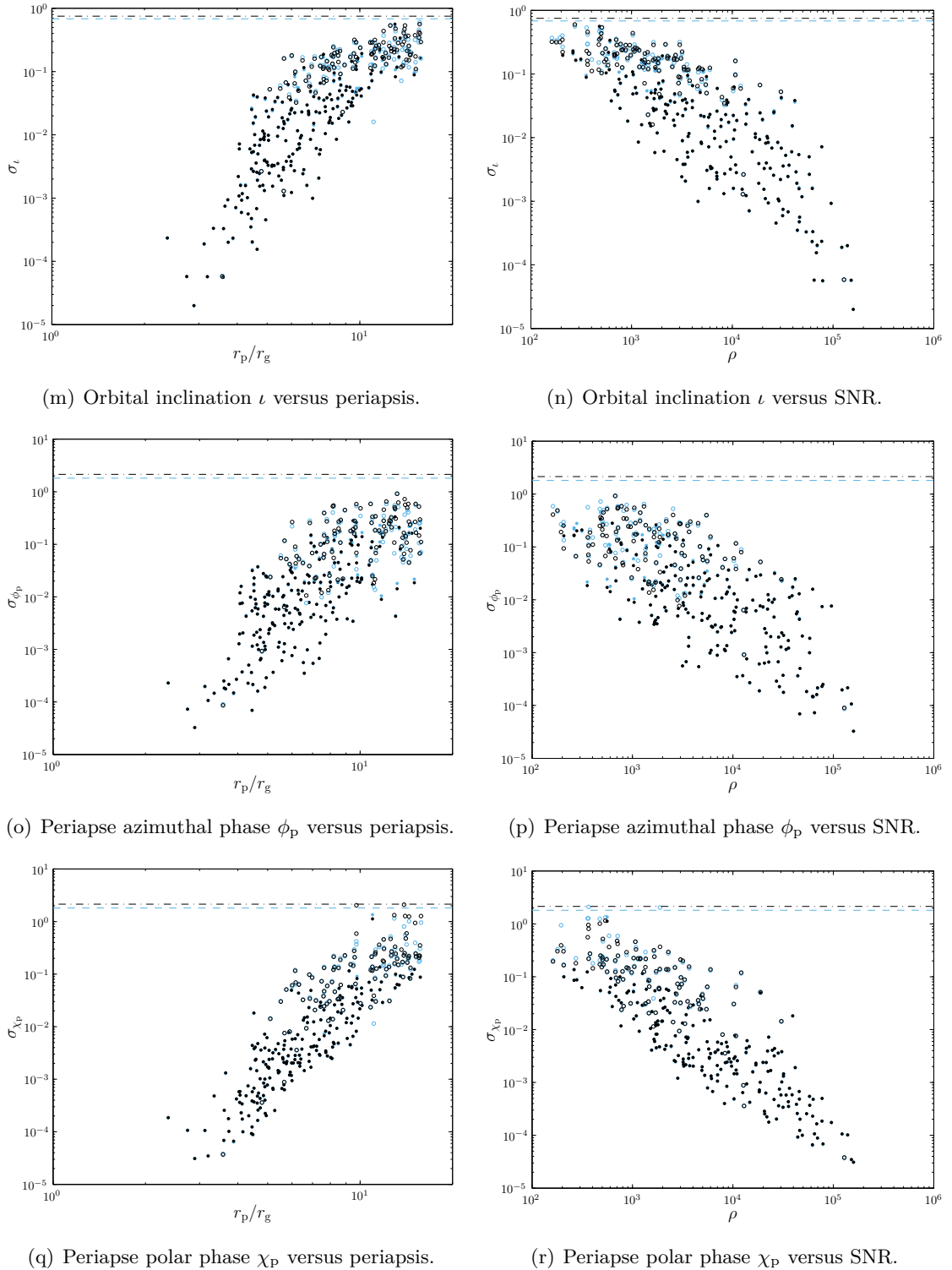


Figure 3.8 (Continued) Distribution widths as functions of periapse r_p and SNR ρ .

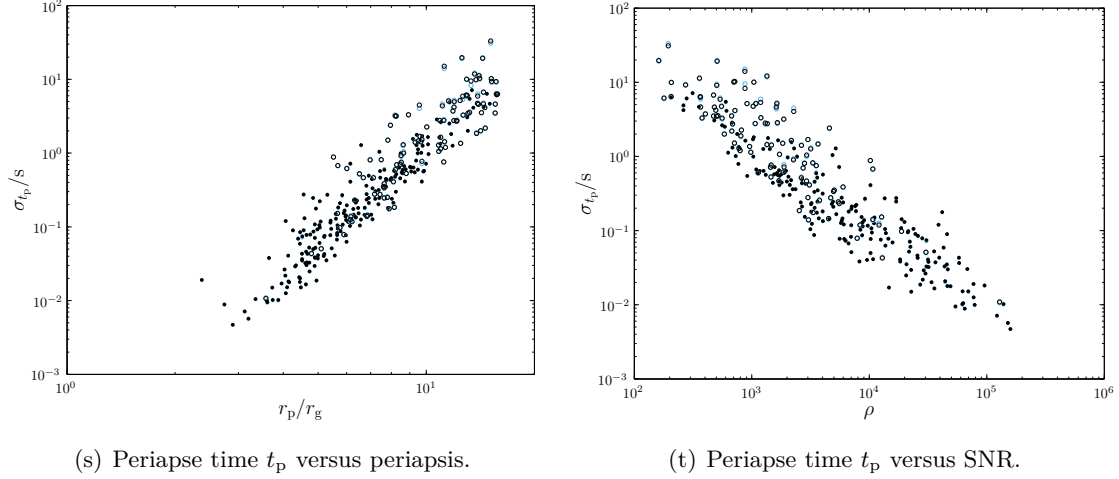


Figure 3.8 (Concluded) Distribution widths as functions of periapsis r_p and SNR ρ .

Most parameters give results consistent to within an order (or two) of magnitude. The best agreement is for t_p , which is largely uncorrelated with the other parameters. The widths for M_\bullet , a_* , L_∞ and ι show more severe differences; these parameters show the tightest degeneracies. The two methods do show signs of slowly converging with increasing SNR, as expected.

As a consistency check, to verify that the mismatch between the FIM and MCMC results is a consequence of parameter correlations, we calculated one-dimensional FIMs, only varying the MBH mass, and compared these to widths computed from MCMCs only sampling in mass. These were found to be in good agreement. The majority ($\sim 87\%$) have standard deviations consistent to within a factor of two; the rest within an order of magnitude.¹⁴ Some small difference is expected because of numerical error from calculating derivatives for the FIM by finite differencing.

3.3.2 Scientific potential

Having quantified the precision with which we could infer parameters from an EMRB waveform, we can now consider if it is possible to learn anything new.

Of paramount interest are the MBH mass and spin. The current uncertainty in the mass is $\sigma_{M_\bullet} = 0.36 \times 10^6 M_\odot$ ($\sim 8\%$; Gillessen *et al.* 2009). There are few runs amongst our data set that are not better than this: it appears that orbits of a $\mu = 10M_\odot$ CO with periapses $r_p \lesssim 13r_g$ should be able to match our current observational constraints. However, the EMRB is an independent measurement, and so a measurement of comparable precision to the current bound can still be informative. Accuracy of 1% could be possible if $r_p \lesssim 8r_g$.

¹⁴One differed by more than an order of magnitude, and also failed to fulfil the (one dimensional) MM criterion; this was a numerical problem in calculating the FIM.

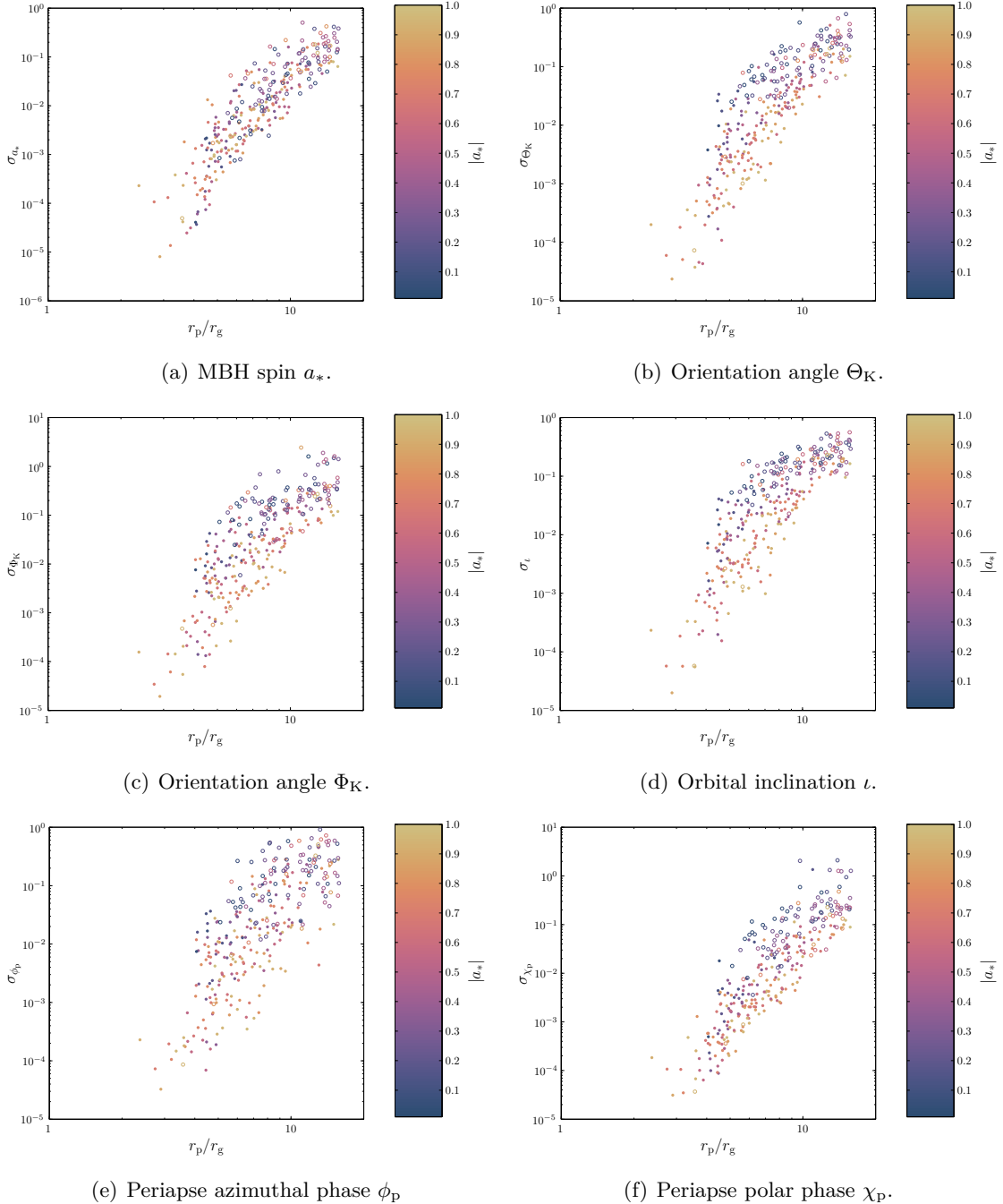


Figure 3.9 Parameter standard deviations versus periapsis r_p , showing dependence (or lack thereof) upon the spin magnitude $|a_*|$.

The spin is less well constrained. To obtain an uncertainty for the magnitude of 0.1, comparable to that achieved in X-ray measurements of active galactic nuclei, it appears that the periapsis needs to be $r_p \lesssim 11r_g$. For smaller periapses, the uncertainty can be much less, indicating that an EMRB could be an excellent probe. The orientation angles for the spin axis may be constrained to better than 0.1 for $r_p \lesssim 11r_g$. It may well be possible to learn both the direction and the magnitude of the spin. This could illuminate the MBH's formation.

We have no *a priori* knowledge about the CO or its orbit, so anything we learn would be new. However, this is not particularly useful information, unless we observe multiple bursts, and can start to build up statistics for the dynamics of the GC. Using current observations for the distance to the GC, which could be further improved by the mass measurement from the EMRB, it is possible to infer a value for the mass μ from ζ . This could inform us of the nature of the object (BH, NS or WD) and be a useful consistency check. A small value of ζ , indicating a massive CO, is unambiguous evidence for the existence of a stellar-mass BH.

3.4 Summary and conclusions

We have analysed the properties of EMRBs from the Galactic Centre. We used NK waveforms built using spherical polar and oblate spheroidal coordinates. The two coordinate schemes yield almost indistinguishable results. There may be differences when the spin is large and the periapse is small: $\sim 10\%$ for $r_p \simeq 4r_g$, $\sim 20\%$ for $r_p \simeq 2r_g$. This is less than the error inherent in the semirelativistic approximation inferred from the difference in NK and BH perturbation theory energy fluxes in section 2.5. We conclude that either is a valid choice for this purpose and have adopted spherical polar coordinates.

The SNR of bursts is well correlated with the periapsis, it can be reasonably described as having a power-law dependence. Using LISA, signals should be detectable for a $1M_\odot$ ($10M_\odot$) object if the periapse is $r_p < 27r_g$ ($r_p < 65r_g$), corresponding to a physical scale of 1.7×10^{11} m (4.1×10^{11} m) or 5.6×10^{-6} pc (1.3×10^{-5} pc). Using eLISA, these distances are approximately three times smaller.

We conducted an investigation using Fisher matrix analysis into how precisely we could infer parameters of the GC's MBH. However, we found that the linearised-signal approximation does not hold for these bursts over a wide range of SNR. This demonstrates the necessity of checking the approximation before quoting the results of an analysis (Vallisneri 2008).

We used MCMC results as a more robust measure of parameter estimation accuracy. Potentially, it is possible to determine very precisely the key parameters defining the MBH's mass and spin, if the orbit gets close enough to the MBH. It appears that we can achieve good results from a single EMRB with periapsis of $r_p \simeq 10r_g$ for a $10M_\odot$

CO. This translates to a distance of 6×10^{10} m or 2×10^{-6} pc. Orbits closer than this would place stricter constraints. The best orbits yield uncertainties of almost one part in 10^5 for the MBH mass and spin, far exceeding existing techniques. Conversely, orbits with $r_p \gtrsim 16r_g$ are unlikely to provide any useful information.

Before we can quote results for how accurately we can determine the various parameters, we must consider the probability of each orbit. This shall be done in

We have so far only considered EMRBS from our Galaxy, a natural extension is to consider bursts from extragalactic sources, which do in the next chapter. Extragalactic bursts are not as promising as those from the GC, but could still make a significant contribute to the total burst event rate.

Chapter 4

Extragalactic bursts

It is well established that space is big (Adams 1979, chapter 8). The Milky Way, our own island universe, is but one of a multitude of galaxies. Each one of these may have an MBH nestled at its core (Lynden-Bell & Rees 1971; Sołtan 1982). We have considered measuring the properties of the Galaxy's MBH using EMRBs and found that bursts can be informative if the periapsis is small enough. In this chapter, we extend this work to other nearby galaxies. If extragalactic EMRBs are detectable, they may be useful for constraining the properties of those galaxies' MBHs.

We use the NK waveforms from chapter 2 and the data analysis techniques from chapter 3. In section 4.1 we discuss the detectability of EMRBs from extragalactic sources. We show that bursts from other galaxies could be detected with LISA or eLISA. Following this, in section 4.2, we present examples of the constraints we could place using EMRBs. We conclude in section 4.3 with a discussion of our findings.

4.1 Detectability of extragalactic bursts

Whether or not a burst is detectable is determined by its SNR. This is calculated using equation (2.21). We assume a detection threshold of $\rho = 10$ as in section 3.1.3. The SNR of an EMRB depends upon many parameters; for a given MBH, the most important is the periapse radius r_p . There is a good correlation between ρ and r_p . Other parameters specifying the inclination of the orbit, the orientation of the system with respect to the detector, or the MBH spin only produce scatter about this trend. The form of the ρ - r_p relation depends upon the noise curve.

We parametrize the detectability in terms of a characteristic frequency f_* . The speed at periapse scales like $v \sim \sqrt{GM/r_p}$; the characteristic time taken for the position to change is then $T \sim r_p/v$, and so we define the characteristic frequency as

$$f_* = \sqrt{\frac{GM_\bullet}{r_p^3}}. \quad (4.1)$$

This allows comparison between different systems where the same periapse does not correspond to the same frequency and thus the same point of the noise curve.

We also expect the SNR to scale with other quantities. We define a characteristic strain amplitude for a burst h_0 ; we expect $\rho \propto h_0$, where the proportionality will be set by a frequency-dependent function that includes the effect of the noise curve. Assuming that the strain is dominated by the quadrupole contribution (Misner *et al.* 1973, section 36.10; Hobson *et al.* 2006, section 17.9) we expect

$$h_0 \sim \frac{G}{c^6} \frac{\mu}{R} \frac{d^2}{dt^2} (r^2), \quad (4.2)$$

where μ is the CO mass, R is the distance to the MBH, t is time and r is a proxy for the position of the orbiting object. The characteristic rate of change is set by f_* and the characteristic length-scale is set by r_p . Hence

$$h_0 \sim \frac{G}{c^6} \frac{\mu}{R} f_*^2 r_p^2 \quad (4.3)$$

$$\sim \frac{G^{5/2}}{c^6} \frac{\mu}{R} f_*^{-2/3} M_\bullet^{2/3}. \quad (4.4)$$

Using this, we can factor out the most important dependences to give a scaled SNR defined by

$$\rho_* = \left(\frac{\mu}{M_\odot} \right)^{-1} \left(\frac{R}{\text{Mpc}} \right) \left(\frac{M_\bullet}{10^6 M_\odot} \right)^{-2/3} \rho. \quad (4.5)$$

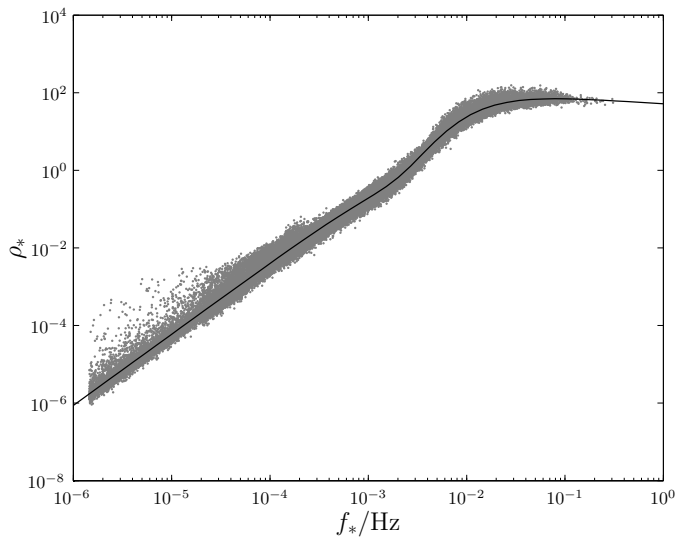
Space-based detectors are most sensitive to extreme-mass-ratio signals originating from systems containing MBHs with masses $\sim 10^6 M_\odot$. Higher mass objects produce signals at too low frequencies. We considered several nearby MBHs that were likely candidates for detectable burst signals. Details are given in table 4.1. For each, we calculated SNRs at $\sim 10^4$ different periapse distances, uniformly distributed in log space between the innermost orbit and $100r_g$ following the procedure in section 3.1.2: for each periapse, five SNRs were calculated using different sets of ancillary parameters specifying the spin magnitude and orientation of the MBH, the orbital inclination and phase, and the position of the detector.

The scaled SNRs are plotted in figure 4.1. The plotted points are the average values of $\ln \rho_*$ calculated for each periapse distance. The curve shows that EMRB SNR does scale as expected, and ρ_* can be described as a one-parameter curve. There remains some scatter about this: the larger scatter at low frequencies is a consequence of numerical noise from dealing with very low SNRs from Andromeda; removing the averaging over ancillary parameters increases the scatter to be typically about an order of magnitude in total. However, the fit is good enough for rough calculations.

We approximate the trend with a parametrized curve

$$\rho_* = \alpha_1 \left(\frac{f_*}{\text{Hz}} \right)^{\beta_1} \left[1 + \left(\alpha_2 \frac{f_*}{\text{Hz}} \right)^{\beta_2} \right] \left[1 + \left(\alpha_3 \frac{f_*}{\text{Hz}} \right)^{\beta_3} \right]^{-\beta_4}. \quad (4.6)$$

Galaxy	$M_\bullet/10^6 M_\odot$	R/Mpc	References
Milky Way (Sgr A*)	4.31 ± 0.36	0.00833	Gillessen <i>et al.</i> (2009)
Andromeda (M31, NGC 224)	140^{+90}_{-30}	0.770	Bender <i>et al.</i> (2005); Karachentsev <i>et al.</i> (2004)
M32 (NGC 221)	2.5 ± 0.5	0.770	Verolme <i>et al.</i> (2002); Karachentsev <i>et al.</i> (2004)
Circinus	1.1 ± 0.2	2.82	Graham (2008); Greenhill <i>et al.</i> (2003); Karachentsev <i>et al.</i> (2007)
NGC 4945	$1.4^{+0.7}_{-0.5}$	3.82	Greenhill <i>et al.</i> (1997); Ferrarese & Ford (2005); Karachentsev <i>et al.</i> (2007)
Sculptor (NGC 253)	10^{+10}_{-5}	3.5	Graham <i>et al.</i> (2011); Rodríguez-Rico <i>et al.</i> (2006); Rekola <i>et al.</i> (2005)
NGC 4395	0.36 ± 0.11	4.0	Peterson <i>et al.</i> (2005); Thim <i>et al.</i> (2004)
M96 (NGC 3368)	7.3 ± 1.5	10.1	Graham <i>et al.</i> (2011); Nowak <i>et al.</i> (2010); Tonry <i>et al.</i> (2001)
NGC 3489	5.8 ± 0.8	11.7	Graham <i>et al.</i> (2011); Nowak <i>et al.</i> (2010); Tonry <i>et al.</i> (2001)

Table 4.1 Sample of nearby MBHs that are candidates for producing detectable EMRBs.**Figure 4.1** Scaled SNR for EMRBs as a function of characteristic frequency. The fitted curve from equation (4.6) is indicated by the line.

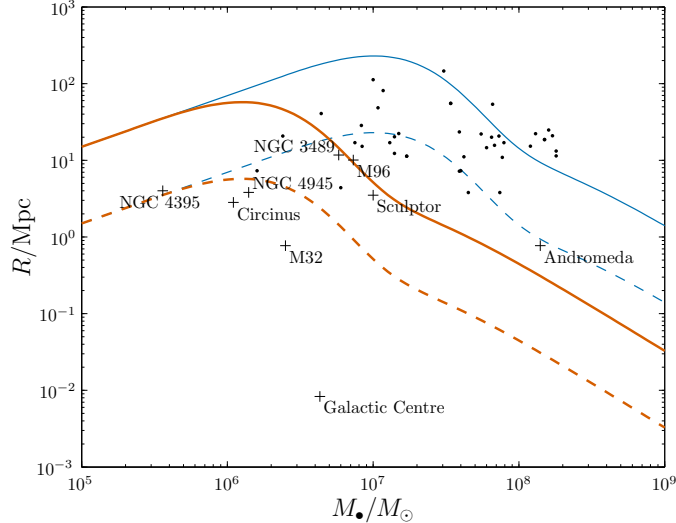


Figure 4.2 Limit of detection using LISA for EMRBs originating from MBHs of mass M and distance R with CO of mass $\mu = 1M_{\odot}$ (dashed line) or $\mu = 10M_{\odot}$ (solid line). The detection threshold is assumed to be $\rho = 10$. The thicker line is the limit for non-rotating MBHs, the thinner is for maximally rotating MBHs. Sources below the relevant line are potentially detectable. The crosses indicate the selected sample of MBHs used to calibrate the curve and the dots indicate other nearby MBHs with known masses. The trends should not be extrapolated to lower MBH masses.

To fit this, we treat the problem as if it were a likelihood maximisation, with each averaged point having a Gaussian likelihood with standard deviation defined from the scatter because of the variation in the ancillary parameters. The optimised values for LISA are

$$\begin{aligned} \alpha_1 &\simeq 8.93 \times 10^4; & \alpha_2 &\simeq 4.68 \times 10^2; & \alpha_3 &\simeq 1.84 \times 10^2; \\ \beta_1 &\simeq 1.84; & \beta_2 &\simeq 3.23; & \beta_3 &\simeq 1.27; & \beta_4 &\simeq 4.13. \end{aligned} \quad (4.7)$$

Using our fitted trends, it is possible to invert equation (4.5) to find the furthest distance that a system contain an MBH of a given mass can produce detectable bursts. In calculating the maximum SNR it is necessary to decide upon a maximum f_* . This corresponds to the minimum periapse radius which is in turn determined by the MBH spin. For the optimal case with a maximally rotating MBH, the innermost periapsis is $r_p = r_g$; for a non-rotating MBH, the innermost periapsis would be $r_p = 4r_g$. We shall use both as limits for the maximum SNR.

Figure 4.2 shows the detectability limit for $\mu = 1M_{\odot}$ and $\mu = 10M_{\odot}$ COs. In addition to the sample of MBHs from table 4.1 we plot additional nearby MBHs (see Graham 2008; Graham *et al.* 2011; Graham & Scott 2013, and references therein). The more massive COs are detectable to a greater distance, but are also the more likely sources since mass segregation ensures that they are more likely to be on orbits that pass close to the MBH (Bahcall & Wolf 1977; Alexander & Hopman 2009; Pretor & Amaro-Seoane 2010). Limits using periapsis of r_g and $4r_g$ are shown: intermediate spin values would

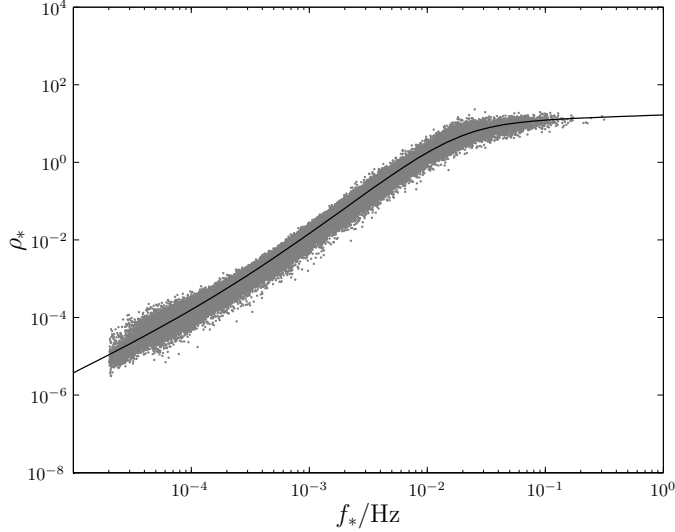


Figure 4.3 Scaled SNR for EMRBs as a function of characteristic frequency for the eLISA design. The fitted curve from equation (4.6) is indicated by the line.

have limits between these two. In any case, these are strict bounds; it is unlikely that we would observe a burst from the optimal orbit. Therefore bursts from MBHs outside the curve are impossible to detect and those inside may be possible, but need not be probable, to detect.

It appears that there are many extragalactic MBHs which could produce observable bursts. From the sample in table 4.1 all could be detected. Andromeda could only be detected if it has a high spin value. It is therefore less promising than the others. NGC 3489, M96 and Sculptor lie on the boundary of detectability for non-spinning sources with a $10M_{\odot}$ CO. They are therefore of marginal interest: we do not necessarily need any special requirement for the spin, but such close orbits would be infrequent. NGC 4395, NGC 4945 and Circinus are around the boundary of detectability for a $1M_{\odot}$ CO. Hence, we could potentially see bursts from white dwarfs or neutron stars as well as BHs. M32 is the best extragalactic source, lying safely within the detection limit for $1M_{\odot}$ COs. Outside of our sample there are other MBHs with measured masses that are of interest. A great many could potentially be detected using optimal bursts from $10M_{\odot}$ COs orbiting a maximally rotating MBH.¹ The most promising MBHs not included in our test sample are found in M64 (NGC 4826), NGC 3076 and M94 (NGC 4736).

We can repeat the analysis for eLISA. The scaled SNRs are shown in figure 4.3. Since Andromeda was only marginally of interest for the classic LISA design, we did not include it this time. This reduces the scatter at low characteristic frequencies.

¹Many galaxies of the Virgo cluster fall in this category. This could potentially make identifying the source galaxy more difficult as the candidates are close together. Since we would have to be fortunate to encounter this problem, we shall not be overly concerned by it.

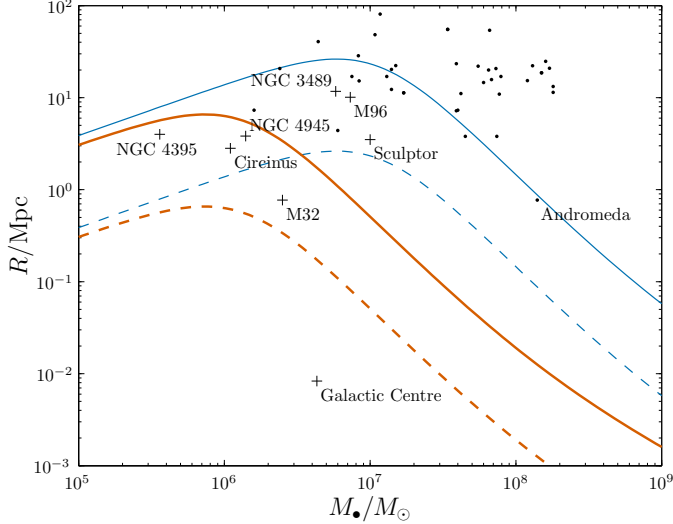


Figure 4.4 Limit of detection using eLISA for EMRBs originating from MBHs of mass M and distance R with CO of mass $\mu = 1M_\odot$ (dashed line) or $\mu = 10M_\odot$ (solid line). The detection threshold is assumed to be $\rho = 10$. The thicker line is the limit for non-rotating MBHs, the thinner is for maximally rotating MBHs. Sources below the relevant line are potentially detectable. The crosses indicate the selected sample of MBHs used to calibrate the curve and the dots indicate other nearby MBHs with known masses. The trends should not be extrapolated to lower MBH masses.

The curve is fitted with

$$\begin{aligned} \alpha_1 &\simeq 73.9; & \alpha_2 &\simeq 4.99 \times 10^3; & \alpha_3 &\simeq 52.7; \\ \beta_1 &\simeq 1.47; & \beta_2 &\simeq 0.85; & \beta_3 &\simeq 1.76; & \beta_4 &\simeq 1.25. \end{aligned} \quad (4.8)$$

The fit parameters are markedly different from those for LISA. However, since we are fitting a phenomenological model and the parameters have no physical significance, we are not concerned with this. The parameters yield a good fit to the data, which is all that we are concerned about here.

Using this fit to find the detectability range results in the curves shown in figure 4.4. The maximum distances are reduced compared to the LISA case indicating that detectable bursts would be much rarer. There still remain a number of potential candidate galaxies. From our sample, Andromeda is on the very edge of possibility. NGC 3489, M96 and Sculptor require a high spin, making them unlikely sources. NGC 4395, NGC 4945 and Circinus can be detected without the high spin assuming a $10M_\odot$ CO. Of the extragalactic sources, only M32 remains detectable with a $1M_\odot$ CO, and still it requires a non-zero spin.

Using either noise curve we see that EMRBs could potentially be seen from a range of galaxies. The Galaxy's MBH remains securely detectable in either case. M32 is the next best. MBHs with masses $\sim 10^6\text{--}10^7 M_\odot$ are observable to the greatest distance. We currently know of few MBHs with masses at the lower end of the spectrum ($10^5\text{--}10^6 M_\odot$)

but these would be good potential candidates.

4.2 Parameter estimation using extragalactic bursts

We are not only interested in discovering if EMRBs are detectable, but also if we can extract information from the signals about their sources. To investigate the potential of extragalactic EMRBs, we considered a sample of bursts from M32, the most promising candidate; NGC N4945, which is near to the optimal mass for LISA (without assuming spin), and NGC 4395, the lightest MBH in our sample. Circinus is similar to NGC 4945, so we expect comparable results: EMRBs from Circinus should be slightly more useful as Circinus is closer.

4.2.1 Parameter inference

In determining parameters from burst waveforms, we have the same inference problem as in section 3.2. Our parameter set, as previously enumerated in section 3.1.1, consists of:

1. The MBH's mass M_\bullet .
2. The spin parameter a_* .
- 3, 4. The orientation angles for the MBH spin Θ_K and Φ_K .
5. The source distance R divided by the CO mass μ , which we denote as $\zeta = R/\mu$.
This scales the amplitude of the waveform.
- 6, 7. The angular momentum of the CO parametrized in terms of total angular momentum L_∞ and inclination ι .
- 8–10. The angular phases at periapse, ϕ_p and χ_p (which determines θ_p), and the time of periapse t_p .
- 11, 12. The coordinates of the source. Sky position is already determined to high accuracy for each galaxy. Since an EMRB can only give weak constraints on source position we take it as known and do not infer it.
- 13, 14. The orbital position of the detector. This should be known and need not be inferred. We assume the same initial position as Cutler (1998); this does not qualitatively influence results.

We are interested in inferring the first 10. The most interesting are the MBH's mass and spin, as these give an insight into the evolution of the MBH's host galaxy. We have estimates for many extragalactic MBHs' masses, but these are less accurate than for the Galactic MBH.

We have assumed that sky position is known; to be able to do this in practice we must be able to successfully identify the source galaxy. We shall see that there are only

a few potential galaxies that could produce detectable EMRBs. It should therefore not be too computationally expensive to check all the candidate sky positions. If multiple galaxies lie close together on the sky, such that they cannot be distinguished, it could be possible to use constraints on the MBH mass to differentiate them. This would not help with galaxies for which we do not have good MBH mass estimates.

4.2.2 Mapping the posterior distribution

To discover if any parameters can be accurately inferred, we must characterise the shape of the posterior. We do this using the MCMC techniques developed in section 3.2.2. The only modification was to lower the target acceptance rate to ~ 0.08 . This appeared to give improved convergence for these less-informative distributions.

As for bursts from the Galactic Centre, posteriors can show strong and complicated parameter degeneracies. The lower SNR compared to Galactic bursts yields wider distributions. As the periapsis increases, the posteriors deteriorate, becoming uninformative. The posteriors recovered from our MCMC show a wide variety of forms. There is a spectrum from well-formed Gaussians through elongated ellipsoids to complete covering of the parameter range. Some example results are shown in figure 4.5, 4.6 and 4.7. These are similar to the plots in section 3.3 except that we now plot $\ln(M_\bullet/M_\odot)$ and $\ln(\zeta/\zeta_0)$.

Figure 4.5 shows the posterior for an EMRB from M32 with $r_p \simeq 5.53r_g$. The distribution is well-defined and near Gaussian, although even in this best case the presence of degeneracies is clear. This example illustrates that it is possible to obtain good results, similar to those from the Galactic Centre, from extragalactic sources. Unfortunately, such tight distributions are not common in our sample.

Figure 4.6 shows the posterior for an EMRB from N4395 with $r_p \simeq 5.92r_g$; it illustrates a more usual posterior. Typical posteriors are not Gaussian; the forms vary significantly, such that it is not possible to produce a standard shape. Non-Gaussianity manifests by the distributions broadening, developing curves and becoming banana-like. The degeneracies may evolve such that there are multiple modes.

Figure 4.7 shows the culmination of the deterioration of the posterior; it is for an EMRB from M32 with $r_p \simeq 11.79r_g$. In this case, the distributions have extended to encompass the entire range for some parameters and so the EMRB is (near) useless. The posteriors show intricate degeneracies in some angular parameters. These are naturally periodic and demonstrate that near identical bursts can be produced through various rotations of the MBH and orbit. Such bursts are not informative and so are not of interest, but we include this example so that there is no illusion of all EMRBs having perfect posteriors.

The general trend is for bursts from orbits with smaller periapses to be narrower and more Gaussian. As the periapse increases, and SNR decreases, the distributions broaden becoming more non-Gaussian. Curving degeneracies and secondary modes develop.

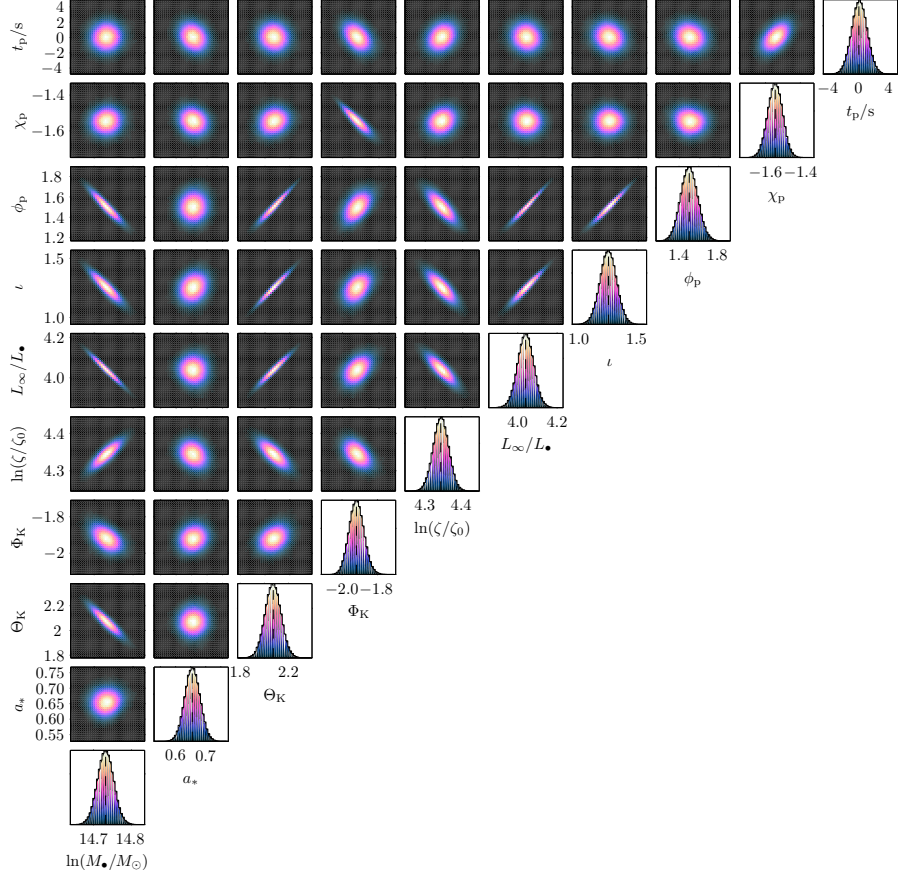


Figure 4.5 Marginalised one- and two-dimensional posteriors (on the diagonal and above, respectively). The scales are identical in both types of plots. The dotted line indicates the true value. These distributions are exceptionally cromulent and well converged. Angular momentum is in units of $L_\bullet = GMc^{-1}$ and the scaled distance is in units of $\zeta_0 = 1M_\odot^{-1}$ kpc. The EMRB is from M32 and has $r_p \simeq 5.53r_g$.

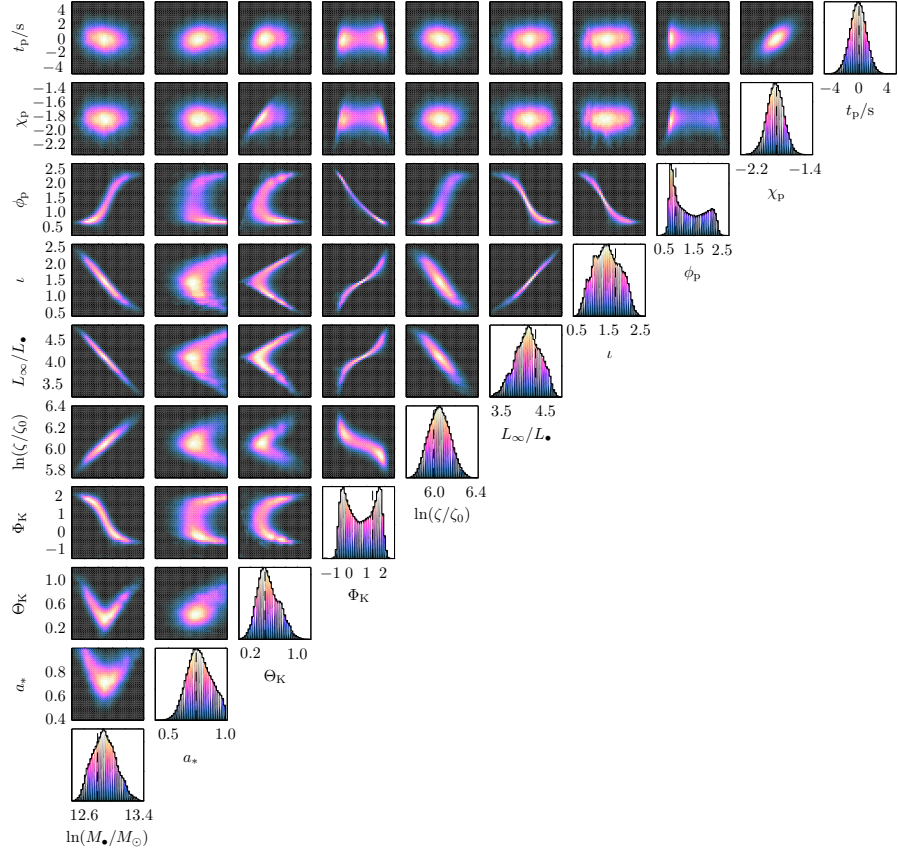


Figure 4.6 Marginalised one- and two-dimensional posteriors. The conventions are the same as in figure 4.5. These distributions begin to show the complicated shapes of degenerate distributions. The EMRB is from NGC 4395 and has $r_p \simeq 5.92r_g$.

Eventually, the distribution broadens to encompass the entire permitted range for the spin and various angular parameters, effectively making these quantities unconstrained.

4.2.3 Parameter uncertainties

Characteristic distribution widths for the (logarithm of the) MBH mass and the spin are shown in figure 4.8, 4.9 and 4.10 for M32, NGC 4945 and NGC 4395 respectively. Plotted are the standard deviation σ_{SD} and the half-width of the $p = 0.68$ range calculated from the k -d tree $\sigma_{0.68}$. These widths are defined in section 3.3.1.1 and are equal for a normal distribution. The filled circles are used for runs that appear to have converged. The open circles are for those yet to converge, but which appear to be approaching an equilibrium state; widths should be accurate to within $\sim 10\%$.

The widths, corresponding to potential parameter accuracies, improve rapidly with decreasing periapsis. The two widths, σ_{SD} and $\sigma_{0.68}$, are typically of similar sizes, despite manifest non-Gaussianity. This is true for all parameters: the greatest differences are when the distributions are strongly multimodal. The fractional difference between the

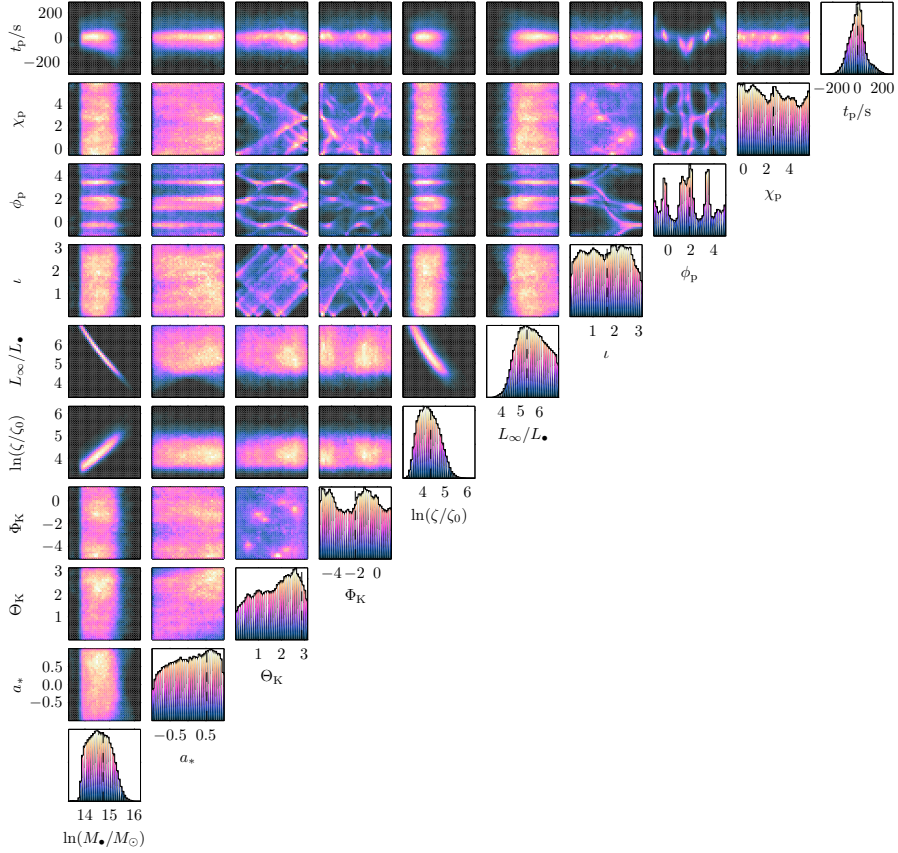


Figure 4.7 Marginalised one- and two-dimensional posteriors. The conventions are the same as in figure 4.5. These are the worst-case scenario distributions that are uninformative. The EMRB is from M32 and has $r_p \simeq 11.79r_g$.

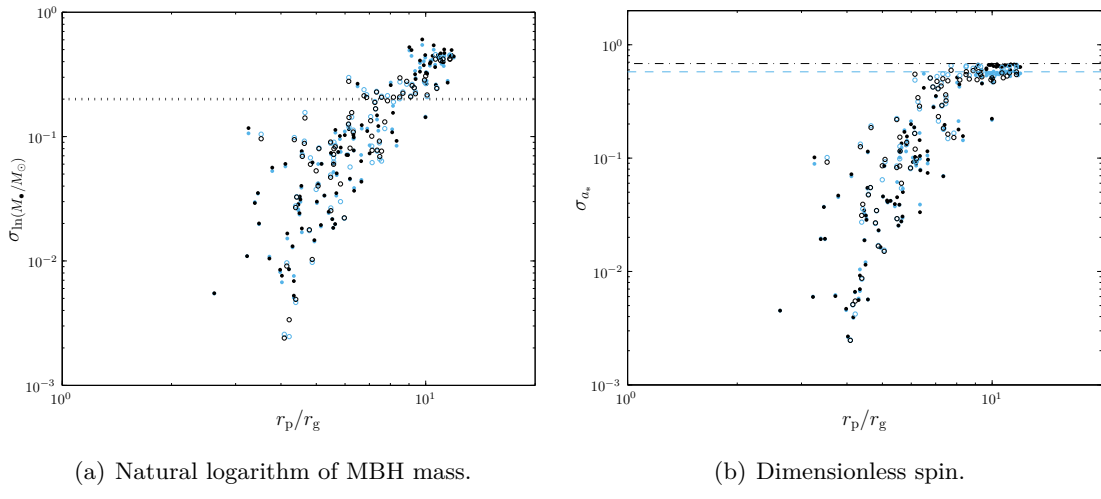


Figure 4.8 Distribution widths as functions of periapsis r_p for M32. The light blue points are used for the standard deviation, the black for the 68-percentile half-width. The filled circles are converged runs and the open circles for those yet to converge. The dotted line is the current uncertainty for M_\bullet . The dashed line is the standard deviation for a uniform a_* distribution and the dot-dashed line is the equivalent 68-percentile half-width.

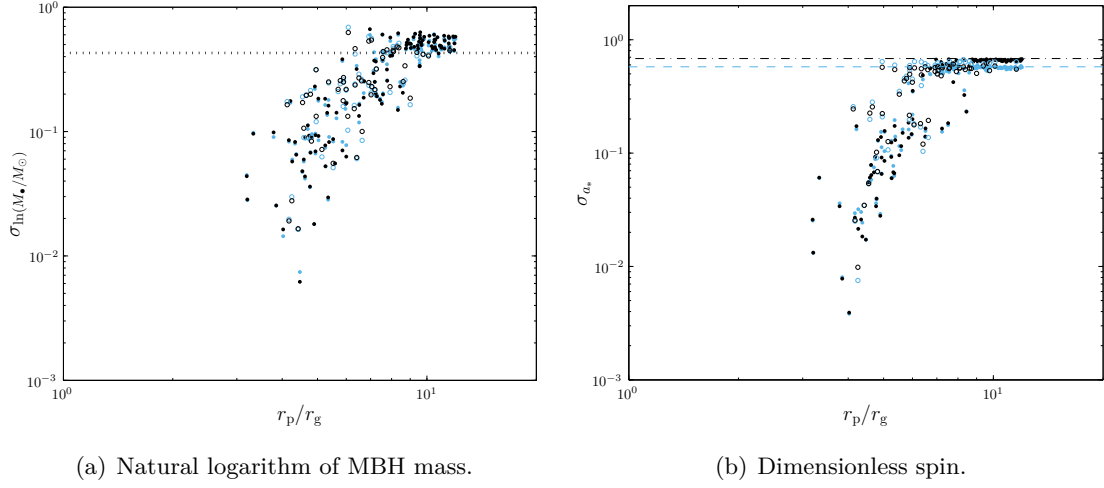


Figure 4.9 Distribution widths as functions of periapsis r_p for NGC 4945. Conventions are identical to those in figure 4.8.

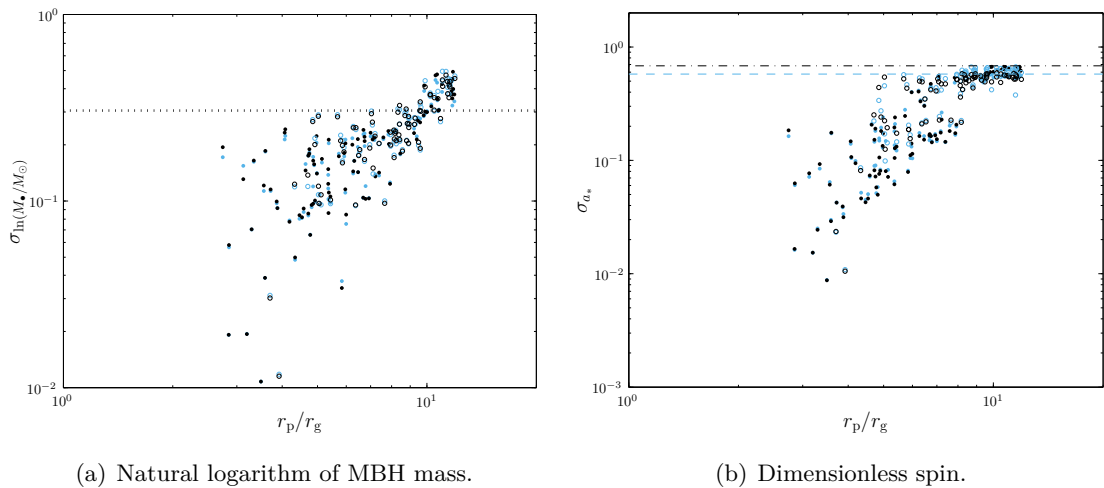


Figure 4.10 Distribution widths as functions of periapsis r_p for NGC 4395. Conventions are identical to those in figure 4.8.

two widths may be up to $\sim 40\%$ for $\ln(M/M_\odot)$ and a_* ; the widths for ϕ_p show the greatest difference, where σ_{SD} may be a factor of a few larger than $\sigma_{0.68}$. Both σ_{SD} and $\sigma_{0.68}$ tend to the appropriate limits for uninformative distributions.

In the best case, uncertainties in mass and spin may be only one part in 10^2 . As might be expected from figure 4.2, M32 has the smallest widths followed by NGC 4945 and then NGC 4395. The spin width saturates about the value expected from a uniform distribution. At this point, we can no longer constrain the spin. The transition does not show any clear correlation with the magnitude of the spin, but is predominantly determined by the periapsis and SNR.

The other parameters show similar behaviour. The angular variables also reach maximum widths, corresponding to uninformative distributions. This does not appear to be directly tied to the spin width.

Potentially, an EMRB could place useful constraints on the mass and spin of an MBH if the periapse radius is small enough.² For M32 we require $r_p \lesssim 8r_g$; for NGC 4945 we require $r_p \lesssim 8r_g$ and $r_p \lesssim 7r_g$ for mass and spin measurements, respectively, and for NGC 4395 we require $r_p \lesssim 9r_g$ and $r_p \lesssim 8r_g$, respectively. Since the range of useful periapses is small, we expect useful EMRBs originating from any individual galaxy to be rare. However, because there are many galaxies hosting potential sources, the probability of seeing any useful EMRBs need not be negligible. Therefore, EMRBs could be a useful astronomical tool.

4.3 Summary and conclusions

We have studied extreme-mass-ratio bursts from extragalactic sources. The SNR of EMRBs has a fundamental scaling with the system parameters. Removing these proportionalities gives a scaled SNR that can be specified as a function of the characteristic frequency f_* . Using these relations allows us to calculate the maximum distance to which EMRBs from a system containing an MBH of a given mass can be detected.

The MBH in our own Galaxy is by far the best source for bursts; however, it is also possible to detect bursts from extragalactic sources. In particular, M32 is a promising candidate. This is good news for any space-borne GW detectors, as EMRBs can be added to their list of potential sources.

Utilising the classic LISA design, EMRBs from a $10M_\odot$ orbiting CO could be detected out to a distance of ~ 100 Mpc. With the descoped eLISA design, this decreases to ~ 10 Mpc. This may drastically reduce the chance of observing an EMRB. For both detectors, sensitivity is maximal for MBHs of $M \sim 10^6\text{--}10^7 M_\odot$, being at slightly higher masses for LISA than for eLISA. We can detect bursts from systems with high MBH

²Here, we assume that a mass measurement is useful if its accuracy is smaller than the current measurement uncertainty, and a spin measurement is useful if it provides any constraint.

spins out to greater distance; hence, the EMRB event rate would be enhanced if MBH spins naturally tend to higher values, perhaps as a consequence of accretion.

However, we must still be cautious: EMRBs may be rare and the event rate may prevent us from observing any over a realistic mission lifetime. Bursts from any given extragalactic source should be less common than from the Galactic Centre, although this may be slightly ameliorated by the larger number of galaxies hosting potential source systems. In the following chapter we shall construct a model to estimate the event rate for Galactic bursts. It is more difficult to perform a similar estimation for other galaxies as we do not have as detailed astrophysical measurement. However, we may use the Galactic event rate as a guide to predict the number of bursts per Milky Way equivalent galaxy.

Extragalactic EMRBs can provide good measurements of MBH mass and spin, but only across an extremely narrow range of periapses. We studied M32, NGC 4945 and NGC 4395 as examples. For all three we found that it is possible to extract information from bursts. The uncertainty may be one part in 10^2 – 10^3 for M32, and slightly worse for NGC 4945 and NGC 4395, at about one part in 10^2 . These are not as good as the constraints from Galactic EMRBs, where the uncertainties could be as small as one part in 10^4 , but would still be of great astrophysical interest. These extragalactic MBHs are much harder to study than the MBH in our own Galaxy and we have not yet been able to measure a spin value even for that MBH. Any measurement of spin would give us a unique glimpse into the formation history of the host galaxy.

These results have been obtained assuming the classic LISA design. The first millihertz space-borne interferometer is likely to have a descoped design such as the proposed eLISA. This concept could be revised in the near future and so we have not used it to produce results. The effect of the reduced sensitivity would be to reduce the SNR and increase the widths of the posterior distributions. We expect the trends in figure 4.8, 4.9 and 4.10 to move upwards and saturate at smaller periapses.

Extreme-mass-ratio bursts could be used to place useful constraints on the mass and spin of a nearby MBH if the periapse radius is small enough. Considering the promising candidates of M32, NGC 4945 and NGC 4395, we find that $r_p \lesssim 8r_g$ typically gives insightful constraints. Such orbits are likely to be rare, but just a single such burst from any of the potential galaxies could give us information that is otherwise inaccessible. This is a tantalising prospect.

Part III

Understanding gravitation

Chapter 5

Gravitational radiation in $f(R)$ -gravity

5.1 Beyond general relativity: $f(R)$ modified gravity

GR is a well tested theory of gravity (Will 2006); however, the majority of the tests that have been carried out to date have been in the weak-field, low-energy regime (Will 1993; Psaltis 2008). It is not unreasonable to suspect there may be higher order corrections that are only discovered in the strong-field regime, where curvature is high or spacetime dynamic.

In this and the following chapter, we shall study a modified theory of gravitation to assess the feasibility of potential corrections to GR. We investigate metric $f(R)$ -gravity, in which the Einstein–Hilbert action is modified by replacing the Ricci scalar R with an arbitrary function $f(R)$. This is one of the simplest extensions to standard GR (Sotiriou & Faraoni 2010; De Felice & Tsujikawa 2010). It has attracted significant interest because the flexibility in defining the function $f(R)$ allows a wide range of cosmological phenomena to be described (Nojiri & Odintsov 2007; Capozziello & Francaviglia 2007). For example, Starobinsky (1980) suggested that a quadratic addition to the field equations could drive exponential expansion of the early Universe (Vilenkin 1985): inflation in modern terminology. In this model $f(R) = R - R^2/(6\Upsilon^2)$; the size of the quadratic correction can be tightly constrained by considering the spectrum of curvature perturbations generated during inflation (Starobinskii 1983, 1985). Using the results of the Wilkinson Microwave Anisotropy Probe (WMAP; Bennett *et al.* 2012; Hinshaw *et al.* 2012), the inverse length-scale can be constrained to $\Upsilon \simeq 3 \times 10^{-6}(50/N)\ell_P^{-1}$, where N is the number of e-folds during inflation and ℓ_P is the Planck length (Starobinsky 2007; De Felice & Tsujikawa 2010).

We consider simple $f(R)$ corrections within the framework of linearised gravity and discover how GWs are modified. We begin by reviewing the properties of the $f(R)$ field equations. We then derive the linearised equations (section 5.3) and use these to deter-

mine the properties of GWs (section 5.4). These are largely known in the literature, but are worked out here *ab initio*. We proceed to derive an effective energy-momentum tensor for gravitational radiation in section 5.5, following the short-wavelength approximation of Isaacson (1968a, b).

Following on from the theory developed in this chapter, in chapter 6 we consider observational tests of $f(R)$ -gravity. We explore what constraints LISA, Solar System tests and laboratory experiments can place on the form of $f(R)$. We do not consider cosmological implications where terms beyond linear order could play a significant role. The overall conclusion is that LISA could place constraints on $f(R)$ -gravity which may be more powerful than those in the Solar System, but are not as powerful as constraints from laboratory experiments. A brief summary of findings from both chapters is found in section 6.4.

Natural units with $c = 1$ are used throughout both chapters, but factors of G are retained.

5.2 Description of $f(R)$ -gravity

5.2.1 The action and field equations

General relativity can be derived from the Einstein–Hilbert action (Misner *et al.* 1973, chapter 21; Landau & Lifshitz 1975, section 93; Dirac 1996, section 26)

$$S_{\text{EH}}[g] = \frac{1}{16\pi G} \int R \sqrt{-g} d^4x. \quad (5.1)$$

In $f(R)$ theory we make a simple modification of the action to include an arbitrary function of the Ricci scalar R such that (Buchdahl 1970)

$$S_{f(R)}[g] = \frac{1}{16\pi G} \int f(R) \sqrt{-g} d^4x. \quad (5.2)$$

Including the function $f(R)$ gives extra freedom in defining the behaviour of gravity. While this action may not encode the true theory of gravity it could contain sufficient information to act as an effective field theory, correctly describing phenomenological behaviour (Park *et al.* 2010); it may be that as an effective field theory, a particular $f(R)$ shall have a limited region of applicability and shall not be universal. We assume that $f(R)$ is analytic about $R = 0$ so that it can be expressed as a power series (Buchdahl 1970; Capozziello *et al.* 2007; Faulkner *et al.* 2007; Clifton 2008; Psaltis *et al.* 2008)

$$f(R) = a_0 + a_1 R + \frac{a_2}{2!} R^2 + \frac{a_3}{3!} R^3 + \dots \quad (5.3)$$

Since the dimensions of $f(R)$ must be the same as of R , $[a_n] = [R]^{(1-n)}$. To link to GR we set $a_1 = 1$; any rescaling can be absorbed into the definition of G .

Various models of cosmological interest may be expressed in such a form, for example, the model of Starobinsky (2007)

$$f(R) = R + \lambda R_0 \left[\left(1 + \frac{R^2}{R_0^2} \right)^{-n} - 1 \right], \quad (5.4)$$

can be expanded as

$$f(R) = R - \frac{\lambda n}{R_0} R^2 + \frac{\lambda n(n+1)}{2R_0^3} R^4 + \dots \quad (5.5)$$

and the model of Hu & Sawicki (2007)

$$f(R) = R - m^2 \frac{c_1 (R/m^2)^n}{c_2 (R/m^2)^n + 1}, \quad (5.6)$$

assuming that $c_2(R/m^2)^n \ll 1$, can be expanded as

$$f(R) = (1 - c_1)R + \frac{c_1 c_2}{m^2} R^2 - \frac{c_1 c_2^2}{m^4} R^3 + \frac{c_1 c_2^3}{m^6} R^4 + \dots \quad (5.7)$$

for $n = 1$ and as

$$f(R) = R - \frac{c_1}{m^2} R^2 + \frac{c_1 c_2^2}{m^4} R^4 + \dots \quad (5.8)$$

for $n = 2$. Consequently such a series expansion can constrain model parameters, although we cannot specify the full functional form from only a few terms.

The field equations are obtained by a variational principle; there are several ways of achieving this. To derive the Einstein field equations from the Einstein–Hilbert action one may use the standard metric variation or the Palatini variation (Misner *et al.* 1973, section 21.2). Both approaches can be used for $f(R)$, but they yield different results (Sotiriou & Faraoni 2010; De Felice & Tsujikawa 2010). Following the metric formalism, one varies the action with respect to the metric $g^{\mu\nu}$. Following the Palatini formalism one varies the action with respect to both the metric $g^{\mu\nu}$ and the connection $\Gamma^\rho_{\mu\nu}$, which are treated as independent quantities: the connection is not the Levi-Civita metric connection.¹

Finally, there is a third version of $f(R)$ -gravity: metric-affine $f(R)$ -gravity (Sotiriou & Liberati 2007a, b). This goes beyond the Palatini formalism by supposing that the matter action is dependent on the variational independent connection. Parallel transport and the covariant derivative are divorced from the metric. This theory has its attractions: it allows for a natural introduction of torsion. However, it is not a metric theory of gravity and so cannot satisfy all the postulates of the Einstein equivalence principle (Will 2006): a free particle does not necessarily follow a geodesic and so the effects of gravity might not

¹Imposing the condition that the metric and Palatini formalisms produce the same field equations, assuming an action that only depends on the metric and Riemann tensor, results in Lovelock gravity (Exirifard & Sheik-Jabbari 2008). Lovelock gravities require the field equations to be divergence free and no more than second order; in four dimensions the only possible Lovelock gravity is GR with a potentially non-zero cosmological constant (Lovelock 1970, 1971, 1972).

be locally removed (Exirifard & Sheik-Jabbari 2008). The implications of this have not been fully explored, but for this reason we will not consider the theory further.

We restrict our attention to metric $f(R)$ -gravity. This is preferred as the Palatini formalism has undesirable properties: static spherically symmetric objects described by a polytropic equation of state are subject to a curvature singularity (Barausse *et al.* 2008b, a; De Felice & Tsujikawa 2010). Varying the action with respect to the metric $g^{\mu\nu}$ produces

$$\delta S_{f(R)} = \frac{1}{16\pi G} \int \left\{ f'(R) \sqrt{-g} [R_{\mu\nu} - \nabla_\mu \nabla_\nu + g_{\mu\nu} \square] - f(R) \frac{1}{2} \sqrt{-g} g_{\mu\nu} \right\} \delta g^{\mu\nu} d^4x, \quad (5.9)$$

where $\square = g^{\mu\nu} \nabla_\mu \nabla_\nu$ is the d'Alembertian and a prime denotes differentiation with respect to R .

Proceeding from here requires certain assumptions regarding surface terms. In the case of the Einstein–Hilbert action these gather into a total derivative; it is possible to subtract this from the action to obtain a well-defined variational quantity (York 1972; Gibbons & Hawking 1977). This is not the case for general $f(R)$ -gravity (Madsen & Barrow 1989). However, since the action includes higher-order derivatives of the metric, we are at liberty to fix more degrees of freedom at the boundary, in so doing eliminating the importance of the surface terms (Dyer & Hinterbichler 2009; Sotiriou & Faraoni 2010). Setting the variation $\delta R = 0$ on the boundary allows us to subtract a term similar to that in GR (Guarnizo *et al.* 2010). We then have a well-defined variational quantity, from which we can obtain the field equations.

The vacuum field equations are

$$f' R_{\mu\nu} - \nabla_\mu \nabla_\nu f' + g_{\mu\nu} \square f' - \frac{f}{2} g_{\mu\nu} = 0. \quad (5.10)$$

Taking the trace gives

$$f' R + 3 \square f' - 2f = 0. \quad (5.11)$$

If we consider a uniform flat spacetime $R = 0$, this requires (Capozziello *et al.* 2007)

$$a_0 = 0. \quad (5.12)$$

In analogy to the Einstein tensor, we define

$$\mathcal{G}_{\mu\nu} = f' R_{\mu\nu} - \nabla_\mu \nabla_\nu f' + g_{\mu\nu} \square f' - \frac{f}{2} g_{\mu\nu}, \quad (5.13)$$

so that in a vacuum

$$\mathcal{G}_{\mu\nu} = 0. \quad (5.14)$$

5.2.2 Conservation of energy-momentum

If we introduce matter with a stress-energy tensor $T_{\mu\nu}$, the field equations become

$$\mathcal{G}_{\mu\nu} = 8\pi G T_{\mu\nu}. \quad (5.15)$$

Acting upon this with the covariant derivative

$$\begin{aligned} 8\pi G \nabla^\mu T_{\mu\nu} &= \nabla^\mu \mathcal{G}_{\mu\nu} \\ &= R_{\mu\nu} \nabla^\mu f' + f' \nabla^\mu \left(R_{\mu\nu} - \frac{1}{2} R g_{\mu\nu} \right) - (\square \nabla_\nu - \nabla_\nu \square) f'. \end{aligned} \quad (5.16)$$

The second term contains the covariant derivative of the Einstein tensor and so is zero.

The final term can be shown to be

$$(\square \nabla_\nu - \nabla_\nu \square) f' = R_{\mu\nu} \nabla^\mu f', \quad (5.17)$$

which is a useful geometric identity (Koivisto 2006). Using this

$$8\pi G \nabla^\mu T_{\mu\nu} = 0. \quad (5.18)$$

Consequently energy-momentum is a conserved quantity in the same way as in GR, as is expected from the symmetries of the action.

5.3 Linearised theory

We start our investigation of $f(R)$ by looking at linearised theory. This is a weak-field approximation that assumes only small deviations from a flat background, greatly simplifying the field equations. Just as in GR, the linearised framework provides a natural way to study GWs. We shall see that the linearised field equations reduce down to flat-space wave equations: GWs are as much a part of $f(R)$ -gravity as of GR.

Consider a perturbation of the metric from flat Minkowski space such that

$$g_{\mu\nu} = \eta_{\mu\nu} + h_{\mu\nu}; \quad (5.19)$$

where, more formally, $h_{\mu\nu} = \varepsilon H_{\mu\nu}$ for a small parameter ε .² We only consider terms to $\mathcal{O}(\varepsilon)$. The inverse metric is then

$$g^{\mu\nu} = \eta^{\mu\nu} - h^{\mu\nu}, \quad (5.20)$$

where we have used the Minkowski metric to raise the indices on the right, defining

$$h^{\mu\nu} = \eta^{\mu\sigma} \eta^{\nu\rho} h_{\sigma\rho}. \quad (5.21)$$

²It is because we wish to perturb about flat spacetime that we have required $f(R)$ to be analytic about $R = 0$.

Similarly, the trace h is given by

$$h = \eta^{\mu\nu} h_{\mu\nu}. \quad (5.22)$$

All quantities denoted by “ h ” are strictly $\mathcal{O}(\varepsilon)$.

The linearised connection is

$$\Gamma^{(1)\rho}_{\mu\nu} = \frac{1}{2} \eta^{\rho\lambda} (\partial_\mu h_{\lambda\nu} + \partial_\nu h_{\lambda\mu} - \partial_\lambda h_{\mu\nu}). \quad (5.23)$$

To $\mathcal{O}(\varepsilon)$ the covariant derivative of any perturbed quantity is the same as the partial derivative. The Riemann tensor is

$$R^{(1)\lambda}_{\mu\nu\rho} = \frac{1}{2} (\partial_\mu \partial_\nu h^\lambda_\rho + \partial^\lambda \partial_\rho h_{\mu\nu} - \partial_\mu \partial_\rho h^\lambda_\nu - \partial^\lambda \partial_\nu h_{\mu\rho}), \quad (5.24)$$

where we have raised the index on the differential operator with the background Minkowski metric. Contracting gives the Ricci tensor

$$R^{(1)}_{\mu\nu} = \frac{1}{2} (\partial_\mu \partial_\rho h^\rho_\nu + \partial_\nu \partial_\rho h^\rho_\mu - \partial_\mu \partial_\nu h - \square h_{\mu\nu}), \quad (5.25)$$

where the d'Alembertian operator is $\square = \eta^{\mu\nu} \partial_\mu \partial_\nu$. Contracting this with $\eta^{\mu\nu}$ gives the first-order Ricci scalar

$$R^{(1)} = \partial_\mu \partial_\rho h^{\rho\mu} - \square h. \quad (5.26)$$

To $\mathcal{O}(\varepsilon)$ we can write $f(R)$ as a Maclaurin series

$$f(R) = a_0 + R^{(1)}; \quad (5.27a)$$

$$f'(R) = 1 + a_2 R^{(1)}. \quad (5.27b)$$

As we are perturbing from a Minkowski background where the Ricci scalar vanishes, we use equation (5.12) to set $a_0 = 0$. Inserting these into equation (5.13) and retaining terms to $\mathcal{O}(\varepsilon)$ yields

$$\mathcal{G}^{(1)}_{\mu\nu} = R^{(1)}_{\mu\nu} - \partial_\mu \partial_\nu (a_2 R^{(1)}) + \eta_{\mu\nu} \square (a_2 R^{(1)}) - \frac{R^{(1)}}{2} \eta_{\mu\nu}. \quad (5.28)$$

Now consider the linearised trace equation, from equation (5.11)

$$\begin{aligned} \mathcal{G}^{(1)} &= R^{(1)} + 3 \square (a_2 R^{(1)}) - 2 R^{(1)} \\ &= 3 \square (a_2 R^{(1)}) - R^{(1)}, \end{aligned} \quad (5.29)$$

where $\mathcal{G}^{(1)} = \eta^{\mu\nu} \mathcal{G}^{(1)}_{\mu\nu}$. This is the massive inhomogeneous Klein-Gordon equation. Setting $\mathcal{G} = 0$, as for a vacuum, we obtain the standard Klein-Gordon equation

$$\square R^{(1)} + \Upsilon^2 R^{(1)} = 0, \quad (5.30)$$

defining the reciprocal length (squared)

$$\Upsilon^2 = -\frac{1}{3a_2}. \quad (5.31)$$

For a physically meaningful solution $\Upsilon^2 > 0$: we constrain $f(R)$ such that $a_2 < 0$ (Schmidt 1986; Teyssandier 1990; Olmo 2005; Corda 2008). From Υ we define a reduced Compton wavelength

$$\lambda_R = \frac{1}{\Upsilon} \quad (5.32)$$

associated with this scalar mode.

The next step is to substitute in $h_{\mu\nu}$ to find wave solutions. We want a quantity $\bar{h}_{\mu\nu}$ that satisfies a wave equation, related to $h_{\mu\nu}$ by

$$\bar{h}_{\mu\nu} = h_{\mu\nu} + A_{\mu\nu}. \quad (5.33)$$

In GR we use the trace-reversed form where $A_{\mu\nu} = -(h/2)\eta_{\mu\nu}$. This does not suffice here, but let us look for a similar solution

$$\bar{h}_{\mu\nu} = h_{\mu\nu} - \frac{h}{2}\eta_{\mu\nu} + B_{\mu\nu}. \quad (5.34)$$

The only rank-two tensors in our theory are: $h_{\mu\nu}$, $\eta_{\mu\nu}$, $R^{(1)}_{\mu\nu}$, and $\partial_\mu\partial_\nu$; $h_{\mu\nu}$ has been used already, and we wish to eliminate $R^{(1)}_{\mu\nu}$, so we can try the simpler option based around $\eta_{\mu\nu}$. We want $B_{\mu\nu}$ to be $\mathcal{O}(\varepsilon)$; since we have already used h , we shall try the other scalar quantity $R^{(1)}$. Therefore, we construct an ansatz

$$\bar{h}_{\mu\nu} = h_{\mu\nu} + \left(ba_2 R^{(1)} - \frac{h}{2} \right) \eta_{\mu\nu}, \quad (5.35)$$

where a_2 has been included to ensure dimensional consistency and b is a dimensionless number. Contracting with the background metric yields

$$\bar{h} = 4ba_2 R^{(1)} - h, \quad (5.36)$$

so we can eliminate h in our definition of $\bar{h}_{\mu\nu}$ to give

$$h_{\mu\nu} = \bar{h}_{\mu\nu} + \left(ba_2 R^{(1)} - \frac{\bar{h}}{2} \right) \eta_{\mu\nu}. \quad (5.37)$$

Just as in GR, we have the freedom to perform a gauge transformation (Misner *et al.* 1973, box 18.2; Hobson *et al.* 2006, section 17.1): the field equations are gauge-invariant since we started with a function of the gauge-invariant Ricci scalar. We shall assume a Lorenz, or de Donder, gauge choice

$$\nabla^\mu \bar{h}_{\mu\nu} = 0; \quad (5.38)$$

or for a flat spacetime

$$\partial^\mu \bar{h}_{\mu\nu} = 0. \quad (5.39)$$

Subject to this, from equation (5.25), the Ricci tensor is

$$R^{(1)}_{\mu\nu} = - \left[b\partial_\mu\partial_\nu(a_2 R^{(1)}) + \frac{1}{2}\square \left(\bar{h}_{\mu\nu} - \frac{\bar{h}}{2}\eta_{\mu\nu} \right) + \frac{b}{6}(R^{(1)} + G^{(1)})\eta_{\mu\nu} \right]. \quad (5.40)$$

Using this with equation (5.29) in equation (5.28) gives

$$\mathcal{G}^{(1)}_{\mu\nu} = \frac{2-b}{6}\mathcal{G}^{(1)}\eta_{\mu\nu} - \frac{1}{2}\square\left(\bar{h}_{\mu\nu} - \frac{\bar{h}}{2}\eta_{\mu\nu}\right) - (b+1)\left[\partial_\mu\partial_\nu(a_2R^{(1)}) + \frac{1}{6}R^{(1)}\eta_{\mu\nu}\right]. \quad (5.41)$$

Picking $b = -1$ the final term vanishes, thus we set (Will 1993, section 10.3; Corda 2008; Capozziello *et al.* 2008)

$$\bar{h}_{\mu\nu} = h_{\mu\nu} - \left(a_2R^{(1)} + \frac{h}{2}\right)\eta_{\mu\nu} \quad (5.42a)$$

$$h_{\mu\nu} = \bar{h}_{\mu\nu} - \left(a_2R^{(1)} + \frac{\bar{h}}{2}\right)\eta_{\mu\nu}. \quad (5.42b)$$

From equation (5.26) the Ricci scalar is

$$\begin{aligned} R^{(1)} &= \square\left(a_2R^{(1)} - \frac{\bar{h}}{2}\right) + \square(4a_2R^{(1)} + \bar{h}) \\ &= 3\square(a_2R^{(1)}) + \frac{1}{2}\square\bar{h}. \end{aligned} \quad (5.43)$$

For consistency with equation (5.29), we require

$$-\frac{1}{2}\square\bar{h} = \mathcal{G}^{(1)}. \quad (5.44)$$

Inserting this into equation (5.41), with $b = -1$, we see

$$-\frac{1}{2}\square\bar{h}_{\mu\nu} = \mathcal{G}^{(1)}_{\mu\nu}; \quad (5.45)$$

we have our wave equations.

Should a_2 be sufficiently small that it can be regarded an $\mathcal{O}(\varepsilon)$ quantity, we recover the usual GR formulae to leading order within our analysis.

5.4 Gravitational radiation

Having established two wave equations, (5.29) and (5.45), we now investigate their solutions. Consider waves in a vacuum, such that $\mathcal{G}_{\mu\nu} = 0$. Using a standard Fourier decomposition

$$\bar{h}_{\mu\nu} = \hat{h}_{\mu\nu}(k_\rho) \exp(ik_\rho x^\rho), \quad (5.46a)$$

$$R^{(1)} = \hat{R}(q_\rho) \exp(iq_\rho x^\rho), \quad (5.46b)$$

where k_μ and q_μ are four-wavevectors. From equation (5.45) we know that k_μ is a null vector, so for a wave travelling along the z -axis

$$k^\mu = \omega(1, 0, 0, 1), \quad (5.47)$$

where ω is the angular frequency. Similarly, from equation (5.29)

$$q^\mu = (\Omega, 0, 0, \sqrt{\Omega^2 - \Upsilon^2}), \quad (5.48)$$

for frequency Ω . These waves do not travel at c , but have a group velocity

$$v(\Omega) = \frac{\sqrt{\Omega^2 - \Upsilon^2}}{\Omega}, \quad (5.49)$$

provided that $\Upsilon^2 > 0$, $v < 1 = c$. For $\Omega < \Upsilon$, we find an evanescently decaying wave. The travelling wave is dispersive; for waves made up of a range of frequency components there shall be a time delay between the arrival of the high-frequency and low-frequency constituents. This may make it difficult to reconstruct a waveform, should the scalar mode be observed with a GW detector (Corda 2009a).

From the gauge condition equation (5.39) we find that k^μ is orthogonal to $\hat{h}_{\mu\nu}$,

$$k^\mu \hat{h}_{\mu\nu} = 0, \quad (5.50)$$

in this case

$$\hat{h}_{0\nu} + \hat{h}_{3\nu} = 0. \quad (5.51)$$

Let us consider the implications of equation (5.44) using (5.29) and (5.36),

$$\begin{aligned} \square (4a_2 R^{(1)} + h) &= 0 \\ \square h &= -\frac{4}{3} R^{(1)}. \end{aligned} \quad (5.52)$$

For non-zero $R^{(1)}$ (as required for the Ricci mode) there is no way to make a gauge choice such that the trace h vanishes (Corda 2008; Capozziello *et al.* 2008). This is distinct from in GR. It is possible, however, to make a gauge choice such that the trace \bar{h} vanishes. Consider a gauge transformation generated by ξ_μ which satisfies $\square \xi_\mu = 0$, and so has a Fourier decomposition

$$\xi_\mu = \hat{\xi}_\mu \exp(ik_\rho x^\rho). \quad (5.53)$$

A transformation

$$\bar{h}_{\mu\nu} \rightarrow \bar{h}_{\mu\nu} + \partial_\mu \xi_\nu + \partial_\nu \xi_\mu - \eta_{\mu\nu} \partial^\rho \xi_\rho, \quad (5.54)$$

would ensure both conditions (5.39) and (5.45) are satisfied (Misner *et al.* 1973, section 35.2). Under such a transformation

$$\hat{h}_{\mu\nu} \rightarrow \hat{h}_{\mu\nu} + i \left(k_\mu \hat{\xi}_\nu + k_\nu \hat{\xi}_\mu - \eta_{\mu\nu} k^\rho \hat{\xi}_\rho \right). \quad (5.55)$$

We may impose four further constraints (one for each $\hat{\xi}_\mu$) upon $\hat{h}_{\mu\nu}$. We take these to be (Wald 1984, section 4.4)

$$\hat{h}_{0\nu} = 0, \quad \hat{h} = 0. \quad (5.56)$$

This might appear to be five constraints, but we have already imposed equation (5.51), and so setting $\hat{h}_{00} = 0$ automatically implies $\hat{h}_{03} = 0$. In this gauge

$$h_{\mu\nu} = \bar{h}_{\mu\nu} - a_2 R^{(1)} \eta_{\mu\nu}; \quad h = -4a_2 R^{(1)}. \quad (5.57)$$

Thus $\bar{h}_{\mu\nu}$ behaves just as its GR counterpart; we can define

$$[\hat{h}_{\mu\nu}] = \begin{bmatrix} 0 & 0 & 0 & 0 \\ 0 & h_+ & h_\times & 0 \\ 0 & h_\times & -h_+ & 0 \\ 0 & 0 & 0 & 0 \end{bmatrix}, \quad (5.58)$$

where h_+ and h_\times are constants representing the amplitudes of the two transverse polarizations of gravitational radiation.

It is important that our solutions reduce to those of GR if $f(R) = R$. In our linearised approach this corresponds to $a_2 \rightarrow 0$, $\Upsilon^2 \rightarrow \infty$. We see from equation (5.48) that in this limit it would take an infinite frequency to excite a propagating Ricci mode, and evanescent waves would decay away infinitely fast. Therefore, there would be no detectable Ricci modes and we would only observe the two polarizations found in GR. Additionally, $\bar{h}_{\mu\nu}$ would simplify to its usual trace-reversed form.

5.5 Energy-momentum tensor

We expect gravitational radiation to carry energy-momentum. Unfortunately, it is difficult to define a proper energy-momentum tensor for a gravitational field: as a consequence of the equivalence principle it is possible to transform to a freely falling frame, eliminating the gravitational field and any associated energy density at a given point, although we can still define curvature in the neighbourhood of this point (Misner *et al.* 1973, section 20.4; Hobson *et al.* 2006, section 17.11). We do nothing revolutionary, but follow the approach of Isaacson (1968a, b). The full field equations (5.10) have no energy-momentum tensor for the gravitational field on the right-hand side; however, by expanding beyond the linear terms we can find a suitable effective energy-momentum tensor for GWs. Expanding $\mathcal{G}_{\mu\nu}$ in orders of $h_{\mu\nu}$

$$\mathcal{G}_{\mu\nu} = \mathcal{G}^{(B)}_{\mu\nu} + \mathcal{G}^{(1)}_{\mu\nu} + \mathcal{G}^{(2)}_{\mu\nu} + \dots \quad (5.59)$$

We use (B) for the background term instead of (0) to avoid confusion regarding its order in ε . So far we have assumed that our background is flat; however, we can imagine that should the gravitational radiation carry energy-momentum then this would act as a source of curvature for the background (Wald 1984, section 4.4b). This is a second-order effect that may be encoded, to accuracy of $\mathcal{O}(\varepsilon^2)$, as (Rindler 2006, section 15.4)

$$\mathcal{G}^{(B)}_{\mu\nu} = -\mathcal{G}^{(2)}_{\mu\nu}. \quad (5.60)$$

By shifting $\mathcal{G}^{(2)}_{\mu\nu}$ to the right-hand side we create an effective energy-momentum tensor. As in GR we average over several wavelengths, assuming that the background curvature is on a larger scale (Misner *et al.* 1973, section 35.13; Stein & Yunes 2011),

$$\mathcal{G}^{(B)}_{\mu\nu} = - \left\langle \mathcal{G}^{(2)}_{\mu\nu} \right\rangle. \quad (5.61)$$

By averaging we probe the curvature in a macroscopic region about a given point in spacetime, yielding a gauge-invariant measure of the gravitational field strength. The averaging can be thought of as smoothing out the rapidly varying ripples of the radiation, leaving only the coarse-grained component that acts as a source for the background curvature.³ The effective energy-momentum tensor for the radiation is

$$t_{\mu\nu} = -\frac{1}{8\pi G} \left\langle \mathcal{G}^{(2)}_{\mu\nu} \right\rangle. \quad (5.62)$$

Having made this provisional identification, we must set about carefully evaluating the various terms in equation (5.59). We begin as in section 5.3 by defining a total metric

$$g_{\mu\nu} = \gamma_{\mu\nu} + h_{\mu\nu}, \quad (5.63)$$

where $\gamma_{\mu\nu}$ is the background metric. This changes our definition for $h_{\mu\nu}$: instead of being the total perturbation from flat Minkowski, it is the dynamical part of the metric with which we associate radiative effects. Since we know that $\mathcal{G}^{(B)}_{\mu\nu}$ is $\mathcal{O}(\varepsilon^2)$, we decompose our background metric as

$$\gamma_{\mu\nu} = \eta_{\mu\nu} + j_{\mu\nu}, \quad (5.64)$$

where $j_{\mu\nu}$ is $\mathcal{O}(\varepsilon^2)$ to ensure that $R^{(B)\lambda}_{\mu\nu\rho}$ is also $\mathcal{O}(\varepsilon^2)$. Therefore its introduction makes no difference to the linearised theory.

We consider terms only to $\mathcal{O}(\varepsilon^2)$. We identify $\Gamma^{(1)\rho}_{\mu\nu}$ from equation (5.23).⁴ We do not distinguish between ∂_μ and $\nabla^{(B)}_\mu$, the covariant derivative for the background metric: to the order of accuracy required covariant derivatives commute and $\nabla^{(B)}_\mu$ behaves just like ∂_μ . Thus

$$\begin{aligned} \Gamma^{(1)\rho}_{\mu\nu} = & \frac{1}{2} \gamma^{\rho\lambda} \left[\partial_\mu \left(\bar{h}_{\lambda\nu} - a_2 R^{(1)} \gamma_{\lambda\nu} \right) + \partial_\nu \left(\bar{h}_{\lambda\mu} - a_2 R^{(1)} \gamma_{\lambda\mu} \right) \right. \\ & \left. - \partial_\lambda \left(\bar{h}_{\mu\nu} - a_2 R^{(1)} \gamma_{\mu\nu} \right) \right], \end{aligned} \quad (5.65)$$

and

$$\begin{aligned} \Gamma^{(2)\rho}_{\mu\nu} = & -\frac{1}{2} h^{\rho\lambda} (\partial_\mu h_{\lambda\nu} + \partial_\nu h_{\lambda\mu} - \partial_\lambda h_{\mu\nu}) \\ = & -\frac{1}{2} \left(\bar{h}^{\rho\lambda} - a_2 R^{(1)} \gamma^{\rho\lambda} \right) \left[\partial_\mu \left(\bar{h}_{\lambda\nu} - a_2 R^{(1)} \gamma_{\lambda\nu} \right) + \partial_\nu \left(\bar{h}_{\lambda\mu} - a_2 R^{(1)} \gamma_{\lambda\mu} \right) \right. \\ & \left. - \partial_\lambda \left(\bar{h}_{\mu\nu} - a_2 R^{(1)} \gamma_{\mu\nu} \right) \right]. \end{aligned} \quad (5.66)$$

³By averaging we do not try to localise the energy of a wave to within a wavelength; for the massive Ricci scalar mode we always consider scales greater than λ_R .

⁴There is one small subtlety: whether we use the background metric $\gamma^{\mu\nu}$ or $\eta^{\mu\nu}$ to raise indices of ∂_μ and $h_{\mu\nu}$. Fortunately, to the accuracy considered here, it does not make a difference, but we shall consider the indices to be changed with $\gamma^{\mu\nu}$.

For the Ricci tensor we can use our linearised expression, equation (5.40), for the first-order term

$$R^{(1)}_{\mu\nu} = a_2 \partial_\mu \partial_\nu R^{(1)} + \frac{1}{6} R^{(1)} \gamma_{\mu\nu}. \quad (5.67)$$

The next term is

$$\begin{aligned} R^{(2)}_{\mu\nu} &= \partial_\rho \Gamma^{(2)\rho}_{\mu\nu} - \partial_\nu \Gamma^{(2)\rho}_{\mu\rho} + \Gamma^{(1)\rho}_{\mu\nu} \Gamma^{(1)\sigma}_{\rho\sigma} - \Gamma^{(1)\rho}_{\mu\sigma} \Gamma^{(1)\sigma}_{\rho\nu} \\ &= \frac{1}{2} \left\{ \frac{1}{2} \partial_\mu \bar{h}_{\sigma\rho} \partial_\nu \bar{h}^{\sigma\rho} + \bar{h}^{\sigma\rho} \left[\partial_\mu \partial_\nu \bar{h}_{\sigma\rho} + \partial_\sigma \partial_\rho (\bar{h}_{\mu\nu} - a_2 R^{(1)} \gamma_{\mu\nu}) \right] \right. \\ &\quad - \partial_\nu \partial_\rho (\bar{h}_{\sigma\mu} - a_2 R^{(1)} \gamma_{\sigma\mu}) - \partial_\mu \partial_\rho (\bar{h}_{\sigma\nu} - a_2 R^{(1)} \gamma_{\sigma\nu}) \Big] \\ &\quad + \partial^\rho \bar{h}_\nu^\sigma (\partial_\rho \bar{h}_{\sigma\mu} - \partial_\sigma \bar{h}_{\rho\mu}) - a_2 \partial^\sigma R^{(1)} \partial_\sigma \bar{h}_{\mu\nu} \\ &\quad \left. + a_2^2 \left(2 R^{(1)} \partial_\mu \partial_\nu R^{(1)} + 3 \partial_\mu R^{(1)} \partial_\nu R^{(1)} + R^{(1)} \square^{(B)} R^{(1)} \gamma_{\mu\nu} \right) \right\}. \end{aligned} \quad (5.68)$$

The d'Alembertian is $\square^{(B)} = \gamma^{\mu\nu} \partial_\mu \partial_\nu$.

To find the Ricci scalar we contract the Ricci tensor with the full metric. To $\mathcal{O}(\varepsilon^2)$,

$$R^{(B)} = \gamma^{\mu\nu} R^{(B)}_{\mu\nu} \quad (5.69a)$$

$$R^{(1)} = \gamma^{\mu\nu} R^{(1)}_{\mu\nu} \quad (5.69b)$$

$$\begin{aligned} R^{(2)} &= \gamma^{\mu\nu} R^{(2)}_{\mu\nu} - h^{\mu\nu} R^{(1)}_{\mu\nu} \\ &= \frac{3}{4} \partial_\mu \bar{h}_{\sigma\rho} \partial^\mu \bar{h}^{\sigma\rho} - \frac{1}{2} \partial^\rho \bar{h}^{\sigma\mu} \partial_\sigma \bar{h}_{\rho\mu} - 2a_2 \bar{h}^{\mu\nu} \partial_\mu \partial_\nu R^{(1)} \\ &\quad + 2a_2 R^{(1)2} + \frac{3a_2^2}{2} \partial_\mu R^{(1)} \partial^\mu R^{(1)}. \end{aligned} \quad (5.69c)$$

Using these

$$f^{(B)} = R^{(B)} \quad (5.70a)$$

$$f^{(1)} = R^{(1)} \quad (5.70b)$$

$$f^{(2)} = R^{(2)} + \frac{a_2}{2} R^{(1)2}, \quad (5.70c)$$

and

$$f'^{(B)} = a_2 R^{(B)} \quad (5.71a)$$

$$f'^{(0)} = 1 \quad (5.71b)$$

$$f'^{(1)} = a_2 R^{(1)} \quad (5.71c)$$

$$f'^{(2)} = a_2 R^{(2)} + \frac{a_3}{2} R^{(1)2}. \quad (5.71d)$$

We list a zeroth-order term for clarity; $R^{(B)}$ is $\mathcal{O}(\varepsilon^2)$.

Combining all of these

$$\begin{aligned}
\mathcal{G}^{(2)}_{\mu\nu} &= R^{(2)}_{\mu\nu} + f'^{(1)} R^{(1)}_{\mu\nu} - \partial_\mu \partial_\nu f'^{(2)} + \Gamma^{(1)\rho}_{\nu\mu} \partial_\rho f'^{(1)} + \gamma_{\mu\nu} \gamma^{\rho\sigma} \partial_\rho \partial_\sigma f'^{(2)} \\
&\quad - \gamma_{\mu\nu} \gamma^{\rho\sigma} \Gamma^{(1)\lambda}_{\sigma\rho} \partial_\lambda f'^{(1)} - \gamma_{\mu\nu} h^{\rho\sigma} \partial_\rho \partial_\sigma f'^{(1)} + h_{\mu\nu} \gamma^{\rho\sigma} \partial_\rho \partial_\sigma f'^{(1)} \\
&\quad - \frac{1}{2} f^{(2)} \gamma_{\mu\nu} - \frac{1}{2} f^{(1)} h_{\mu\nu} \\
&= R^{(2)}_{\mu\nu} + a_2 \left(\gamma_{\mu\nu} \square^{(B)} - \partial_\mu \partial_\nu \right) R^{(2)} - \frac{1}{2} R^{(2)} \gamma_{\mu\nu} \\
&\quad + \frac{a_3}{2} \left(\gamma_{\mu\nu} \square^{(B)} - \partial_\mu \partial_\nu \right) R^{(1)2} - \frac{1}{6} \bar{h}_{\mu\nu} R^{(1)} - a_2 \gamma_{\mu\nu} \bar{h}^{\sigma\rho} \partial_\sigma \partial_\rho R^{(1)} \\
&\quad + \frac{a_2}{2} \partial^\rho R^{(1)} \left(\partial_\mu \bar{h}_{\rho\nu} + \partial_\nu \bar{h}_{\rho\mu} - \partial_\rho \bar{h}_{\mu\nu} \right) + a_2 \left(R^{(1)} R^{(1)\mu\nu} + \frac{1}{4} R^{(1)2} \gamma_{\mu\nu} \right) \\
&\quad - a_2^2 \left(\partial_\mu R^{(1)} \partial_\nu R^{(1)} + \frac{1}{2} \gamma_{\mu\nu} \partial^\rho R^{(1)} \partial_\rho R^{(1)} \right). \tag{5.72}
\end{aligned}$$

It is simplest to split this up for the purposes of averaging. Since we average over all directions at each point, gradients average to zero (Hobson *et al.* 2006, section 17.11; Stein & Yunes 2011)

$$\langle \partial_\mu V \rangle = 0. \tag{5.73}$$

As a corollary of this

$$\langle U \partial_\mu V \rangle = - \langle V \partial_\mu U \rangle. \tag{5.74}$$

Repeated application of this, together with our gauge condition (5.39), and wave equations (5.29) and (5.45) allows us to eliminate many terms. Those that do not average to zero are the last three terms in equation (5.72) and

$$\langle R^{(2)}_{\mu\nu} \rangle = \left\langle -\frac{1}{4} \partial_\mu \bar{h}_{\sigma\rho} \partial_\nu \bar{h}^{\rho\sigma} + \frac{a_2^2}{2} \partial_\mu R^{(1)} \partial_\nu R^{(1)} + \frac{a_2}{6} \gamma_{\mu\nu} R^{(1)2} \right\rangle; \tag{5.75a}$$

$$\langle R^{(2)} \rangle = \left\langle \frac{3a_2}{2} R^{(1)2} \right\rangle; \tag{5.75b}$$

$$\langle R^{(1)} R^{(1)\mu\nu} \rangle = \left\langle a_2 R^{(1)} \partial_\mu \partial_\nu R^{(1)} + \frac{1}{6} \gamma_{\mu\nu} R^{(1)2} \right\rangle. \tag{5.75c}$$

Combining terms gives

$$\langle \mathcal{G}^{(2)}_{\mu\nu} \rangle = \left\langle -\frac{1}{4} \partial_\mu \bar{h}_{\sigma\rho} \partial_\nu \bar{h}^{\rho\sigma} - \frac{3a_2^2}{2} \partial_\mu R^{(1)} \partial_\nu R^{(1)} \right\rangle. \tag{5.76}$$

Thus we obtain the result

$$t_{\mu\nu} = \frac{1}{32\pi G} \left\langle \partial_\mu \bar{h}_{\sigma\rho} \partial_\nu \bar{h}^{\rho\sigma} + 6a_2^2 \partial_\mu R^{(1)} \partial_\nu R^{(1)} \right\rangle. \tag{5.77}$$

In the limit of $a_2 \rightarrow 0$ we obtain the familiar GR result as required. The GR result is also recovered if $R^{(1)} = 0$, as would be the case if the Ricci mode was not excited; for example, if the frequency was below the cut-off frequency Υ .

Rewriting the effective energy-momentum tensor in terms of metric perturbation $h_{\mu\nu}$, using equation (5.57),

$$t_{\mu\nu} = \frac{1}{32\pi G} \left\langle \partial_\mu h_{\sigma\rho} \partial_\nu h^{\rho\sigma} + \frac{1}{8} \partial_\mu h \partial_\nu h \right\rangle. \tag{5.78}$$

These results do not depend upon a_3 or higher-order coefficients (Stein & Yunes 2011).

This result has been subsequently confirmed by N  f & Jetzer (2011). They used the Landau-Lifshitz complex (Landau & Lifshitz 1975, section 94), appropriately generalised for $f(R)$ -gravity (Nutku 1969), to derive the result.⁵ This is equivalent to the approach used by Will (1993, section 10.3) to derive the energy flux for scalar-tensor theories. The consistency between approaches is reassuring.

The effective energy-momentum tensor could be used to constrain the parameter a_2 through observations of the energy and momentum carried away by GWs. Of particular interest would be a system with a frequency that evolved from $\omega < \Upsilon$ to $\omega > \Upsilon$, as then we would witness the switching on of the propagating Ricci mode. If we could accurately identify the cut-off frequency we could accurately measure a_2 . However, we shall see in section 6.3.3 that this is unlikely to happen.

5.6 Summary

We have introduced an alternative theory of gravity: metric $f(R)$ -gravity. By generalising the Einstein–Hilbert action to include an arbitrary function we gained extra degrees of freedom which could help us match cosmological observations. We consider an analytic function $f(R)$ which admits flat spacetime as a solution. We analysed the properties of this theory within linearised theory, concentrating on the properties of gravitational radiation. We have shown that in addition to there being two transverse modes, similar to in GR, there is an additional scalar mode. We have also calculated an effective energy-momentum tensor for the GWs using the short-wave formalism of Isaacson (1968a, b). Looking for observational constraints on these differences from GR should place constraints on the form of $f(R)$. We shall do this in the next chapter, where we also study $f(R)$ -gravity with a source instead of just in vacuo.

⁵The Landau-Lifshitz complex is defined such that the (ordinary) derivative of it plus the energy-momentum vanishes. The sum defines an energy-momentum pseudo-tensor that is conserved in the familiar way: the rate of change of energy-momentum contained in a spacial volume is given by the flux through the surface of the volume. The complex is also symmetric in its indices to ensure conservation of angular momentum.

Chapter 6

Observational constraints for $f(R)$ -gravity

In the previous chapter we introduced an extended theory of gravity, metric $f(R)$ -gravity, and derived its behaviour in the linearised framework. We now continue, to find what constraints we could place on this theory to quantify deviations from GR. In section 6.1 we look at the effects of introducing a source term and derive the weak-field metrics for a point source, a slowly rotating point source, and a uniform density sphere, recovering some results known for quadratic theories of gravity. These are used in section 6.2 to compute the frequencies of radial and vertical epicyclic oscillations about circular-equatorial orbits in the weak-field, slow-rotation metric, and hence to construct an estimate of the detectability of the $f(R)$ deviations in LISA EMRI observations. For comparison, in section 6.3, we describe the constraints on $f(R)$ -gravity that can be obtained from Solar System and laboratory tests. We conclude in section 6.4 with a summary of our findings.

6.1 $f(R)$ -gravity with a source

Having considered radiation in a vacuum, we now include a source term. We want a first-order perturbation, so the linearised field equations are

$$\mathcal{G}^{(1)}_{\mu\nu} = 8\pi G T_{\mu\nu}. \quad (6.1)$$

We again assume a Minkowski background, considering terms to $\mathcal{O}(\varepsilon)$ only. To solve the wave equations (5.29) and (5.45) with this source term we use a Green's function

$$(\square + \Upsilon^2) \mathcal{G}_\Upsilon(x, x') = \delta(x - x'), \quad (6.2)$$

where \square acts on x . The Green's function is familiar as the Klein-Gordon propagator (up to a factor of $-i$) (Peskin & Schroeder 1995, section 2.4)

$$\mathcal{G}_\Upsilon(x, x') = \int \frac{d^4 p}{(2\pi)^4} \frac{\exp[-ip \cdot (x - x')]}{\Upsilon^2 - p^2}. \quad (6.3)$$

This can be evaluated by a suitable contour integral to give

$$\mathcal{G}_\Upsilon(x, x') = \begin{cases} \int \frac{d\omega}{2\pi} \exp[-i\omega(t-t')] \frac{1}{4\pi r} \exp\left[i(\omega^2 - \Upsilon^2)^{1/2} r\right] & \omega^2 > \Upsilon^2 \\ \int \frac{d\omega}{2\pi} \exp[-i\omega(t-t')] \frac{1}{4\pi r} \exp\left[-(\Upsilon^2 - \omega^2)^{1/2} r\right] & \omega^2 < \Upsilon^2 \end{cases}, \quad (6.4)$$

where we have introduced $t = x^0$, $t' = x'^0$ and $r = |\mathbf{x} - \mathbf{x}'|$. For $\Upsilon = 0$,

$$\mathcal{G}_0(x, x') = \frac{\delta(t - t' - r)}{4\pi r}, \quad (6.5)$$

the familiar retarded-time Green's function. We can use this to solve equation (5.45)

$$\begin{aligned} \bar{h}_{\mu\nu}(x) &= -16\pi G \int d^4 x' \mathcal{G}_0(x, x') T_{\mu\nu}(x') \\ &= -4G \int d^3 x' \frac{T_{\mu\nu}(t-r, \mathbf{x}')}{r}. \end{aligned} \quad (6.6)$$

This is exactly as in GR, so we can use standard results.

Solving for the scalar mode:

$$R^{(1)}(x) = -8\pi G \Upsilon^2 \int d^4 x' \mathcal{G}_\Upsilon(x, x') T(x'). \quad (6.7)$$

To proceed further we must know the form of the trace $T(x')$. In general the form of $R^{(1)}(x)$ is complicated.

6.1.1 The Newtonian limit

Let us consider the limiting case of a Newtonian source, such that

$$T_{00} = \rho; \quad |T_{00}| \gg |T_{0i}|; \quad |T_{00}| \gg |T_{ij}|, \quad (6.8)$$

with a mass distribution of a stationary point source

$$\rho = M\delta(\mathbf{x}'). \quad (6.9)$$

This source does not produce any radiation. As in GR

$$\bar{h}_{00} = -\frac{4GM}{r}; \quad \bar{h}_{0i} = \bar{h}_{ij} = 0. \quad (6.10)$$

Solving for the Ricci scalar (Havas 1977)

$$R^{(1)} = -2G\Upsilon^2 M \frac{\exp(-\Upsilon r)}{r}. \quad (6.11)$$

Combining these in equation (5.42b) yields a metric perturbation with non-zero elements

$$h_{00} = -\frac{2GM}{r} \left[1 + \frac{\exp(-\Upsilon r)}{3} \right]; \quad h_{ij} = -\frac{2GM}{r} \left[1 - \frac{\exp(-\Upsilon r)}{3} \right] \delta_{ij}. \quad (6.12)$$

Thus, to first order, the metric for a point mass in $f(R)$ -gravity is

$$ds^2 = \left\{ 1 - \frac{2GM}{r} \left[1 + \frac{\exp(-\Upsilon r)}{3} \right] \right\} dt^2 - \left\{ 1 + \frac{2GM}{r} \left[1 - \frac{\exp(-\Upsilon r)}{3} \right] \right\} d\Sigma^2, \quad (6.13)$$

using $d\Sigma^2 = dx^2 + dy^2 + dz^2$ (Capozziello *et al.* 2007, 2009; N  f & Jetzer 2010). This is not the linearised limit of the Schwarzschild metric, although this is recovered as $a_2 \rightarrow 0$, $\Upsilon \rightarrow \infty$ (Chiba *et al.* 2007). This metric has already been derived for the case of quadratic gravity, which includes terms like R^2 and $R_{\mu\nu}R^{\mu\nu}$ in the Lagrangian (Pechlaner & Sexl 1966; Stelle 1978; Schmidt 1986; Teyssandier 1990). In linearised theory our $f(R)$ reduces to quadratic theory, as to first order $f(R) = R + a_2 R^2/2$.

Extending this result to a slowly rotating source with angular momentum J , we then have the additional term (Hobson *et al.* 2006, section 13.20)

$$\bar{h}^{0i} = -\frac{2G}{c^2 r^3} \epsilon^{ijk} J_j x_k, \quad (6.14)$$

where ϵ^{ijk} is the Levi-Civita alternating tensor. The metric is

$$\begin{aligned} ds^2 = & \left\{ 1 - \frac{2GM}{r} \left[1 + \frac{\exp(-\Upsilon r)}{3} \right] \right\} dt^2 + \frac{4GJ}{r^3} (xdy - ydx) dt \\ & - \left\{ 1 + \frac{2GM}{r} \left[1 - \frac{\exp(-\Upsilon r)}{3} \right] \right\} d\Sigma^2, \end{aligned} \quad (6.15)$$

where z is the rotation axis. This is not the first-order limit of the Kerr metric (aside from as $a_2 \rightarrow 0$, $\Upsilon \rightarrow \infty$).

In $f(R)$ -gravity Birkhoff's theorem no longer applies (Pechlaner & Sexl 1966; Stelle 1978; Clifton 2006; Capozziello & Stabile 2009; Stabile 2010): the metric about a spherically symmetric mass does not correspond to the equivalent of the Schwarzschild solution. The distribution of matter influences how the Ricci scalar decays, and consequently Gauss' theorem is not applicable. Repeating our analysis for a (nonrotating) sphere of uniform density and radius L ,

$$\bar{h}_{00} = -\frac{4GM}{r}; \quad \bar{h}_{0i} = \bar{h}_{ij} = 0, \quad (6.16)$$

as in GR, and for the point mass, but

$$\begin{aligned} R^{(1)} = & -6GM \frac{\exp(-\Upsilon r)}{r} \left[\frac{\Upsilon L \cosh(\Upsilon L) - \sinh(\Upsilon L)}{\Upsilon L^3} \right] \\ = & -6GM \frac{\exp(-\Upsilon r)}{r} \Upsilon^2 \Xi(\Upsilon L), \end{aligned} \quad (6.17)$$

defining $\Xi(\Upsilon L)$ in the last line.¹ The metric perturbation thus has non-zero first-order elements (Stelle 1978; Capozziello & Stabile 2009; Stabile 2010)

$$h_{00} = -2GM [1 + \exp(-\Upsilon r) \Xi(\Upsilon L)]; \quad h_{ij} = -2GM [1 - \exp(-\Upsilon r) \Xi(\Upsilon L)] \delta_{ij}, \quad (6.18)$$

where we have assumed that $r > L$ at all stages.²

Solving the full field equations to find the exact metric in $f(R)$ is difficult because of the higher-order derivatives that enter the equations. However, we expect a solution to have the appropriate limiting form as given above.

¹ $\Xi(0) = 1/3$ is the minimum of $\Xi(\Upsilon L)$.

²Inside the source $R^{(1)} = -(6GM/L^3)[1 - (\Upsilon L + 1) \exp(-\Upsilon L) \sinh(\Upsilon r)/\Upsilon r]$.

It has been suggested that since $R = 0$ is a valid solution to the vacuum equations, the BH solutions of GR are also the BH solutions in $f(R)$ (Psaltis *et al.* 2008; Barausse & Sotiriou 2008). We have seen that having a non-zero stress-energy tensor at the origin, because of equation (5.29), forces R to be non-zero in the surrounding vacuum, although it decays to zero at infinity (Olmo 2007). Therefore, it is not obvious that the end-state of gravitational collapse must be a GR solution and that it could not settle to a different solution.³

However, a uniqueness theorem exists for the closely related Brans-Dicke theory (Hawking 1972b; Bekenstein & Meisels 1978; Thorne & Dykla 1971; Scheel *et al.* 1995), and recently this has been extended to $f(R)$ -gravity, assuming only the stationarity of the solution (Sotiriou & Faraoni 2012). Therefore astrophysical BHs in $f(R)$ -gravity are also described by the Kerr solution. We can only detect differences in the properties of extended sources.

6.1.2 The weak-field metric

It is useful to transform the weak-field metric, equation (6.15), to the more familiar form

$$ds^2 = A(\tilde{r})dt^2 + \frac{4GJ}{\tilde{r}}\sin^2\theta d\phi dt - B(\tilde{r})d\tilde{r}^2 - \tilde{r}^2d\Omega^2. \quad (6.19)$$

The coordinate \tilde{r} is a circumferential measure, as in the Schwarzschild metric, as opposed to r , used in preceding sections, which is a radial distance (an isotropic coordinate) (Misner *et al.* 1973, section 40.1; Olmo 2007). To simplify the algebra we introduce the Schwarzschild radius

$$r_S = 2GM. \quad (6.20)$$

In the linearised regime, we require that the new radial coordinate satisfies

$$\tilde{r}^2 = \left\{ 1 + \frac{r_S}{r} \left[1 - \frac{\exp(-\Upsilon r)}{3} \right] \right\} r^2 \quad (6.21)$$

$$\tilde{r} = r + \frac{r_S}{2} \left[1 - \frac{\exp(-\Upsilon r)}{3} \right]. \quad (6.22)$$

This can be used as an implicit definition of r in terms of \tilde{r} . To first order in r_S/r (Olmo 2007)

$$A(\tilde{r}) = 1 - \frac{r_S}{\tilde{r}} \left[1 + \frac{\exp(-\Upsilon r)}{3} \right]. \quad (6.23)$$

We see that the functional form of g_{00} is almost unchanged upon substituting \tilde{r} for r , but r is left in the exponential.

To find $B(\tilde{r})$ we consider, using equation (6.22),

$$\frac{d\tilde{r}}{\tilde{r}} = d\ln \tilde{r} = \left\{ \frac{1 + \Upsilon r_S r \exp(-\Upsilon r)/6\tilde{r}}{1 + (r_S/2\tilde{r})[1 - \exp(-\Upsilon r)/3]} \right\} \frac{dr}{r}. \quad (6.24)$$

³We cannot simply extrapolate from our δ -function solution, as it is necessary to consider the junction conditions required for a physical solution (Deruelle *et al.* 2008).

Thus

$$d\tilde{r}^2 = \frac{\tilde{r}^2}{r^2} \left\{ \frac{1 + \Upsilon r_S r \exp(-\Upsilon r)/6\tilde{r}}{1 + (r_S/2\tilde{r})[1 - \exp(-\Upsilon r)/3]} \right\}^2 dr^2. \quad (6.25)$$

The term in braces is $[B(\tilde{r})]^{-1}$. We assume that in the weak-field

$$\varepsilon \sim \frac{r_S}{r} \quad (6.26)$$

is small; then the metric perturbations from Minkowski are small. Expanding to first order (Olmo 2007)

$$B(\tilde{r}) = 1 + \frac{r_S}{\tilde{r}} \left[1 - \frac{\exp(-\Upsilon r)}{3} \right] - \frac{\Upsilon r_S \exp(-\Upsilon r)}{3}. \quad (6.27)$$

In the limit $\Upsilon \rightarrow \infty$, where we recover GR, $A(\tilde{r})$ and $B(\tilde{r})$ tend to their Kerr (Schwarzschild) forms.

In the following sections we use these weak-field metrics (in both coordinates) with astrophysical and laboratory tests of gravity to place constraints on $f(R)$.

6.2 Epicyclic frequencies

One means of probing the nature of a spacetime is through observations of orbital motions (Gair *et al.* 2008). We consider the epicyclic motion produced by perturbing a circular orbit. There are two epicyclic frequencies associated with any circular-equatorial orbit, characterising perturbations in the radial and vertical directions respectively (Binney & Tremaine 2008, section 3.2.3). We start by deriving a general result for any metric of the form of equation (6.19), and then specialise to our $f(R)$ solution. We work in the slow-rotation limit, keeping only linear terms in J .

An orbit in a spacetime described by equation (6.19) has as constants of motion: the orbiting particle's rest mass, the energy (per unit mass) of the orbit E and the z -component of the angular momentum (per unit mass) L_z . Using an over-dot to denote differentiation with respect to an affine parameter, which we identify as proper time τ ,

$$E = A\dot{t} + \frac{2GJ}{\tilde{r}} \sin^2 \theta \dot{\phi}; \quad (6.28)$$

$$L_z = \tilde{r}^2 \sin^2 \theta \dot{\phi} - \frac{2GJ}{\tilde{r}} \sin^2 \theta \dot{t}. \quad (6.29)$$

For circular equatorial orbits $\dot{\tilde{r}} = \ddot{\tilde{r}} = \dot{\theta} = 0$ and $\theta = \pi/2$. The time-like geodesic equation can be written in the covariant form

$$\frac{du_\mu}{d\tau} = \frac{1}{2} (\partial_\mu g_{\rho\sigma}) u^\rho u^\sigma, \quad (6.30)$$

where u^μ is the 4-velocity. For a circular equatorial orbit, setting $\mu = \tilde{r}$ gives the frequency of the orbit $\omega_0 = d\phi/dt$ as

$$\omega_0 = -\frac{GJ}{\tilde{r}^3} \pm \frac{1}{2} \sqrt{\frac{2A'}{\tilde{r}} + \left(\frac{2GJ}{\tilde{r}^3} \right)^2}, \quad (6.31)$$

in which a prime denotes $d/d\tilde{r}$ and the $+/-$ sign denotes prograde/retrograde orbits. The definition of proper time gives

$$\dot{t} = \left(A + \frac{4GJ\omega_0}{\tilde{r}} - \tilde{r}^2\omega_0^2 \right)^{-1/2}. \quad (6.32)$$

We now have both \dot{t} and $\dot{\phi} = \omega_0\dot{t}$ as functions of \tilde{r} ; substitution into equations (6.28) and (6.29) allows us to find the energy and angular momentum in terms of \tilde{r} .

From the Hamiltonian $\mathcal{H} = g_{\mu\nu}u^\mu u^\nu$ we can obtain the general equation of motion for massive particles, using the substitutions

$$\dot{t} = \frac{E}{A} - \frac{2GJ}{A\tilde{r}^3}L_z, \quad (6.33)$$

$$\dot{\phi} = \frac{2GJE}{A\tilde{r}^3} + \frac{L_z}{\tilde{r}^2 \sin^2 \theta}, \quad (6.34)$$

where we have linearised in J , as appropriate for the slow-rotation limit. With these replacements, the general time-like geodesic equation takes the form

$$\begin{aligned} \dot{\tilde{r}}^2 + \frac{\tilde{r}^2}{B}\dot{\theta}^2 &= \frac{E^2}{AB} - \frac{4GJEL_z}{AB\tilde{r}^3} - \frac{1}{B} \left(1 + \frac{L_z^2}{\tilde{r}^2 \sin^2 \theta} \right) \\ &= V(\tilde{r}, \theta, E, L_z). \end{aligned} \quad (6.35)$$

To compute the epicyclic frequency we imagine the orbit is perturbed by a small amount, while E and L_z are unchanged.⁴ For radial perturbations $\tilde{r} = \bar{r}(1 + \delta)$, where \bar{r} is the radius of the unperturbed orbit, the orbit undergoes small oscillations with frequency

$$\dot{t}^2\Omega_{\text{rad}}^2 = -\frac{1}{2} \left. \frac{\partial^2 V}{\partial \tilde{r}^2} \right|_{\bar{r}, \theta=\pi/2}. \quad (6.36)$$

Small vertical perturbations $\theta = \pi/2 + \delta$ oscillate with frequency

$$\dot{t}^2\Omega_{\text{vert}}^2 = -\frac{1}{2} \left. \frac{B(\bar{r})}{\bar{r}^2} \frac{\partial^2 V}{\partial \theta^2} \right|_{\bar{r}, \theta=\pi/2}. \quad (6.37)$$

We denote $A(\bar{r}) \equiv \bar{A}$, $B(\bar{r}) \equiv \bar{B}$, $A'(\bar{r}) \equiv \bar{A}'$, etc.; differentiating the potential from equation (6.35) we find (Berry & Gair 2011)

$$\begin{aligned} \dot{t}^2\Omega_{\text{rad}}^2 &= -\frac{E^2}{AB} \left(\frac{\bar{A}'^2}{\bar{A}^2} - \frac{\bar{A}''}{2\bar{A}} + \frac{\bar{A}'\bar{B}'}{\bar{A}\bar{B}} + \frac{\bar{B}'^2}{\bar{B}^2} - \frac{\bar{B}''}{2\bar{B}} \right) - \frac{\bar{B}''}{2\bar{B}^2} + \frac{\bar{B}'^2}{\bar{B}^3} \\ &\quad - \frac{L_z^2}{\bar{B}\bar{r}^2} \left(\frac{\bar{B}''}{2\bar{B}} - \frac{\bar{B}'^2}{\bar{B}^2} - \frac{2\bar{B}'}{\bar{B}\bar{r}} - \frac{3}{\bar{r}^2} \right) \\ &\quad + \frac{4GJEL_z}{\bar{A}\bar{B}\bar{r}^3} \left[\frac{\bar{A}'^2}{\bar{A}^2} - \frac{\bar{A}''}{2\bar{A}} + \frac{\bar{A}'\bar{B}'}{\bar{A}\bar{B}} + \frac{\bar{B}'^2}{\bar{B}^2} - \frac{\bar{B}''}{2\bar{B}} + \frac{3}{\bar{r}} \left(\frac{\bar{A}'}{\bar{A}} + \frac{\bar{B}'}{\bar{B}} \right) + \frac{6}{\bar{r}^2} \right] \end{aligned} \quad (6.38)$$

⁴It is not possible for the orbit to be perturbed without changing the energy or angular momentum. However, these corrections are quadratic in the amplitude of the perturbation, and so can be ignored at linear order.

$$= \frac{L_z^2}{\bar{r}^3 \bar{B}} \left(\frac{\bar{A}''}{\bar{A}'} - \frac{2\bar{A}'}{\bar{A}} + \frac{3}{\bar{r}} \right) + \frac{6GJEL_z}{\bar{A}\bar{B}\bar{r}^4} \left(\frac{\bar{A}''}{\bar{A}'} + \frac{4}{\bar{r}} \right); \quad (6.39)$$

$$i\Omega_{\text{vert}} = \frac{L_z}{\bar{r}^2}. \quad (6.40)$$

To simplify equation (6.38) we used conditions imposed by setting V and $\partial V/\partial \tilde{r}$ equal to zero for circular equatorial orbits. These results hold for any metric of the general form equation (6.19), subject to the slow-rotation condition, which we have used to linearise in J at various stages.

6.2.1 Gravitational wave constraints

We now consider if the deviation arising from the $f(R)$ correction could be observable. This should be possible if the orbit is sufficiently different from its counterpart in Kerr. To quantify the difference, we must identify equivalent orbits in the two spacetimes. For circular equatorial orbits there is a natural way to do this: by identifying orbits with the same frequency ω_0 , as this is a gauge invariant observable quantity (Detweiler 2008). The quantity

$$\Delta(\omega_0, \Upsilon) = \Omega(\omega_0, \Upsilon) - \Omega(\omega_0, \Upsilon \rightarrow \infty) \quad (6.41)$$

characterises the rate of increase in the phase difference between the $f(R)$ trajectory and the Kerr trajectory with the same frequency and spin parameter (Berry & Gair 2011).⁵

Consider the GWs emitted by an object undergoing epicyclic motion. We assume that we are in the extreme-mass-ratio regime, such that we can ignore the gravity of the orbiting body. The correction is detectable if it leads to a significant phase shift in a gravitational waveform over the length of an observation; we adopt the criterion that it is detectable if $T_{\text{obs}}\Delta > 2\pi$ for observation period T_{obs} . This is a significant over-simplification. We have assumed that the orbital frequency has been matched to a Kerr value, but small changes in the other parameters such as the central object's mass or spin, the orbital eccentricity or the inclination, could mimic (or disguise) the effect. However, we are also keeping the orbital frequency fixed whereas we shall observe inspirals. This can break the parameter degeneracies. Since we are interested in extreme-mass-ratio systems, for which the inspiral proceeds slowly, it is likely that we are being over-optimistic, so these results can be considered upper bounds on what could be measurable.

EMRIs are a potential source of observation for LISA. However, these will be for systems about massive BHs. As BH spacetimes are no different in $f(R)$ -gravity, we must assume that the central object is an extended body: it must be an exotic object such as a boson star. There is no evidence for the existence of these non-standard

⁵By comparing with the $\Upsilon \rightarrow \infty$ limit of the trajectory rather than the exact Kerr result ensures that we are taking the same slow rotation limit in both cases, and we need not be concerned with $\mathcal{O}(J^2)$ corrections.

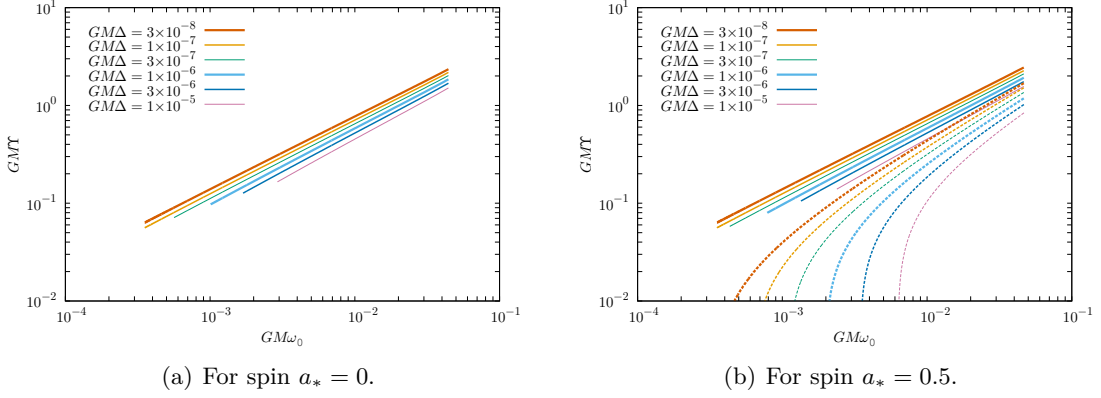


Figure 6.1 Region of parameter space in which $f(R)$ and Kerr trajectories can be distinguished. Curve corresponds to different values of the detectability criterion equation (6.42), given in the key. Dashed lines are measurements of the vertical epicyclic frequency, solid lines are for measurements of the radial epicyclic frequency. The region below a curve could be distinguishable in a LISA observation with that detectability. Taken from Berry & Gair (2011).

objects. Therefore, this analysis is only included as a sketch of what could be potentially achievable if this were the case.

The time-scale of the systems we are considering is set by the central object mass, and the quantities $M\omega_0$ and $M\Delta$ are mass-independent. A duration of a typical EMRI observation with LISA would be of the order of a year, and so the criterion for detectability becomes (Berry & Gair 2011)

$$GM\Delta = 9.8 \times 10^{-7} \left(\frac{M}{10^6 M_\odot} \right) \left(\frac{\text{yr}}{T_{\text{obs}}} \right). \quad (6.42)$$

In figure 6.1 we show the region of $\Upsilon\text{-}\omega_0$ parameter space in which corrections could be distinguished from Kerr, as defined by this criterion. Each curve represents a particular choice for $GM\Delta$: the region below the curve is detectable in an observation characterised by that choice. Equation (6.42) indicates that the curve $GM\Delta = 10^{-6}$ is what would be achieved in a one-year observation for a $10^6 M_\odot$ mass central object. The curves $GM\Delta = 10^{-5}/10^{-7}$ are the corresponding results for a $10^7/10^5 M_\odot$ mass object, while the curve $GM\Delta = 3 \times 10^{-7}$ represents what would be achieved in a three-year observation. We show results for two choices of spin: $a_* = J/GM^2 = 0$ and $a_* = 0.5$. There is not much difference between the two. The vertical epicyclic frequency is only measurable for $a_* \neq 0$ as it coincides with the orbital frequency for $a_* = 0$ as a consequence of the spherical symmetry. Results are shown only for prograde orbits. For $a_* \neq 0$, we can compute results for retrograde orbits; these differ from the prograde results by an amount which is almost indistinguishable on the scale of the plots.

From figure 6.1 we conclude that we could be able to distinguish spacetimes with $GM\Upsilon \lesssim 1$. For a $10^6 M_\odot$ central object this corresponds to $\Upsilon \lesssim 10^{-9} \text{ m}^{-1}$. Larger values are accessible at higher frequencies, but the inspiral would pass through that region quickly, and these orbits correspond to relatively small radii at which the weak-field

approximations begin to break down, so we must be cautious extrapolating these results. Using this detectability criterion, the radial epicyclic frequency is always a more powerful probe than the vertical epicyclic frequency. This is expected; the latter is generally smaller in magnitude and so accumulates fewer cycles over a typical observation.

6.3 Solar System and laboratory tests

6.3.1 Light bending and the post-Newtonian parameter γ

The parametrized post-Newtonian (PPN) formalism was created to quantify deviations from GR (Will 1993, chapter 4; Will 2006). It is ideal for Solar System tests. The only parameter we need to consider here is γ , which measures the space-curvature produced by unit rest mass. The PPN metric has components

$$g_{00}^{\text{PPN}} = 1 - 2U; \quad g_{ij}^{\text{PPN}} = -(1 + 2\gamma U)\delta_{ij}, \quad (6.43)$$

where for a point mass

$$U(r) = \frac{GM}{r}. \quad (6.44)$$

The metric must be in isotropic coordinates (Misner *et al.* 1973, section 40.1; Will 1993, section 4.1(c)). The $f(R)$ metric equation (6.13) is of a similar form, but there is not a direct correspondence because of the exponential.⁶ It has been suggested that this may be incorporated by changing the definition of the potential U (Olmo 2007; Faulkner *et al.* 2007; Bisabr 2010; De Felice & Tsujikawa 2010), then

$$\gamma = \frac{3 - \exp(-\Upsilon r)}{3 + \exp(-\Upsilon r)}. \quad (6.45)$$

As $\Upsilon \rightarrow \infty$, the GR value of $\gamma = 1$ is recovered. However, the experimental bounds for γ are derived assuming that it is a constant (Will 1993, section 6.1). Since this is not the case, we shall rederive the post-Newtonian, or $\mathcal{O}(\varepsilon)$, corrections to photon trajectories for a more general metric. We define

$$ds^2 = [1 + 2\Psi(r)] dt^2 - [1 - 2\Phi(r)] (dx^2 + dy^2 + dz^2). \quad (6.46)$$

To post-Newtonian order, this has non-zero connection coefficients

$$\Gamma^0_{0i} = \frac{\Psi'(r)x^i}{r}; \quad \Gamma^i_{00} = \frac{\Psi'(r)x^i}{r}; \quad \Gamma^i_{jk} = \frac{\Phi'(r)(\delta_{jk}x^i - \delta_{ij}x^k - \delta_{ik}x^j)}{r}. \quad (6.47)$$

The photon trajectory is described by the geodesic equation

$$\frac{d^2x^\mu}{d\sigma^2} + \Gamma^\mu_{\nu\rho} \frac{dx^\nu}{d\sigma} \frac{dx^\rho}{d\sigma} = 0, \quad (6.48)$$

⁶Our $f(R)$ theory is equivalent to a Brans-Dicke theory with a potential and parameter $\omega_{\text{BD}} = 0$ (Teyssandier & Tourrenc 1983; Wands 1994). We cannot use the familiar result $\gamma = (1 + \omega_{\text{BD}})/(2 + \omega_{\text{BD}})$ (Will 2006) as this was derived for Brans-Dicke theory without a potential (Will 1993, section 5.3).

for affine parameter σ . The time coordinate obeys

$$\frac{d^2t}{d\sigma^2} + \Gamma^0_{\nu\rho} \frac{dx^\nu}{d\sigma} \frac{dx^\rho}{d\sigma} = 0, \quad (6.49)$$

so we can rewrite the spatial components of equation (6.48) using t as an affine parameter (Will 1993, section 6.1)

$$\frac{d^2x^i}{dt^2} + \left(\Gamma^i_{\nu\rho} - \Gamma^0_{\nu\rho} \frac{dx^i}{dt} \right) \frac{dx^\nu}{dt} \frac{dx^\rho}{dt} = 0. \quad (6.50)$$

Since the geodesic is null we also have

$$g_{\mu\nu} \frac{dx^\mu}{dt} \frac{dx^\nu}{dt} = 0. \quad (6.51)$$

To post-Newtonian accuracy these become

$$\frac{d^2x^i}{dt^2} = - \left(\frac{\Psi'}{r} + \frac{\Phi'}{r} \left| \frac{d\mathbf{x}}{dt} \right|^2 \right) x^i + 2 \frac{\Psi' + \Phi'}{r} \mathbf{x} \cdot \frac{d\mathbf{x}}{dt} \frac{dx^i}{dt}, \quad (6.52)$$

$$0 = 1 + 2\Phi - (1 - 2\Phi) \left| \frac{d\mathbf{x}}{dt} \right|^2. \quad (6.53)$$

The Newtonian, or zeroth-order, solution of these is propagation in a straight line at constant speed (Will 1993, section 6.1)

$$x_N^i = n^i t; \quad |\mathbf{n}| = 1. \quad (6.54)$$

The post-Newtonian trajectory can be written as

$$x^i = n^i t + x_{pN}^i \quad (6.55)$$

where x_{pN}^i is the deviation from the straight line. Substituting this into equations (6.52) and (6.53) gives

$$\frac{d^2\mathbf{x}_{pN}}{dt^2} = - \nabla(\Psi + \Phi) + 2\mathbf{n} \cdot \nabla(\Psi + \Phi) \mathbf{n}, \quad (6.56)$$

$$\mathbf{n} \cdot \frac{d\mathbf{x}_{pN}}{dt} = \Psi + \Phi. \quad (6.57)$$

The post-Newtonian deviation only depends upon the combination $\Psi + \Phi$. From equation (6.13)

$$\begin{aligned} \Psi(r) + \Phi(r) &= - \frac{2GM}{r} \\ &= - 2U(r). \end{aligned} \quad (6.58)$$

This is identical to the form in GR. The result holds not just for a point mass, using equation (5.42b),

$$\begin{aligned} 2(\Psi + \Phi) &= h_{00} + h_{ii} \quad (\text{no summation}) \\ &= \bar{h}_{00} + \bar{h}_{ii}, \end{aligned} \quad (6.59)$$

and since $\bar{h}_{\mu\nu}$ obeys equation (5.45) exactly as in GR, there is no difference (Zhao *et al.* 2011). We conclude that an appropriate definition for the post-Newtonian parameter for light-bending is

$$\gamma = -\frac{g_{00} + g_{ii}}{2U} - 1 \quad (\text{no summation}). \quad (6.60)$$

Using this, our $f(R)$ solutions have $\gamma = 1$. This agrees with the result found by Clifton (2008).⁷ Consequently, $f(R)$ -gravity is indistinguishable from GR in this respect and is entirely consistent with the current observational value of $\gamma = 1 + (2.1 \pm 2.3) \times 10^{-5}$ (Will 2006; Bertotti *et al.* 2003).

This result has important implications. To first order, the gravitational lensing of light in $f(R)$ -gravity is identical to that in GR. Therefore, we still need dark matter to explain lensing observations of galaxies and galaxy clusters (Lubini *et al.* 2011). $f(R)$ -gravity is not an alternative to dark matter.

There are non-linear signatures of $f(R)$ -gravity that may be observable with lensing measurements; however, these are too small to be currently observable (Vanderveld *et al.* 2011). We must use other experiments to put constraints upon $f(R)$.

6.3.2 Planetary precession

The epicyclic frequencies derived in section 6.2 can be used for the classic test of planetary precession in the Solar System.⁸ Radial motion perturbs the orbit into an ellipse. The amplitude of our perturbation δ gives the eccentricity e of the ellipse (Kerner *et al.* 2001). Unless $\omega_0 = \Omega_{\text{rad}}$ the epicyclic motion is asynchronous with the orbital motion: there is periape precession. In one revolution the ellipse precesses about the focus by

$$\varpi = 2\pi \left(\frac{\omega_0}{\Omega_{\text{rad}}} - 1 \right) \quad (6.61)$$

where ω_0 is the frequency of the circular orbit given in equation (6.31). The precession is cumulative, so a small deviation may be measurable over sufficient time. Taking the non-rotating limit, the epicyclic frequency is

$$\Omega_{\text{rad}}^2 = \omega_0^2 \left[1 - \frac{3r_S}{\bar{r}} - \zeta(\Upsilon, r_S, \bar{r}) \right], \quad (6.62)$$

defining the function

$$\begin{aligned} \zeta = r_S &\left(\frac{1}{\bar{r}} + \Upsilon \right) \frac{\exp(-\Upsilon r)}{3} \\ &+ \frac{\Upsilon^2 \bar{r}^2 \exp(-\Upsilon r)}{3 + (1 + \Upsilon \bar{r}) \exp(-\Upsilon r)} \left[1 - \frac{r_S}{\bar{r}} + r_S \left(\frac{1}{\bar{r}} + \Upsilon \right) \frac{\exp(-\Upsilon r)}{3} \right]. \end{aligned} \quad (6.63)$$

⁷Clifton (2008) also gives PPN parameters $\beta = 1$, $\zeta_1 = 0$, $\zeta_3 = 0$ and $\zeta_4 = 0$, all identical to the values in GR.

⁸Since the Sun is an extended body, we do not have to worry about BH solutions being identical in GR and $f(R)$ -gravity here.

Planet	Semimajor axis $r/10^{11}$ m	Orbital period $(2\pi/\omega_0)/\text{yr}$	Precession rate $\Delta\varpi \pm \sigma_{\Delta\varpi}/\text{mas yr}^{-1}$	Eccentricity e
Mercury	0.57909175	0.24084445	-0.040 ± 0.050	0.20563069
Venus	1.0820893	0.61518257	0.24 ± 0.33	0.00677323
Earth	1.4959789	0.99997862	0.06 ± 0.07	0.01671022
Mars	2.2793664	1.88071105	-0.07 ± 0.07	0.09341233
Jupiter	7.7841202	11.85652502	0.67 ± 0.93	0.04839266
Saturn	14.267254	29.42351935	-0.10 ± 0.15	0.05415060
Uranus	28.709722	83.74740682	-38.9 ± 39.0	0.04716771
Neptune	44.982529	163.7232045	-44.4 ± 54.0	0.00858587
Pluto	59.063762	248.0208	28.4 ± 45.1	0.24880766

Table 6.1 Orbital properties of the eight major planets and Pluto. We take the semimajor orbital axis to be the flat-space distance r , not the coordinate \tilde{r} . The eccentricity is not used in calculations, but is given to assess the accuracy of neglecting terms $\mathcal{O}(e^2)$. Semimajor axis, orbital period and eccentricity are taken from Cox (2000), the precession rate is from Pitjeva (2009)

This characterises the deviation from the Schwarzschild case: the change in the precession per orbit relative to Schwarzschild is

$$\Delta\varpi = \varpi - \varpi_S \quad (6.64)$$

$$= \pi\zeta, \quad (6.65)$$

using the subscript S to denote the Schwarzschild value. To obtain the last line we have expanded to lowest order, assuming that ζ is small.⁹ Since $\zeta \geq 0$, the precession rate is enhanced relative to GR.

Table 6.1 shows the orbital properties of the planets. We use the deviation in perihelion precession rate from the GR prediction to constrain the value of ζ , and hence Υ and a_2 . All the precession rates are consistent with GR predictions ($\Delta\varpi = 0$) within their uncertainties. Assuming that these uncertainties constrain the possible deviation from GR we can use them as bounds for $f(R)$ corrections. Table 6.2 shows the constraints for Υ and a_2 obtained by equating the uncertainty in the precession rate $\sigma_{\Delta\varpi}$ with the $f(R)$ correction, and similarly using twice the uncertainty $2\sigma_{\Delta\varpi}$. The tightest constraint is obtained from the orbit of Mercury. Adopting a value of $\Upsilon \geq 5.3 \times 10^{-10} \text{ m}^{-1}$, the cut-off frequency for the Ricci mode is $\geq 0.16 \text{ s}^{-1}$. Therefore it could lie in the upper range of the LISA frequency band (Bender *et al.* 1998; Danzmann & Rüdiger 2003) or in the ground-based detector frequency range (Abramovici *et al.* 1992; Abbott *et al.* 2009; Accadida *et al.* 2010). The constraints are not as tight as those from GW observations; however, as we shall see in section 6.3.3, it is possible to place stronger constraints on Υ using laboratory experiments.

⁹There is one term in ζ that is not explicitly $\mathcal{O}(\varepsilon)$. Numerical evaluation shows that this is < 0.6 for the applicable range of parameters.

Planet	Using $\sigma_{\Delta\varpi}$		Using $2\sigma_{\Delta\varpi}$	
	$\Upsilon/10^{-11} \text{ m}^{-1}$	$ a_2 /10^{18} \text{ m}^2$	$\Upsilon/10^{-11} \text{ m}^{-1}$	$ a_2 /10^{18} \text{ m}^2$
Mercury	52.6	1.2	51.3	1.3
Venus	25.3	5.2	24.6	5.5
Earth	19.1	9.1	18.6	9.6
Mars	12.2	22	11.9	24
Jupiter	2.96	380	2.87	410
Saturn	1.69	1200	1.63	1200
Uranus	0.58	9800	0.56	11000
Neptune	0.35	28000	0.33	31000
Pluto	0.26	49000	0.25	55000

Table 6.2 Bounds calculated using uncertainties in planetary perihelion precession rates. Υ must be greater than or equal to the tabulated value, $|a_2|$ must be less than or equal to the tabulated value.

6.3.3 Fifth-force tests

From the metric (6.13), a point mass has a Yukawa gravitational potential (Stelle 1978; Capozziello *et al.* 2009; N  f & Jetzer 2010)

$$V(r) = \frac{GM}{r} \left[1 + \frac{\exp(-\Upsilon r)}{3} \right]. \quad (6.66)$$

Potentials of this form are well studied in fifth-force tests (Will 2006; Adelberger *et al.* 2009, 2003) which consider a potential defined by a coupling constant α and a length-scale λ such that

$$V(r) = \frac{GM}{r} \left[1 + \alpha \exp\left(-\frac{r}{\lambda}\right) \right]. \quad (6.67)$$

We are able to put strict constraints upon our length-scale λ_R , and hence a_2 , because our coupling constant $\alpha_R = 1/3$ is relatively large. This can be larger for extended sources: comparison with equation (6.18) shows that for a uniform sphere $\alpha_R = \Xi(\Upsilon L) \geq 1/3$.

The best constraints at short distances come from the E  t-Wash experiments, which use torsion balances (Kapner *et al.* 2007; Hoyle *et al.* 2004). These constrain $\lambda_R \lesssim 8 \times 10^{-5} \text{ m}$. Hence we determine $|a_2| \lesssim 2 \times 10^{-9} \text{ m}^2$. Similar results have been obtained by Cembranos (2009), and by N  f & Jetzer (2010). This would mean that the cut-off frequency for a propagating scalar mode would be $\gtrsim 4 \times 10^{12} \text{ s}^{-1}$ which is much higher than expected for astrophysical objects.

Fifth-force tests also permit λ_R to be large. This degeneracy can be broken using other tests; from section 6.2 we know that the large range for λ_R is excluded by planetary precession rates. This is supported by a result of N  f & Jetzer (2010) obtained using the results of Gravity Probe B (Everitt *et al.* 2009, 2011).

While the laboratory bound on λ_R may be strict compared to astronomical length-scales, it is still much greater than the expected characteristic gravitational scale, the Planck length ℓ_P . We might expect for a natural quantum theory that $a_2 \sim \mathcal{O}(\ell_P^2)$, but

$\ell_P^2 = 2.612 \times 10^{-70} \text{ m}^2$, thus the bound is still about 60 orders of magnitude greater than the natural value. The only other length-scale that we could introduce is defined by the cosmological constant Λ . Using the concordance values $\Lambda = 1.202 \times 10^{-52} \text{ m}^{-2}$ (Bennett *et al.* 2012; Hinshaw *et al.* 2012), we see that $\Lambda^{-1} \gg |a_2|$. It is intriguing combining these two length-scales we find $\ell_P/\Lambda^{1/2} = 1.474 \times 10^{-9} \text{ m}^2$, which is of the order of the current bound. This is coincidence, since there is nothing fundamental about the current level of precision, but it would be interesting to see if the measurements could be improved to rule out a Yukawa interaction around this length-scale.

6.4 Discussion of $f(R)$ -gravity

Over the course of two chapters, we have examined the possibility of testing $f(R)$ -type modifications to gravity using future GW observations and other measurements. We have seen that gravitational radiation is modified in $f(R)$ -gravity as the Ricci scalar is no longer constrained to be zero; in linearised theory there is an additional mode of oscillation, that of the Ricci scalar. This can only propagate above a cut-off frequency, but once excited, does carry additional energy-momentum away from the source. The two transverse GW modes are modified from their GR counterparts to include a contribution from the Ricci scalar, which would allow us to probe the curvature of the strong-field source regions. However, further study is needed in order to understand how GWs behave in a region with background curvature, in particular, when R is non-zero.

From linearised theory we have deduced the weak-field metrics for some simple mass distributions and found they are not the same as in GR. Birkhoff's theorem no longer applies in $f(R)$ -gravity, and extended bodies have a different gravitational field than in GR. However, the BH metrics of GR remain solutions in $f(R)$ -gravity. This restricts the potential GW observations that could be made to test $f(R)$ theories.

LISA observations of EMRIs are sensitive to small differences in the precession frequencies of orbits: even tiny differences accumulate into a measurable dephasing over the $\sim 10^5$ cycles LISA would observe. However, as BHs are identical in both GR and $f(R)$ -gravity there would be no difference in the orbital frequencies. There would be a difference if the compact object was an exotic extended object; in this case deviations would only be detectable when $|a_2| \gtrsim 10^{17} \text{ m}^2$, assuming an extreme-mass-ratio binary with a massive object of mass $\sim 10^6 M_\odot$. This is calculated using the weak-field, slow-rotation metric. There could still be differences in the evolution of the inspiral because of a difference in the self-force.

We calculated constraints that can be placed using Solar System observations of planetary precessions and laboratory experiments. While the LISA constraints could beat those from Solar System observations (which presently give $|a_2| \lesssim 1.2 \times 10^{18} \text{ m}^2$), considerably stronger constraints have already been placed from fifth-force tests. Using

existing results from the Eöt-Wash experiment, we constrain $|a_2| \lesssim 2 \times 10^{-9} \text{ m}^2$. For this range of a_2 , we do expect the propagating Ricci mode to be excited by astrophysical systems as the cut-off frequency is too high. However, even in the absence of excitation of the Ricci mode, gravitational radiation in $f(R)$ -gravity is still modified through the dependence of the transverse polarizations on the Ricci scalar.

Although the constraints from astrophysical observations are much weaker than this laboratory bound, they are still of interest since they probe gravity at a different scale and in a different environment. It is possible that $f(R)$ -gravity is not universal, but changes in different regions of space or at different energy scales. The $f(R)$ model could be regarded as an approximate effective theory, and the range of validity of a particular parameterization is limited to a specific scale. For example, the effective theory in the vicinity of a massive BH, where the curvature is large, could be distinct from the appropriate effective theory in the Solar System, where curvature is small; or $f(R)$ could evolve with cosmological epoch such that it varies with redshift. If the laboratory bound is indeed universal there should be no deviation in GW observations: detection of a deviation would prove both that GR is incomplete and that the effective a_2 varies with environment.

One method of obtaining variation in the behaviour of gravity is via the chameleon mechanism. Then $f(R)$ -gravity is modified in the presence of matter (Khoury & Weltman 2004b, a; Brax *et al.* 2004; Khoury 2013). In metric $f(R)$ -gravity this is a non-linear effect arising from a large departure of the Ricci scalar from its background value (De Felice & Tsujikawa 2010). The mass of the effective scalar degree of freedom then depends upon the density of its environment (Faulkner *et al.* 2007; Li & Barrow 2007). In a region of high matter density, such as the Earth, the deviations from standard gravity would be exponentially suppressed due to a large effective Υ ; while on cosmological scales, where the density is low, the scalar would have a small Υ , perhaps of the order H_0/c (Khoury & Weltman 2004b, a). The chameleon mechanism allows $f(R)$ -gravity to pass laboratory, or Solar System, tests while potentially remaining of interest for cosmology.¹⁰ In the context of gravitational radiation, this would mean that the Ricci scalar mode could freely propagate on cosmological scales (Corda 2009b). Unfortunately, because the chameleon mechanism suppresses the effects of $f(R)$ in the presence of matter, this mode would have to be excited by something other than the acceleration of matter. Additionally, since electromagnetic radiation has a traceless energy-momentum tensor it cannot excite the Ricci mode.¹¹ To be able to detect the Ricci mode we must observe it

¹⁰The need to reconcile laboratory experiments with a non-trivial $f(R)$ could be regarded as motivation for introducing the chameleon mechanism.

¹¹The standard transverse polarizations of gravitational radiation have an energy-momentum tensor that averages to be traceless, although this may not be the case locally (Butcher *et al.* 2010); the contribution to the gravitational averaged energy-momentum tensor from a propagating Ricci mode does have a non-zero trace, see equation (5.77). In any case it is doubtful that gravitational energy-momentum

well away from any matter, which would cause it to become evanescent: a space-borne detector such as LISA could be our only hope.

As the chameleon mechanism is inherently non-linear, it is difficult to discuss in terms of our linearised framework. Treating $f(R)$ as an effective theory, we could incorporate the effects of matter by taking the coefficients $\{a_n\}$ to be functions of the matter stress-energy tensor (or its trace). In this case, the results presented here would hold in the event that the coefficient a_2 is slowly varying, such that it may be treated as approximately constant in the region of interest. The linearised wave equations, (5.29) and (5.45), retain the same form in the case of a variable a_2 ; the only alteration would be that $a_2 R^{(1)}$ replaces $R^{(1)}$ as subject of the Klein-Gordon equation. In particular, the conclusion that $\gamma = 1$ is unaffected by the possibility of a variable a_2 .

An interesting extension to the work presented here would be to consider the case when the constant term in the function $f(R)$, a_0 , is non-zero. We would then be able to study perturbations with respect to (anti-)de Sitter space. This is relevant because the current Λ CDM paradigm indicates that we live in a universe with a positive cosmological constant (Jarosik *et al.* 2011; Komatsu *et al.* 2011). Such a study would naturally complement an investigation into the effects of background curvature on propagation (Yang *et al.* 2011).

could act as a source for detectable radiation.

Part IV

Conclusion

Part V

Appendices

Appendix A

The signal inner product

We wish to derive an inner product over the space of signals; we shall denote the product of signals g and h as $(g|h)$. The use of the inner product is well established in GW astronomy (Jaranowski & Królak 2012).

A.1 Preliminaries

A.1.1 The Fourier transform

We begin with some basic properties of Fourier transform (Riley *et al.* 2002, section 13.1). We define transformations

$$x(t) = \int_{-\infty}^{\infty} \tilde{x}(f) \exp(2\pi ift) \, df \quad (\text{A.1a})$$

$$\tilde{x}(f) = \int_{-\infty}^{\infty} x(t) \exp(-2\pi ift) \, dt. \quad (\text{A.1b})$$

The Dirac delta-function arises as

$$\delta(f) = \int_{-\infty}^{\infty} \exp(-2\pi ift) \, dt. \quad (\text{A.2})$$

We shall use Plancherel's theorem which proves the unitarity of the Fourier transformation

$$\begin{aligned} \int_{-\infty}^{\infty} |x(t)|^2 \, dt &= \int_{-\infty}^{\infty} dt \int_{-\infty}^{\infty} \tilde{x}(f) \exp(2\pi ift) \, df \int_{-\infty}^{\infty} \tilde{x}^*(f') \exp(-2\pi if't) \, df' \\ &= \int_{-\infty}^{\infty} |\tilde{x}(f)|^2 \, df. \end{aligned} \quad (\text{A.3})$$

A.1.2 The Wiener–Khinchin theorem

We begin by deriving the Wiener–Khinchin theorem (Kittel 1958, chapter 28). For a real signal we have $\tilde{x}(f) = \tilde{x}^*(f)$, and since $\tilde{x}(f) = \tilde{x}^*(-f)$,

$$|\tilde{x}(f)|^2 = |\tilde{x}(-f)|^2. \quad (\text{A.4})$$

We use $\langle \dots \rangle$ to denote time averaging, then

$$\langle x^2 \rangle = \lim_{T \rightarrow \infty} \frac{1}{2T} \int_{-T}^T [x(t)]^2 dt. \quad (\text{A.5})$$

Applying Plancherel's theorem for our real signal

$$\langle x^2 \rangle = \lim_{T \rightarrow \infty} \frac{1}{2T} \int_{-\infty}^{\infty} |\tilde{x}(f)|^2 df = \lim_{T \rightarrow \infty} \frac{1}{T} \int_0^{\infty} |\tilde{x}(f)|^2 df. \quad (\text{A.6})$$

The power spectrum $G(f)$ is

$$G(f) = \lim_{T \rightarrow \infty} \frac{1}{T} \overline{|\tilde{x}(f)|^2}, \quad (\text{A.7})$$

where an overline represents an ensemble average. Therefore

$$\overline{\langle x^2 \rangle} = \int_0^{\infty} G(f) df. \quad (\text{A.8})$$

If $x(t)$ is a randomly varying signal we can use the ergodic principle to equate a time average with an ensemble over multiple realisations. Hence $\overline{\langle x^2 \rangle} = \langle x^2 \rangle$ and we can drop the overline.

The correlation function for a random process is

$$C(\tau) = \langle x(t)x(t + \tau) \rangle \quad (\text{A.9})$$

$$\begin{aligned} &= \lim_{T \rightarrow \infty} \frac{1}{2T} \int_{-T}^T dt \int_{-\infty}^{\infty} \tilde{x}(f) \exp(2\pi ift) df \int_{-\infty}^{\infty} \tilde{x}(f') \exp[2\pi if'(t + \tau)] df' \\ &= \lim_{T \rightarrow \infty} \frac{1}{2T} \int_{-\infty}^{\infty} |\tilde{x}(f)|^2 \exp(2\pi if\tau) df. \end{aligned} \quad (\text{A.10})$$

We can rewrite this in terms of the power spectrum

$$C(\tau) = \frac{1}{2} \int_{-\infty}^{\infty} G(f) \exp(2\pi if\tau) df = \int_0^{\infty} G(f) \cos(2\pi f\tau) df. \quad (\text{A.11})$$

Inverting these

$$G(f) = 2 \int_{-\infty}^{\infty} C(\tau) \exp(-2\pi if\tau) d\tau = 4 \int_0^{\infty} C(\tau) \cos(2\pi f\tau) d\tau. \quad (\text{A.12})$$

The power spectrum and correlation function are related to each other by the Fourier transform. This is the Wiener–Khinchin theorem.

A.2 Defining the inner product

A.2.1 Gaussian noise

We consider a normally distributed noise signal $n(t)$ with zero mean and standard deviation σ_n . The variance is

$$\langle n^2 \rangle = C_n(0) = \sigma_n^2, \quad (\text{A.13})$$

introducing correlation function $C_n(\tau)$. If we have a measured signal $s(t)$ and a true signal $h(t)$, the probability $p(s|h)$ is that of the realisation of noise such

$$s = h + n. \quad (\text{A.14})$$

Let us consider a discrete signal $n_i \equiv n(t_i)$, with $t_i - t_j = (i-j)\Delta t$ $\{i, j = -N, \dots, N\}$ and $\Delta T = 2T/(2N+1)$. For a single point (Finn 1992),

$$p(s_i|h_i) = \frac{1}{\sqrt{2\pi C_n(0)}} \exp\left[-\frac{1}{2} \frac{n_i^2}{C_n(0)}\right]. \quad (\text{A.15})$$

Expanding this to the entire signal

$$p(s|h) = \frac{1}{\sqrt{(2\pi)^{2N+1} \det C_{n,ij}}} \exp\left[-\frac{1}{2} \sum_{k,l} C_{kl}^{-1} n_k n_l\right], \quad (\text{A.16})$$

introducing short-hand $C_{n,ij} \equiv C_n(t_i - t_j)$ and defining the inverse matrix C_{kl}^{-1} such that

$$\delta_{jl} = \sum_l C_{n,jk} C_{kl}^{-1}. \quad (\text{A.17})$$

To transform to the continuum (and infinite duration) limit we identify

$$\lim_{T \rightarrow \infty; \Delta t \rightarrow 0} \sum_j \Delta t \rightarrow \lim_{T \rightarrow \infty} \int_{-T}^T dt_j. \quad (\text{A.18})$$

To change between Kronecker and Dirac deltas

$$\sum_j \delta_{jk} = \int_{-T}^T \delta(t_j - t_k) dt_j, \quad (\text{A.19})$$

hence

$$\delta(t_j - t_k) = \lim_{\Delta t \rightarrow 0} \frac{1}{\Delta t} \delta_{jk}. \quad (\text{A.20})$$

Using the inverse matrix definition

$$\begin{aligned} \exp(-2\pi i f t_k) &= \sum_j \exp(-2\pi i f t_j) \delta_{jk} \\ &= \frac{1}{(\Delta t)^2} \sum_j \Delta t \exp(-2\pi i f t_j) \sum_l \Delta t C_{n,jl} C_{lk}^{-1}. \end{aligned} \quad (\text{A.21})$$

Taking the limit

$$\begin{aligned} \exp(-2\pi i f t_k) &= \lim_{T \rightarrow \infty; \Delta t \rightarrow 0} \frac{1}{(\Delta t)^2} \int_{-T}^T \exp(-2\pi i f t_j) dt_j \int_{-T}^T C_n(t_j - t_l) C^{-1}(t_l, t_k) dt_l \\ &= \lim_{\Delta t \rightarrow 0} \frac{1}{(\Delta t)^2} \int_{-\infty}^{\infty} C_n(\tau) \exp(-2\pi i f \tau) d\tau \\ &\quad \times \int_{-\infty}^{\infty} C^{-1}(t_l, t_k) \exp(-2\pi i f t_l) dt_l, \end{aligned} \quad (\text{A.22})$$

where $\tau = t_j - t_l$. Defining the transformation

$$\widetilde{C}^{-1}(f, t_k) = \int_{-\infty}^{\infty} C^{-1}(t, t_k) \exp(-2\pi i f t) dt, \quad (\text{A.23})$$

and using the Wiener–Khinchin theorem to define power spectral density (Cutler & Flanagan 1994)

$$S_n(f) = \lim_{T \rightarrow \infty} \frac{1}{T} \overline{|\tilde{n}(f)|^2} \quad (\text{A.24})$$

$$= 2 \int_{-\infty}^{\infty} C_n(\tau) \exp(-2\pi i f \tau) d\tau, \quad (\text{A.25})$$

we have

$$\exp(-2\pi i f t_k) = \lim_{\Delta t \rightarrow 0} \frac{1}{(\Delta t)^2} \frac{S_n(f)}{2} \widetilde{C^{-1}}(f, t_k). \quad (\text{A.26})$$

This can be rearranged to define $\widetilde{C^{-1}}(f, t_k)$ (Finn 1992).

The term in the exponential in equation (A.16) has the limit

$$\begin{aligned} \mathcal{H} &= \frac{1}{2} \lim_{T \rightarrow \infty; \Delta t \rightarrow 0} \sum_{j,k} C_{jk}^{-1} n_j n_k \\ &= \frac{1}{2} \lim_{T \rightarrow \infty; \Delta t \rightarrow 0} \frac{1}{(\Delta t)^2} \int_{-T}^T dt_j \int_{-T}^T dt_k C^{-1}(t_j, t_k) n(t_j) n(t_k) \\ &= \frac{1}{2} \lim_{\Delta t \rightarrow 0} \frac{1}{(\Delta t)^2} \int_{-\infty}^{\infty} dt_k \int_{-\infty}^{\infty} df \widetilde{C^{-1}}(f, t_k) \tilde{n}(-f) n(t_k) \\ &= \int_{-\infty}^{\infty} \frac{\tilde{n}^*(f) \tilde{n}(f)}{S_n(f)} df \\ &= \frac{1}{2} (n|n), \end{aligned} \quad (\text{A.27})$$

defining the inner product (Finn 1992)

$$(g|h) = 2 \int_{-\infty}^{\infty} \frac{\tilde{g}^*(f) \tilde{h}(f)}{S_n(f)} df = 2 \int_0^{\infty} \frac{\tilde{g}^*(f) \tilde{h}(f) + \tilde{g}(f) \tilde{h}^*(f)}{S_n(f)} df. \quad (\text{A.28})$$

This is a noise-weighted inner product over the space of real signals. The probability of the signal is (Cutler & Flanagan 1994)

$$p(s|h) \propto \exp \left[-\frac{1}{2} (n|n) \right]. \quad (\text{A.29})$$

A.2.2 Noise power spectral density

We have defined the power spectral density $S_n(f)$ using the Wiener–Khinchin theorem. It is more usual to define it in terms of the average of the noise spectrum. We shall again appeal to the ergodic principle to equate noise time and ensemble averages. Averaging two frequency components

$$\begin{aligned} \langle \tilde{n}(f) \tilde{n}^*(f') \rangle &= \lim_{T \rightarrow \infty} \frac{1}{2T} \int_{-T}^T \tilde{n}(f) \exp(2\pi i f \tau) \tilde{n}^*(f') \exp(2\pi i f' \tau) d\tau \\ &= \lim_{T \rightarrow \infty} \frac{1}{2T} \tilde{n}(f) \tilde{n}^*(f') \delta(f - f'). \end{aligned} \quad (\text{A.30})$$

Taking the ensemble average of both sides, and exploiting the properties of the delta-function, we can use equation (A.24) to identify (Cutler & Flanagan 1994)

$$\langle \tilde{n}(f) \tilde{n}^*(f') \rangle = \frac{1}{2} S_n(f) \delta(f - f'). \quad (\text{A.31})$$

This can serve as a definition for the noise power spectral density.

Appendix B

Windowing and Fourier analysis

B.1 Spectral leakage

When performing a Fourier transform using a computer we must necessarily only transform a finite time-span τ . The effect of this is the same as transforming the true, infinite signal multiplied by a unit top-hat function of width τ . Transforming yields the true waveform convolved with a sinc. If $\tilde{h}'(f)$ is the computed Fourier transform then

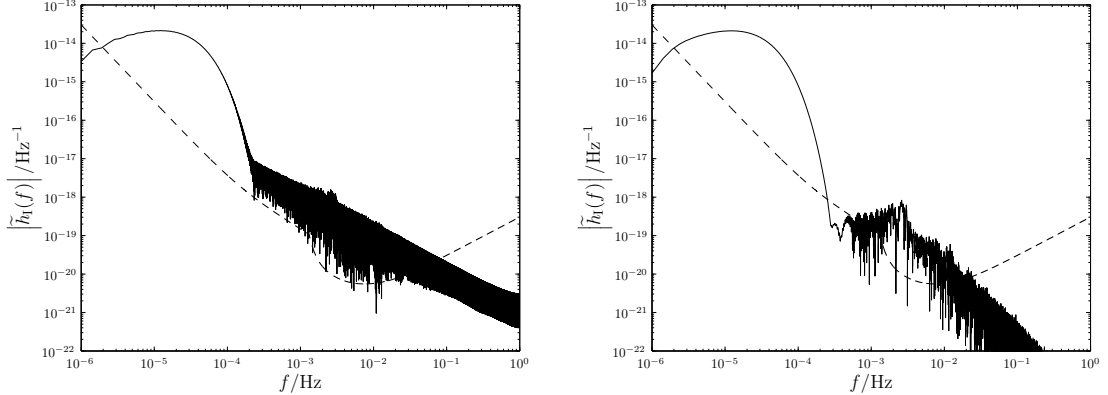
$$\tilde{h}'(f) = \int_{-\tau/2}^{\tau/2} h(t) \exp(2\pi i f t) dt = [\tilde{h}(f) * \tau \operatorname{sinc}(\pi f \tau)], \quad (\text{B.1})$$

where $\tilde{h}(f) = \mathcal{F}\{h(t)\}$ is the unwindowed Fourier transform of the infinite signal. This windowing of the data is a problem innate in the method, and results in spectral leakage.

Figure B.1(a) shows the computed Fourier transform for an example EMRB. The waveform has two distinct regions: a low-frequency curve, and a high-frequency tail. The low-frequency signal is the spectrum we are interested in; the high-frequency components are a combination of spectral leakage and numerical noise. The $\mathcal{O}(1/f)$ behaviour of the sinc gives the shape of the tail.¹

Despite being many orders of magnitude below the peak level, the high-frequency tail is still well above the noise curve for a wide range of frequencies. It therefore contributes to the evaluation of any inner products, and could mask interesting features. It is possible to reduce, but unfortunately not eliminate, the leakage using apodization: to improve the frequency response of a finite time series one can use a weighting window function $w(t)$ which modifies the impulse response in a prescribed way.

¹This has possibly been misidentified in figure 8 of Burko & Khanna (2007) as the characteristic strain for parabolic encounters.



(a) Spectrum using no window. The calculated SNR is $\rho \simeq 12.5$.

(b) Spectrum using a Nuttall window. The calculated SNR is $\rho \simeq 8.5$.

Figure B.1 Example spectra calculated using (a) a rectangular window and (b) Nuttall’s four-term window with continuous first derivative (Nuttall 1981). The spin of the MBH is $a_* = 0.5$, the mass of the orbiting CO is $\mu = 10M_\odot$, the periapsis is $r_p = 50r_g$ and the inclination is $\iota = 0.1$. The high-frequency tail is the result of spectral leakage. The level of the *LISA* noise curve is indicated by the dashed line. The spectra are from detector I, but the detector II spectra look similar.

B.2 Window functions

The simplest window function is the rectangular (or Dirichlet) window $w_R(t)$; this is the top-hat described above. Other window functions are generally tapered.² There is a wide range of window functions described in the literature (Harris 1978; Kaiser & Schafer 1980; Nuttall 1981; McKechnie *et al.* 2010). The introduction of a window function influences the spectrum in a manner dependent upon its precise shape. There are two distinct distortions: local smearing due to the finite width of the centre lobe, and distant leakage due to finite amplitude sidelobes. The window function may be optimised such that the peak sidelobe has a small amplitude, or such that the sidelobes decay away rapidly with frequency. Choosing a window function is a trade-off between these various properties, and depends upon the particular application.

For use with the parabolic spectra, the primary concern is to suppress the sidelobes. Many windows with good sidelobe behaviour exist; we consider three: the Blackman–Harris minimum four-term window (Harris 1978; Nuttall 1981)

$$w_{\text{BH}}(t) = \sum_{n=0}^3 a_n^{\text{BH}} \cos\left(\frac{2n\pi t}{\tau}\right), \quad (\text{B.2})$$

where

$$a_0^{\text{BH}} = 0.35875, \quad a_1^{\text{BH}} = 0.48829, \quad a_2^{\text{BH}} = 0.14128, \quad a_3^{\text{BH}} = 0.01168; \quad (\text{B.3})$$

²When using a tapered window function it is important to ensure that the window is centred upon the signal; otherwise the calculated transform has a reduced amplitude.

the Nuttall four-term window with continuous first derivative (Nuttall 1981)

$$w_N(t) = \sum_{n=0}^3 a_n^N \cos\left(\frac{2n\pi t}{\tau}\right), \quad (\text{B.4})$$

where

$$a_0^N = 0.355768, \quad a_1^N = 0.487396, \quad a_2^N = 0.144232, \quad a_3^N = 0.012604, \quad (\text{B.5})$$

and the Kaiser–Bessel window (Harris 1978; Kaiser & Schafer 1980)

$$w_{\text{KB}}(t; \beta) = \frac{I_0\left[\beta\sqrt{1 - (2t/\tau)^2}\right]}{I_0(\beta)}, \quad (\text{B.6})$$

where $I_\nu(z)$ is the modified Bessel function of the first kind, and β is an adjustable parameter. Increasing β reduces the peak sidelobe, but also widens the central lobe.

The Kaiser–Bessel window has the smallest peak sidelobe, but the worst decay ($1/f$); the Nuttall window has the best asymptotic behaviour ($1/f^3$); the Blackman–Harris window has a peak sidelobe similar to the Nuttall window, and decays asymptotically as fast (slow) as the Kaiser–Bessel window, but has the advantage of having suppressed sidelobes next to the central lobe.

Another window has been recently suggested for use with gravitational waveforms: the Planck–taper window (Damour *et al.* 2000; McKechnie *et al.* 2010)

$$w_P(t; \epsilon) = \begin{cases} \frac{1}{\exp(Z_+) + 1} & -\frac{\tau}{2} \leq t < -\tau\left(\frac{1}{2} - \epsilon\right) \\ 1 & -\tau\left(\frac{1}{2} - \epsilon\right) < t < \tau\left(\frac{1}{2} - \epsilon\right) \\ \frac{1}{\exp(Z_-) + 1} & \tau\left(\frac{1}{2} - \epsilon\right) < t \leq \frac{\tau}{2} \end{cases}, \quad (\text{B.7})$$

with

$$Z_\pm(t; \epsilon) = 2\epsilon \left[\frac{1}{1 \pm 2(t/\tau)} + \frac{1}{1 - 2\epsilon \pm 2(t/\tau)} \right]. \quad (\text{B.8})$$

This was put forward for use with binary coalescences, and has superb asymptotic decay. However, the peak sidelobe is high, which is disadvantageous here. We therefore propose a new window function: the Planck–Bessel window which combines the Kaiser–Bessel and Planck–taper windows to produce a window which inherits the best features of both, albeit in a diluted form,

$$w_{\text{PB}}(t; \beta, \epsilon) = w_P(t; \epsilon)w_{\text{KB}}(t; \beta). \quad (\text{B.9})$$

The window functions' frequency responses are plotted in figure B.2. There is no window that performs best everywhere.

Figure B.1 shows the computed Fourier transforms for an example EMRB using no window (alternatively a rectangular window), and the Nuttall window.³ Using the Nuttall window, the spectral leakage is greatly reduced; the peak sidelobe is lower, and the tail decays away as $1/f^3$ instead of $1/f$. The low frequency signal is not appreciably changed.

³The Blackman–Harris, Kaiser–Bessel and Planck–Bessel windows give almost identical results.

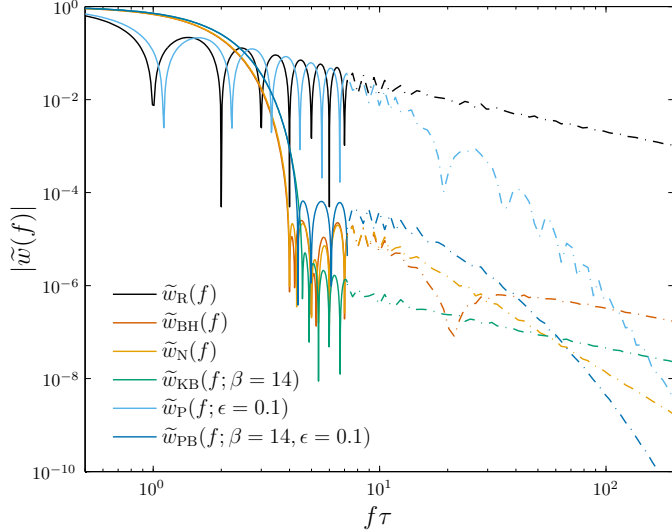


Figure B.2 Window function frequency response. To avoid clutter, the response function is only plotted in detail until $f\tau = 8$, above this a smoothed value is used, as indicated by the dot-dashed line. As well as having good asymptotic behaviour, the Planck–taper window has the narrowest main lobe, except for the rectangular window.

B.3 Influence on results

The choice of window function influences the results as it changes the form of $\tilde{h}(f)$. The variation in results between windows depends upon the signal: variation is greatest for low frequency bursts, as then there is greatest scope for leakage into the detector band; variation is least significant for orbits with small periapses as then there are strong signals to relatively high frequencies, and spectral leakage is confined mostly to below the noise level. Preliminary investigations showed that the choice of window function (excluding the rectangular window) negligibly influences results for the closest orbits. As the periapse increases, such that the peak frequency decreases, differences begin to appear. To quantify the influence, we studied the diagonal elements of the Fisher matrix (section 3.2.1) from a selection of orbits about the GC with periapses ranging from $\sim 10r_g$ – $300r_g$. For orbits with small periapses all five windows (excluding the rectangular window) produced very similar results: the Planck–taper window differed by a maximum of $\sim 0.5\%$ from the others, which all agreed to better than 0.1% . The worst case results came from the lowest frequency orbits (which extend beyond the range of detectability), then the Planck–taper window deviated by a maximum of $\sim 30\%$ in the value for the Fisher matrix elements, the Blackman–Harris deviated by $\sim 20\%$ and the others agreed to better than $\sim 5\%$. The Planck–taper window’s performance is limited by its poor sidelobe behaviour; the Blackman–Harris is limited by its performance at high frequencies.

For this work we have used the Nuttall window. Its performance is comparable to

the Kaiser–Bessel and Planck–Bessel windows, but it is computationally less expensive as it does not contain Bessel functions. Results should be accurate to a few percent at worst, and results from closer orbits, which provide better constraints, should be less affected by the choice of window function. We expect that any inaccuracies as a consequence of windowing are no greater than the error expected from using a numerical kludge approximation to generate the waveforms. Therefore, we are confident that none of our conclusions are sensitive to the particular windowing method implemented.

Appendix C

Semirelativistic fluxes

The semirelativistic approximation for extreme-mass-ratio waveforms uses an exact geodesic of the background for the trajectory of the orbiting body, but only uses the flat-space radiation generation formula (Ruffini & Sasaki 1981). This is at the heart of the numerical kludge approximation. Gair, Kennefick & Larson (2005) derived analytic formulae for the fluxes of energy and angular momentum using the semirelativistic approximation for Schwarzschild geometry. These are useful for checking the accuracy of the numerical kludge waveforms.

The published expressions contain a number of (minor) errors; we rederive the correct forms. We consider an object of mass m orbiting about another of mass M , with a trajectory specified by eccentricity e and periapsis r_p . For this section we use geometric units with $G = c = 1$.

The geodesic equations in Schwarzschild are

$$\frac{dt}{d\tau} = \left(1 - \frac{2M}{r}\right)^{-1} E, \quad (\text{C.1a})$$

$$\left(\frac{dr}{d\tau}\right)^2 = (E^2 - 1) + \frac{2M}{r} \left(1 + \frac{L_z^2}{r^2}\right) - \frac{L_z^2}{r^2}, \quad (\text{C.1b})$$

$$\frac{d\phi}{d\tau} = \frac{L_z}{r^2}, \quad (\text{C.1c})$$

where t , r and ϕ are the usual Schwarzschild coordinates, τ is the proper time, and we have introduced specific energy E and azimuthal angular momentum L_z . Spherical symmetry has been exploited to set $\theta = \pi/2$ without loss of generality. For bound orbits, the radial equation has three roots, and can be written as

$$\left(\frac{dr}{d\tau}\right)^2 = - (E^2 - 1) \frac{(r_a - r)(r - r_p)(r - r_3)}{r^3}. \quad (\text{C.2})$$

The turning points are the apoapsis, the periapsis and a third root; the orbit becomes unstable when $r_p = r_3$. An eccentricity can be defined, in analogy to Keplerian orbits, such that

$$r_a = \frac{1+e}{1-e} r_p. \quad (\text{C.3})$$

The third root is then

$$r_3 = \frac{2(1+e)M}{(1+e)r_p - 4M} r_p. \quad (\text{C.4})$$

The last stable orbit with a given eccentricity, has periapse radius

$$r_{p,\text{LSO}} = \frac{2(3+e)M}{1+e}. \quad (\text{C.5})$$

Orbits that approach closer than this will plunge into the black hole.

The parameters $\{r_p, e\}$ can be used to characterise orbits in place of $\{E, L_z\}$. The two are related by

$$E^2 = 1 - \frac{(1-e)[(1+e)r_p - 4M]M}{[(1+e)r_p - (3+e^2)M]r_p}; \quad (\text{C.6})$$

$$L_z^2 = \frac{(1+e)^2 M r_p^2}{(1+e)r_p - (3+e^2)M}. \quad (\text{C.7})$$

Following the semirelativistic approximation, the fluxes of energy and angular momentum are derived by inserting the Schwarzschild geodesic into the flat-space radiation formulae, identifying the coordinate t with the flat-space time (Misner *et al.* 1973, chapter 36)

$$\mu \frac{dE}{dt} = -\frac{1}{5} \left\langle \frac{d^3 I_{ij}}{dt^3} \frac{d^3 I^{ij}}{dt^3} \right\rangle, \quad (\text{C.8})$$

$$\mu \frac{dL_z}{dt} = -\frac{2}{5} \left\langle \frac{d^2 I_{xi}}{dt^2} \frac{d^3 I^{iy}}{dt^3} - \frac{d^2 I_{yi}}{dt^2} \frac{d^3 I^{iz}}{dt^3} \right\rangle, \quad (\text{C.9})$$

where $I_{ij} = I_{ij} - (1/3)I\delta_{ij}$ is the reduced mass quadrupole tensor and $\langle \dots \rangle$ indicates averaging over several wavelengths (or periods). For a point particle, the mass quadrupole is

$$I^{jk} = \mu x^j x^k, \quad (\text{C.10})$$

for trajectory $x^i(t)$. This is determined from the geodesic equations, and written as a function of r_p , e and r . To calculate the total change over one orbit we integrate r from r_p to r_a and back again. For this purpose it is easier to consider derivatives with respect to r . The integrands are rational functions of r and the square root of a cubic in r ; the integrals can thus be written as a combination of elliptic integrals.

The integrals are of a general form

$$\mathcal{J}_n = \int_{r_p}^{r_a} \frac{M^{n+1}}{r^n \sqrt{(r_a - r)(r - r_p)(r - r_3)r}} dr. \quad (\text{C.11})$$

By considering the derivative of $r^{-n} \sqrt{(r_a - r)(r - r_p)(r - r_3)r}$ we may derive a recurrence relationship using integration by parts. After some rearrangement

$$\mathcal{J}_n = \frac{n-1}{2n-1} \mathcal{J}_{n-1} - \frac{2n-3}{2n-1} \frac{(r_a + r_p + r_3)M^2}{r_a r_p r_3} \mathcal{J}_{n-2} + \frac{2(n-2)}{2n-1} \frac{M^3}{r_a r_p r_3} \mathcal{J}_{n-3}. \quad (\text{C.12})$$

Setting $n = 2$, the third term vanishes, hence the integrals \mathcal{I}_0 and \mathcal{I}_1 are sufficient to specify the series.¹ The zeroth integral can be evaluated using Gradshteyn & Ryzhik (2000, 3.147.6) as

$$\mathcal{I}_0 = \frac{2M}{\sqrt{r_p(r_a - r_3)}} K \left[\sqrt{\frac{(r_a - r_p)r_3}{(r_a - r_3)r_p}} \right], \quad (\text{C.13})$$

where $K(k)$ is the complete elliptic integral of the first kind. The next integral can be evaluated using Gradshteyn & Ryzhik (2000, 3.149.6) as

$$\begin{aligned} \mathcal{I}_1 = & \frac{2M^2}{r_p r_3 \sqrt{r_p(r_a - r_3)}} \left\{ r_p K \left[\sqrt{\frac{(r_a - r_p)r_3}{(r_a - r_3)r_p}} \right] \right. \\ & \left. - (r_p - r_3) \Pi \left[\frac{(r_a - r_p)r_3}{(r_a - r_3)r_p}, \sqrt{\frac{(r_a - r_p)r_3}{(r_a - r_3)r_p}} \right] \right\}, \end{aligned} \quad (\text{C.14})$$

where $\Pi(n, k)$ is the complete elliptic integral of the third kind. In this instance we may simplify using Olver *et al.* (2010, 19.6.2)

$$\Pi(k^2, k) = \frac{E(k)}{1 - k^2} \quad (\text{C.15})$$

to rewrite in terms of the complete elliptic integral of the second kind. Hence

$$\mathcal{I}_1 = \frac{2M^2}{r_3 \sqrt{r_p(r_a - r_3)}} \left\{ K \left[\sqrt{\frac{(r_a - r_p)r_3}{(r_a - r_3)r_p}} \right] - \frac{r_a - r_3}{r_a} E \left[\sqrt{\frac{(r_a - r_p)r_3}{(r_a - r_3)r_p}} \right] \right\}. \quad (\text{C.16})$$

The elliptic integrals in both \mathcal{I}_0 and \mathcal{I}_1 share the same argument, which can be rewritten as

$$\sqrt{\frac{(r_a - r_p)r_3}{(r_a - r_3)r_p}} = \sqrt{\frac{4eM}{(1 + e)r_p - 2(3 - e)M}}. \quad (\text{C.17})$$

Substituting in for the integrals, we find that the energy lost in one orbit is

$$\begin{aligned} \frac{M}{m} \Delta E = & - \frac{16M^{11}}{1673196525r_p^6(1 + e)^{19/2} \{(r_p - 2M)[(1 + e)r_p - 2(1 - e)M]\}^{5/2}} \\ & \times \left\{ \sqrt{(1 + e)\frac{r_p}{M} - 2(3 - e)} E \left[\sqrt{\frac{4eM}{(1 + e)r_p - 2(3 - e)M}} \right] f_1 \left(\frac{r_p}{M}, e \right) \right. \\ & \left. + \frac{1 + e}{\sqrt{(1 + e)(r_p/M) - 2(3 - e)}} K \left[\sqrt{\frac{4eM}{(1 + e)r_p - 2(3 - e)M}} \right] f_2 \left(\frac{r_p}{M}, e \right) \right\}, \end{aligned} \quad (\text{C.18})$$

where we have introduced functions²

$$\begin{aligned} f_1(y, e) = & 4608(1 - e)(1 + e)^2 (3 + e^2)^2 (2428691599 + 313957879e^2 \\ & + 1279504693e^4 + 63843717e^6) \\ & - 192(1 + e)^2 (908960573673 - 155717471796e^2 \end{aligned}$$

¹The integral \mathcal{I}_{-1} could be calculated using Gradshteyn & Ryzhik (2000, 3.148.6).

²The following functional forms are long and so are split over multiple pages.

$$\begin{aligned}
& - 88736969547e^4 - 293676299040e^6 - 195313674237e^8 \\
& - 26635698156e^{10} - 346799201e^{12} \Big) y \\
& + 384(1+e)^3 \left(336063804453 - 53956775638e^2 - 33318942522e^4 \right. \\
& \left. - 92857670352e^6 - 41764459155e^8 - 2765710514e^{10} \right) y^2 \\
& - 16(1+e)^4 \left(3418907055555 - 580720618635e^2 - 168432860626e^4 \right. \\
& \left. - 606890963686e^6 - 176495184865e^8 - 3768291999e^{10} \right) y^3 \\
& + 32(1+e)^5 \left(510454645597 - 92175635794e^2 \right. \\
& \left. + 26432814256e^4 - 28250211070e^6 - 5713846269e^8 \right) y^4 \\
& - 4(1+e)^6 \left(1107402703901 - 174239346926e^2 \right. \\
& \left. + 100957560852e^4 + 3707280110e^6 - 899162673e^8 \right) y^5 \\
& + 8(1+e)^7 \left(143625217397 - 16032820010e^2 \right. \\
& \left. + 4238287541e^4 + 275190560e^6 \right) y^6 \\
& - (1+e)^8 \left(220627324753 - 14884378223e^2 \right. \\
& \left. - 1210713997e^4 + 14138955e^6 \right) y^7 \\
& + 8(1+e)^9 \left(2922108518 - 46504603e^2 - 2407656e^4 \right) y^8 \\
& - 3(1+e)^{10} \left(241579935 + 6314675e^2 - 149426e^4 \right) y^9 \\
& - 4(1+e)^{11} \left(8608805 - 48992e^2 \right) y^{10} \\
& - 2(1+e)^{12} \left(1242083 - 16320e^2 \right) y^{11} \\
& - 184320(1+e)^{13}y^{12} - 5120(1+e)^{14}y^{13}
\end{aligned} \tag{C.19}$$

and

$$\begin{aligned}
f_2(y, e) = & 3072(3-e)(3+e) \left(3 + e^2 \right) \left(7286074797 - 3299041125e^2 \right. \\
& \left. + 792940362e^4 - 1366777698e^6 - 369698151e^8 - 5932745e^{10} \right) \\
& - 384(1+e) \left(2989180413711 - 583867932642e^2 - 131661872359e^4 \right. \\
& \left. - 419423580924e^6 - 194293515951e^8 - 3390301442e^{10} + 1353430119e^{12} \right) y \\
& + 64(1+e)^2 \left(14825178681327 - 2675442646782e^2 - 728511901515e^4 \right. \\
& \left. - 1837874368340e^6 - 591999524567e^8 1856757710e^{10} + 841581651e^{12} \right) y^2 \\
& - 32(1+e)^3 \left(14292163934541 - 2666166422089e^2 - 522582885086e^4 \right. \\
& \left. - 1347373382962e^6 - 307066297439e^8 - 1675056789e^{10} \right) y^3 \\
& + 16(1+e)^4 \left(9557748374919 - 1917809903861e^2 - 24258045506e^4 \right. \\
& \left. - 511875047746e^6 - 86779453317e^8 - 462078345e^{10} \right) y^4 \\
& - 8(1+e)^5 \left(5390797838491 - 990602472036e^2 + 161182699002e^4 \right)
\end{aligned}$$

$$\begin{aligned}
& - 89978894004e^6 - 11363685245e^8 \Big) y^5 \\
& + 4(1+e)^6 \left(2857676457065 - 351292910556e^2 + 79840371470e^4 \right. \\
& \left. - 2670080940e^6 - 463345647e^8 \right) y^6 \\
& - 2(1+e)^7 \left(1249768416047 - 79903103833e^2 \right. \\
& \left. + 12179840133e^4 + 482157413e^6 \right) y^7 \\
& + (1+e)^8 \left(363565648057 - 10040939153e^2 \right. \\
& \left. - 318841465e^4 + 14611473e^6 \right) y^8 \\
& - 2(1+e)^9 \left(13862653487 - 100645509e^2 - 11015842e^4 \right) y^9 \\
& + (1+e)^{10} \left(518128485 + 16345427e^2 - 421398e^4 \right) y^{10} \\
& + 16(1+e)^{11} \left(1220639 - 13448e^2 \right) y^{11} \\
& + 2(1+e)^{12} \left(689123 - 18880e^2 \right) y^{12} \\
& + 153600(1+e)^{13}y^{13} + 5120(1+e)^{14}y^{14}. \tag{C.20}
\end{aligned}$$

The angular momentum lost is

$$\begin{aligned}
\frac{\Delta L_z}{m} = & - \frac{16M^{15/2}}{24249225(1+e)^{13/2}r_p^{7/2}(r_p - 2M)^2 [(1+e)r_p - 2(1-e)M]^2} \\
& \times \left\{ \sqrt{(1+e)\frac{r_p}{M} - 2(3-e)} E \left[\sqrt{\frac{4eM}{(1+e)r_p - 2(3-e)M}} \right] g_1 \left(\frac{r_p}{M}, e \right) \right. \\
& \left. + \frac{(1+e)}{\sqrt{(1+e)(r_p/M) - 2(3-e)}} K \left[\sqrt{\frac{4eM}{(1+e)r_p - 2(3-e)M}} \right] g_2 \left(\frac{r_p}{M}, e \right) \right\} \tag{C.21}
\end{aligned}$$

where

$$\begin{aligned}
g_1(y, e) = & 169728(1-e)(1+e)^2 \left(279297 + 219897e^2 + 106299e^4 + 9611e^6 \right) \\
& - 384(1+e)^2 \left(192524061 - 13847615e^2 - 36165965e^4 \right. \\
& \left. - 20710173e^6 - 588532e^8 \right) y \\
& + 192(1+e)^3 \left(235976417 + 13109547e^2 - 3369705e^4 - 3292707e^6 \right) y^2 \\
& - 16(1+e)^4 \left(813592799 + 112906199e^2 + 53843933e^4 + 602061e^6 \right) y^3 \\
& + 16(1+e)^5 \left(87491089 + 7247482e^2 + 4608349e^4 \right) y^4 \\
& + 8(1+e)^6 \left(9580616 + 6179243e^2 - 92047e^4 \right) y^5 \\
& - 4(1+e)^7 \left(3760123 + 272087e^2 \right) y^6 \\
& - (1+e)^8 \left(1168355 - 35347e^2 \right) y^7 \\
& - 71792(1+e)^9y^8 - 4120(1+e)^{10}y^9 \tag{C.22}
\end{aligned}$$

and

$$\begin{aligned}
g_2(y, e) = & 339456(3 - e)(3 + e) \left(93099 - 10213e^2 - 18155e^4 - 10551e^6 - 420e^8 \right) \\
& - 1536(1 + e) \left(319648410 - 35712133e^2 - 33099777e^4 \right. \\
& \left. - 11272311e^6 + 457187e^8 \right) y \\
& + 128(1 + e)^2 \left(2706209781 - 45415294e^2 - 103634296e^4 \right. \\
& \left. - 34056010e^6 - 130293e^8 \right) y^2 \\
& - 32(1 + e)^3 \left(3895435659 + 212168215e^2 + 4641265e^4 - 15197651e^6 \right) y^3 \\
& + 16(1 + e)^4 \left(1396737473 + 123722895e^2 + 27602127e^4 - 465119e^6 \right) y^4 \\
& - 16(1 + e)^5 \left(78148621 + 3035912e^2 + 3130827e^4 \right) y^5 \\
& - 16(1 + e)^6 \left(8005570 + 1485159e^2 - 47943e^4 \right) y^6 \\
& + 2(1 + e)^7 \left(4015181 + 601959e^2 \right) y^7 \\
& + (1 + e)^8 \left(737603 - 39467e^2 \right) y^8 \\
& + 47072(1 + e)^9 y^9 + 4120(1 + e)^{10} y^{10}.
\end{aligned} \tag{C.23}$$

Taking limit $r_p \rightarrow \infty$ should recover weak field results. Using series expansions of the elliptic integrals for small arguments

$$\begin{aligned}
\frac{M}{m} \Delta E \simeq & - \frac{64\pi}{5} \frac{1}{(1 + e)^{7/2}} \left(1 + \frac{73}{24}e^2 + \frac{37}{96}e^4 \right) \left(\frac{M}{r_p} \right)^{7/2} \\
& - \frac{192\pi}{5} \frac{1}{(1 + e)^{9/2}} \left(1 + \frac{31}{8}e^2 + \frac{65}{32}e^4 + \frac{1}{6}e^6 \right) \left(\frac{M}{r_p} \right)^{9/2} \\
& + \mathcal{O}\left(\frac{M^{11/2}}{r_p^{11/2}}\right)
\end{aligned} \tag{C.24}$$

$$\begin{aligned}
\frac{\Delta L_z}{m} \simeq & - \frac{64\pi}{5} \frac{1}{(1 + e)^2} \left(1 + \frac{7}{8}e^2 \right) \left(\frac{M}{r_p} \right)^2 \\
& - \frac{192\pi}{5} \frac{1}{(1 + e)^3} \left(1 + \frac{35}{24}e^2 + \frac{1}{4}e^4 \right) \left(\frac{M}{r_p} \right)^3 + \mathcal{O}\left(\frac{M^4}{r_p^4}\right).
\end{aligned} \tag{C.25}$$

The leading order terms correspond to the Keplerian results of Peters (1964).

For a parabolic orbit with $e = 1$, the energy loss reduces to

$$\begin{aligned}
\frac{M}{m} \Delta E = & - \frac{2^{7/2} M^{21/2}}{1673196525 (r_p - 2M)^2 r_p^{17/2}} \left[E \left(\sqrt{\frac{2M}{r_p - 2M}} \right) f_1 \left(\frac{r_p}{M} \right) \right. \\
& \left. + K \left(\sqrt{\frac{2M}{r_p - 2M}} \right) f_2 \left(\frac{r_p}{M} \right) \right]
\end{aligned} \tag{C.26}$$

where

$$f_1(y) = -2y \left(27850061568 - 83550184704y + 117662445984y^2 - 102686941680y^3 \right)$$

$$\begin{aligned}
 & + 64808064704y^4 - 33026468872y^5 + 12784148218y^6 - 2873196259y^7 \\
 & + 185808888y^8 + 17119626y^9 + 2451526y^{10} + 368640y^{11} + 20480y^{12} \quad (\text{C.27})
 \end{aligned}$$

and

$$\begin{aligned}
 f_2(y) = & - 72901570560 + 274404834816y - 424693524096y^2 \\
 & + 378109481088y^3 - 249480499840y^4 + 154011967968y^5 \\
 & - 84437171728y^6 + 31689370996y^7 - 6231594434y^8 + 321950817y^9 \\
 & + 27462280y^{10} + 4073612y^{11} + 696320y^{12} + 40960y^{13}. \quad (\text{C.28})
 \end{aligned}$$

The angular momentum lost is

$$\begin{aligned}
 \frac{\Delta L_z}{m} = & \frac{64M^7}{24249225r_p^{11/2}(r_p - 2M)^{3/2}} \left[E\left(\sqrt{\frac{2M}{r_p - 2M}}\right) g_1\left(\frac{r_p}{M}\right) \right. \\
 & \left. + K\left(\sqrt{\frac{2M}{r_p - 2M}}\right) g_2\left(\frac{r_p}{M}\right) \right], \quad (\text{C.29})
 \end{aligned}$$

where

$$\begin{aligned}
 g_1(y) = & 181817664y - 363635328y^2 - 245236248y^3 - 49673460y^4 \\
 & - 7833906y^5 + 2016105y^6 + 283252y^7 + 35896y^8 + 4120y^9 \quad (\text{C.30})
 \end{aligned}$$

and

$$\begin{aligned}
 g_2(y) = & 71285760 - 324389184y + 468548880y^2 - 277856496y^3 + 54521424y^4 \\
 & + 6181872y^5 - 1630457y^6 - 238086y^7 - 31776y^8 - 4120y^9. \quad (\text{C.31})
 \end{aligned}$$

Appendix D

The loss cone

When considering the orbits of stars about a massive black hole (MBH), the loss cone describes a region of velocity space that is depopulated because of tidal disruption (Frank & Rees 1976; Lightman & Shapiro 1977; Merritt 2013).

A main sequence star may be disrupted by tidal forces before it is swallowed by a MBH; we define the tidal disruption radius as r_T . We expect any orbit that passes inside r_T is depopulated unless stars can successfully escape to another orbit before being disrupted. Stars' velocities change because of gravitational interaction with other stars. Deflections can be modelled as a series of two-body encounters, the cumulative effect of which is a random walk in velocity space (Chandrasekhar 1960, chapter 2). Changes scale with the square-root of time, with the relaxation time-scale τ_R setting the scale.

Consider a typical star at a distance r from the MBH. We decompose its motion into radial and tangential components as

$$v_r = v \cos \theta; \quad v_\perp = v \sin \theta. \quad (\text{D.1})$$

Over a dynamical time-scale t_{dyn} , we expect that stars change velocity by a typical amount

$$\theta_D \approx \left(\frac{t_{\text{dyn}}}{\tau_R} \right)^{1/2}, \quad (\text{D.2})$$

assuming this change is small. We introduce the loss cone angle θ_{LC} to describe the range of trajectories that shall proceed to pass within a distance r_T of the MBH. By comparing the diffusion and loss cone angles we can deduce if we would expect orbits to be depleted: if $\theta_D > \theta_{LC}$ a star can safely diffuse out of the loss cone before it is destroyed, whereas if $\theta_D < \theta_{LC}$ a star is disrupted before it can change its velocity sufficiently, leading to the depopulation of the orbit.

Frank & Rees (1976) first introduced the loss cone. They considered stars on nearly radial orbits. The orbital energy and angular momentum (per unit mass) of an object with eccentricity e and periapse radius r_p are

$$\mathcal{E} = -\frac{GM_\bullet(1-e)}{2r_p}; \quad (\text{D.3})$$

$$\mathcal{J}^2 = GM_{\bullet}(1+e)r_p, \quad (\text{D.4})$$

where M_{\bullet} is the MBH's mass. The angular momentum can also be defined as

$$\begin{aligned} \mathcal{J}^2 &= v_{\perp}^2 r^2 \\ &\simeq \theta^2 v^2 r^2, \end{aligned} \quad (\text{D.5})$$

using the small angle approximation. Frank & Rees (1976) took the limit $e \rightarrow 1$ and then set $r_p = r_T$ to demarcate the limit of the loss cone; we rearrange to find

$$\theta_{\text{LC}} \simeq \frac{2GM_{\bullet}r_T}{v^2 r^2}. \quad (\text{D.6})$$

We need to find the speed at r . Frank & Rees (1976) used a typical value

$$v^2 \simeq 3\sigma^2, \quad (\text{D.7})$$

where σ is the 1D velocity dispersion. They assumed the velocity dispersion is Keplerian within the core region, where dynamics are dominated by the MBH, and is a constant outside of this

$$\sigma^2 \simeq \begin{cases} \frac{GM_{\bullet}}{r} & r < r_c \\ \frac{GM_{\bullet}}{r_c} & r > r_c \end{cases}. \quad (\text{D.8})$$

The core radius r_c is

$$r_c = \frac{GM_{\bullet}}{\sigma_0^2}, \quad (\text{D.9})$$

where σ_0 is the 1D velocity dispersion far from the MBH. Substituting for v^2 in equation (D.6) gives

$$\theta_{\text{LC}}^2 \simeq \begin{cases} \frac{2r_T}{3r} & r < r_c \\ \frac{2r_T r_c}{3r^2} & r > r_c \end{cases}. \quad (\text{D.10})$$

Frank & Rees (1976) made one final modification, introducing a gravitational focusing factor f such that

$$\theta_{\text{LC}} \simeq f \begin{cases} \left(\frac{2r_T}{3r}\right)^{1/2} & r < r_c \\ \left(\frac{2r_T r_c}{3r^2}\right)^{1/2} & r > r_c \end{cases}. \quad (\text{D.11})$$

The focusing factor could be imagined as the correction from assuming that stars travel along straight lines, such that $\tan \theta_{\text{LC}} = r_T/r$, to accounting for a Keplerian trajectory about the MBH.

It is unappealing to include an arbitrary, albeit order unitary, factor. Additionally, there are various restrictive approximations in the derivation. Considering the orbital energy for $v^2 = 3\sigma^2$ inside the core

$$\frac{3GM_{\bullet}}{2r} - \frac{GM_{\bullet}}{r} = -\frac{GM_{\bullet}(1-e)}{2r_T} \quad (\text{D.12})$$

$$\implies \frac{r_T}{r} = e - 1. \quad (\text{D.13})$$

Since the radii must be positive, this enforces that $e \geq 1$: the orbits could be marginally bound at best. As we have taken the limit $e \rightarrow 1$, assuming that $r \gg r_T$ this is still self-consistent. However, it is desirable to relax these conditions.

Let us consider an orbit with $r_p = r_T$, which gives the edge of the loss cone. The angular momentum squared is

$$\sin^2 \theta_{LC} v^2 r^2 = GM_\bullet(1 + e)r_T. \quad (\text{D.14})$$

The energy is

$$\frac{v^2}{2} - \frac{GM_\bullet}{r} = -\frac{GM_\bullet(1 - e)}{2r_T}. \quad (\text{D.15})$$

Combining these to eliminate the velocity gives

$$\sin^2 \theta_{LC} = \frac{(1 + e)r_T^2}{2rr_T - (1 - e)r^2}. \quad (\text{D.16})$$

This has been obtained without making any assumptions about the velocity dispersion or the position of the star. Since we have considered the Keplerian orbit, there should be no need to introduce a focusing factor.

This is similar in form to the classic result. Consider an orbit with eccentricity $e = 1 - \epsilon$, where ϵ is small. Let us choose the star to be at a characteristic distance set by its semimajor axis $a = r_p/(1 - e)$, such that

$$r = \frac{r_T}{\epsilon}. \quad (\text{D.17})$$

This ensures that $r \gg r_T$. Therefore, we have matched the assumptions of Frank & Rees (1976). Substituting into our loss cone formula

$$\begin{aligned} \sin^2 \theta_{LC} &= \frac{(2 - \epsilon)r_T^2}{2rr_T + \epsilon r^2} \\ &\simeq \frac{2r_T}{3r}, \end{aligned} \quad (\text{D.18})$$

retaining terms to first order in ϵ . Since this is small, we can use the small angle approximation to recover the result of equation (D.10).

References

- Abadie, J. *et al.*; *Classical and Quantum Gravity*; **27**(17):173001; 2010; [arXiv:1003.2480](#).
- Abbott, B. *et al.*; *Physical Review D*; **76**(8):082001(35); 2007; [arXiv:gr-qc/0605028](#).
- Abbott, B.P. *et al.*; *Reports on Progress in Physics*; **72**(7):076901(25); 2009; [arXiv:0711.3041](#).
- Abramovici, A. *et al.*; *Science*; **256**(5055):325–333; 1992.
- Accadia, T. *et al.*; *Journal of Physics: Conference Series*; **203**(1):012074(5); 2010.
- Accadia, T. *et al.*; *Classical and Quantum Gravity*; **28**(11):114002(10); 2011.
- Acernese, F. *et al.*; *Journal of Physics: Conference Series*; **120**(3):032007(7); 2008.
- Adams, D.; *The Hitchhikers' Guide to the Galaxy*; London: Pan Books; first edition; 1979.
- Adams, J.C.; *The Scientific Papers of John Couch Adams*; volume I; Cambridge: Cambridge University Press; 1896.
- Adelberger, E., Gundlach, J., Heckel, B., Hoedl, S. & Schlamminger, S.; *Progress in Particle and Nuclear Physics*; **62**(1):102–134; 2009.
- Adelberger, E., Heckel, B. & Nelson, A.; *Annual Review of Nuclear and Particle Science*; **53**(1):77–121; 2003; [arXiv:hep-ph/0307284](#).
- Alexander, T. & Hopman, C.; *The Astrophysical Journal*; **697**(2):1861–1869; 2009; [arXiv:0808.3150](#).
- Althaus, L.G., Córscico, A.H., Isern, J. & García-Berro, E.; *The Astronomy and Astrophysics Review*; **18**(4):471–566; 2010; [arXiv:1007.2659](#).
- Amaro-Seoane, P. *et al.*; *Classical and Quantum Gravity*; **29**(12):124016(20); 2012; [arXiv:1202.0839](#).
- Amaro-Seoane, P. *et al.*; *Classical and Quantum Gravity*; **24**(17):R113–R169; 2007; [arXiv:astro-ph/0703495](#).
- Ando, M. *et al.*; *Classical and Quantum Gravity*; **27**(8):084010(10); 2010.
- Andrieu, C. & Thoms, J.; *Statistics and Computing*; **18**(4):343–373; 2008.
- Antoniadis, J. *et al.*; *Science*; **340**(6131):1233232(9); 2013; [arXiv:1304.6875](#).
- Antonucci, F. *et al.*; *Classical and Quantum Gravity*; **29**(12):124014(10); 2012.
- Anza, S. *et al.*; *Classical and Quantum Gravity*; **22**(10):S125–S138; 2005.
- Babak, S., Fang, H., Gair, J., Glampedakis, K. & Hughes, S.; *Physical Review D*; **75**(2):024005(25); 2007; [arXiv:gr-qc/0607007](#).
- Babak, S., Gair, J.R., Petiteau, A. & Sesana, A.; *Classical and Quantum Gravity*; **28**(11):114001(15); 2011; [arXiv:1011.2062](#).
- Babcock, H.; *Lick Observatory bulletin*; **19**(498):41–51; 1939.
- Backer, D.C. & Sramek, R.A.; *The Astrophysical Journal*; **524**(2):805–815; 1999; [arXiv:astro-ph/9906048](#).
- Bahcall, J.N. & Wolf, R.A.; *The Astrophysical Journal*; **216**(3):883–907; 1977.
- Bambi, C. & Freese, K.; *Physical Review D*; **79**(4):043002(7); 2009; [arXiv:0812.1328](#).
- Barack, L.; *Classical and Quantum Gravity*; **26**(21):213001(56); 2009; [arXiv:0908.1664](#).
- Barack, L. & Cutler, C.; *Physical Review D*; **69**(8):082005(24); 2004; [arXiv:gr-qc/0310125](#).
- Barausse, E., Sotiriou, T.P. & Miller, J.C.; *Classical and Quantum Gravity*; **25**(10):105008(15); 2008a; [arXiv:0712.1141](#).

- Barausse, E. & Sotiriou, T.P.; *Physical Review Letters*; **101**(9):099001(1); 2008; [arXiv:0803.3433](#).
- Barausse, E., Sotiriou, T.P. & Miller, J.C.; *Classical and Quantum Gravity*; **25**(6):062001(7); 2008b; [arXiv:gr-qc/0703132](#).
- Bédard, M.; *The Annals of Applied Probability*; **17**(4):1222–1244; 2007; [arXiv:0710.3684](#).
- Bédard, M.; *Journal of Computational and Graphical Statistics*; **17**(2):312–332; 2008a.
- Bédard, M.; *Stochastic Processes and their Applications*; **118**(12):2198–2222; 2008b.
- Bekenstein, J.D.; *The Astrophysical Journal*; **183**(2):657–664; 1973.
- Bekenstein, J.D. & Meisels, A.; *Physical Review D*; **18**(12):4378–4386; 1978.
- Bélanger, G., Terrier, R., de Jager, O.C., Goldwurm, A. & Melia, F.; *Journal of Physics: Conference Series*; **54**(1):420–426; 2006; [arXiv:astro-ph/0604337](#).
- Bender, P. et al.; ‘LISA Pre-Phase A Report’; Technical report; Max-Planck-Institut für Quantenoptik; Garching; 1998.
- Bender, P.L. et al.; *Science*; **182**(4109):229–38; 1973.
- Bender, R. et al.; *The Astrophysical Journal*; **631**(1):280–300; 2005; [arXiv:astro-ph/0509839](#).
- Bennett, C.L. et al.; **176**; 2012; [arXiv:1212.5225](#).
- Bergmann, A.G., Petrosian, V. & Lynds, R.; *The Astrophysical Journal*; **350**(1):23–35; 1990.
- Berrier, J.C. et al.; *The Astrophysical Journal*; **769**(2):132(17); 2013; [arXiv:1304.4937](#).
- Berry, C.P.L. & Gair, J.R.; *Physical Review D*; **82**(10):107501(4); 2010; [arXiv:1010.3865](#).
- Berry, C.P.L. & Gair, J.R.; *Physical Review D*; **83**(10):104022(19); 2011; [arXiv:1104.0819](#).
- Berti, E. et al.; *Physical Review D*; **76**(6):064034(40); 2007; [arXiv:gr-qc/0703053](#).
- Berti, E. & Volonteri, M.; *The Astrophysical Journal*; **684**(2):822–828; 2008; [arXiv:0802.0025](#).
- Bertone, G., Hooper, D. & Silk, J.; *Physics Reports*; **405**(5-6):279–390; 2005; [arXiv:hep-ph/0404175](#).
- Bertotti, B., Iess, L. & Tortora, P.; *Nature*; **425**(6956):374–376; 2003.
- Binétruy, P. et al.; *Journal of Cosmology and Astroparticle Physics*; **2012**(06):027(70); 2012; [arXiv:1201.0983](#).
- Binney, J. & Tremaine, S.; *Galactic Dynamics*; Princeton Series in Astrophysics; Princeton, New Jersey: Princeton University Press; second edition; 2008.
- Bisabr, Y.; *Gravitation and Cosmology*; **16**(3):239–244; 2010; [arXiv:1005.5670](#).
- Boyer, R.H. & Lindquist, R.W.; *Journal of Mathematical Physics*; **8**(2):265–281; 1967.
- Brax, P., van de Bruck, C., Davis, A.C., Khouri, J. & Weltman, A.; *Physical Review D*; **70**(12):123518(18); 2004; [arXiv:astro-ph/0408415](#).
- Brenneman, L.W. et al.; *The Astrophysical Journal*; **736**(2):103(10); 2011; [arXiv:1104.1172](#).
- Brenneman, L.W. & Reynolds, C.S.; *The Astrophysical Journal*; **652**(2):1028–1043; 2006; [arXiv:astro-ph/0608502](#).
- Breton, R.P. et al.; *Science*; **321**(5885):104–107; 2008; [arXiv:0807.2644](#).
- Broderick, A.E., Fish, V.L., Doeleman, S.S. & Loeb, A.; *The Astrophysical Journal*; **697**(1):45–54; 2009a; [arXiv:0809.4490](#).
- Broderick, A.E., Loeb, A. & Narayan, R.; *The Astrophysical Journal*; **701**(2):1357–1366; 2009b; [arXiv:0903.1105](#).
- Broderick, A.E., Loeb, A. & Reid, M.J.; *The Astrophysical Journal*; **735**(1):57(18); 2011; [arXiv:1104.3146](#).
- Buchdahl, H.A.; *Monthly Notices of the Royal Astronomical Society*; **150**(1):1–8; 1970.
- Burko, L.M. & Khanna, G.; *Europhysics Letters (EPL)*; **78**(6):60005(6); 2007; [arXiv:gr-qc/0609002](#).
- Butcher, L.M., Hobson, M. & Lasenby, A.; *Physical Review D*; **82**(10):104040(20); 2010; [arXiv:1008.4061](#).
- Capozziello, S., Corda, C. & De Laurentis, M.F.; *Physics Letters B*; **669**(5):255–259; 2008; [arXiv:0812.2272](#).
- Capozziello, S. & Stabile, A.; *Classical and Quantum Gravity*; **26**(8):085019(22); 2009;

- [arXiv:0903.3238](#).
- Capozziello, S., Stabile, A. & Troisi, A.; *Physical Review D*; **76**(10):104019(12); 2007; [arXiv:0708.0723](#).
- Capozziello, S., Stabile, A. & Troisi, A.; *Modern Physics Letters A*; **24**(09):659–665; 2009; [arXiv:0901.0448](#).
- Capozziello, S. & Francaviglia, M.; *General Relativity and Gravitation*; **40**(2-3):357–420; 2007; [arXiv:0706.1146](#).
- Carroll, S.M.; *Living Reviews in Relativity*; **4**(1); 2001; [arXiv:astro-ph/0004075](#).
- Carter, B.; *Physical Review Letters*; **26**(6):331–333; 1971.
- Carter, B.; *Physical Review*; **174**(5):1559–1571; 1968.
- Cembranos, J.A.R.; *Physical Review Letters*; **102**(14):141301(4); 2009; [arXiv:0809.1653](#).
- Chandrasekhar, S.; *Principles of Stellar Dynamics*; New York: Dover Publications; enlarged edition; 1960.
- Chandrasekhar, S.; *The Mathematical Theory of Black Holes*; Oxford Classic Texts in the Physical Sciences; Oxford: Oxford University Press; 1992.
- Chiba, T., Smith, T. & Erickcek, A.; *Physical Review D*; **75**(12):124014(7); 2007; [arXiv:astro-ph/0611867](#).
- Clifton, T.; *Classical and Quantum Gravity*; **23**(24):7445–7453; 2006; [arXiv:gr-qc/0607096](#).
- Clifton, T.; *Physical Review D*; **77**(2):024041(11); 2008; [arXiv:0801.0983](#).
- Clowe, D. et al.; *The Astrophysical Journal*; **648**(2):L109–L113; 2006; [arXiv:astro-ph/0608407](#).
- Corda, C.; *International Journal of Modern Physics A*; **23**(10):1521–1535; 2008; [arXiv:0711.4917](#).
- Corda, C.; *International Journal of Modern Physics D*; **18**(14):2275–2282; 2009a; [arXiv:0905.2502](#).
- Corda, C.; *The European Physical Journal C*; **65**(1-2):257–267; 2009b; [arXiv:1007.4077](#).
- Cox, A.N.; *Allen's Astrophysical Quantities*; New York: Springer-Verlag; fourth edition; 2000.
- Crowder, J. & Cornish, N.J.; *Physical Review D*; **72**(8):083005(10); 2005; [arXiv:gr-qc/0506015](#).
- Cutler, C.; *Physical Review D*; **57**(12):7089–7102; 1998; [arXiv:gr-qc/9703068](#).
- Cutler, C. & Flanagan, E.E.; *Physical Review D*; **49**(6):2658–2697; 1994; [arXiv:gr-qc/9402014](#).
- Damour, T., Iyer, B.R. & Sathyaprakash, B.S.; *Physical Review D*; **62**(8):084036(34); 2000; [arXiv:gr-qc/0001023](#).
- Damour, T. & Vilenkin, A.; *Physical Review D*; **71**(6):063510(13); 2005; [arXiv:hep-th/0410222](#).
- Danzmann, K. & Rüdiger, A.; *Classical and Quantum Gravity*; **20**(10):S1–S9; 2003.
- Darwin, C.; *Proceedings of the Royal Society A: Mathematical, Physical and Engineering Sciences*; **263**(1312):39–50; 1961.
- de Berg, M., Cheong, O., van Kreveld, M. & Overmars, M.; *Computational Geometry: Algorithms and Applications*; Berlin: Springer; third edition; 2008.
- De Felice, A. & Tsujikawa, S.; *Living Reviews in Relativity*; **13**(3); 2010; [arXiv:1002.4928](#).
- de Felice, F.; *Journal of Physics A: Mathematical and General*; **13**(5):1701–1708; 1980.
- de la Calle Pérez, I. et al.; *Astronomy and Astrophysics*; **524**:A50(22); 2010; [arXiv:0709.3268](#).
- Deruelle, N., Sasaki, M. & Sendouda, Y.; *Progress of Theoretical Physics*; **119**(2):237–251; 2008; [arXiv:0711.1150](#).
- Detweiler, S.; *Physical Review D*; **77**(12):124026(15); 2008; [arXiv:0804.3529](#).
- Dewdney, P., Hall, P., Schilizzi, R. & Lazio, T.; *Proceedings of the IEEE*; **97**(8):1482–1496; 2009.
- Dimmelmeier, H., Font, J.A. & Müller, E.; *Astronomy and Astrophysics*; **393**(2):523–542; 2002; [arXiv:astro-ph/0204289](#).
- Dirac, P.A.; *General Theory of Relativity*; Princeton Landmarks in Physics; Princeton, New Jersey: Princeton University Press; 1996.
- Doeleman, S.S. et al.; *Nature*; **455**(7209):78–80; 2008; [arXiv:0809.2442](#).
- Drasco, S. & Hughes, S.; *Physical Review D*; **69**(4):044015(11); 2004; [arXiv:astro-ph/0308479](#).
- Dyer, E. & Hinterbichler, K.; *Physical Review D*; **79**(2):024028; 2009; [arXiv:0809.4033](#).

- Einstein, A.; *The Collected Papers of Albert Einstein*; volume 6; Princeton, New Jersey: Princeton University Press; 1997.
- Emmanoulopoulos, D. et al.; *Monthly Notices of the Royal Astronomical Society*; **415**(2):1895–1906; 2011; [arXiv:1104.0044](#).
- Everitt, C.W.F. et al.; *Space Science Reviews*; **148**(1-4):53–69; 2009.
- Everitt, C.W.F. et al.; *Physical Review Letters*; **106**(22):221101(5); 2011; [arXiv:1105.3456](#).
- Exirifard, Q. & Sheik-Jabbari, M.; *Physics Letters B*; **661**(2-3):158–161; 2008; [arXiv:0705.1879](#).
- Fabian, A.C. et al.; *Monthly Notices of the Royal Astronomical Society*; **429**(4):2917–2923; 2013; [arXiv:1208.5898](#).
- Farr, W.M. et al.; *The Astrophysical Journal*; **741**(2):103(19); 2011; [arXiv:1011.1459](#).
- Faulkner, T., Tegmark, M., Bunn, E.F. & Mao, Y.; *Physical Review D*; **76**(6):063505(10); 2007; [arXiv:astro-ph/0612569](#).
- Feng, H. & Soria, R.; *New Astronomy Reviews*; **55**(5-6):166–183; 2011; [arXiv:1109.1610](#).
- Ferrarese, L. & Ford, H.; *Space Science Reviews*; **116**(3-4):523–624; 2005; [arXiv:astro-ph/0411247](#).
- Ferrarese, L. & Merritt, D.; *The Astrophysical Journal*; **539**(1):L9–L12; 2000; [arXiv:astro-ph/0006053](#).
- Finn, L.S.; *Physical Review D*; **46**(12):5236–5249; 1992; [arXiv:gr-qc/9209010](#).
- Fish, V.L. et al.; *The Astrophysical Journal*; **727**(2):L36(6); 2011; [arXiv:1011.2472](#).
- Flanagan, É.É. & Hedges, S.A.; *Physical Review D*; **57**(8):4535–4565; 1998; [arXiv:gr-qc/9701039](#).
- Frank, J. & Rees, M.J.; *Monthly Notices of the Royal Astronomical Society*; **176**(3):633–647; 1976.
- Freire, P.C.C. et al.; *The Astrophysical Journal*; **675**(1):670–682; 2008; [arXiv:0711.0925](#).
- Gair, J.R., Kennefick, D.J. & Larson, S.L.; *Physical Review D*; **72**(8):084009(20); 2005; [arXiv:gr-qc/0508049](#).
- Gair, J.R., Li, C. & Mandel, I.; *Physical Review D*; **77**(2):024035(23); 2008; [arXiv:0708.0628](#).
- Gallo, L.C. et al.; *Monthly Notices of the Royal Astronomical Society*; **411**(1):607–619; 2011; [arXiv:1009.2987](#).
- Gammie, C.F., Shapiro, S.L. & McKinney, J.C.; *The Astrophysical Journal*; **602**(1):312–319; 2004; [arXiv:astro-ph/0310886](#).
- Gebhardt, K. et al.; *The Astrophysical Journal*; **539**(1):L13–L16; 2000; [arXiv:astro-ph/0006289](#).
- Gebhardt, K. et al.; *The Astrophysical Journal*; **583**(1):92–115; 2003; [arXiv:astro-ph/020943](#).
- Gelman, A., Roberts, G.O. & Gilks, W.R.; in J.M. Bernardo, J.O. Berger, A.P. Dawid & A.F.M. Smith (eds.), *Bayesian Statistics*; Oxford Science Publications; 599–607; Oxford: Clarendon Press; 1996.
- Genzel, R. et al.; *Nature*; **425**(6961):934–937; 2003; [arXiv:astro-ph/0310821](#).
- Ghez, A.M. et al.; *The Astrophysical Journal*; **689**(2):1044–1062; 2008; [arXiv:0808.2870](#).
- Gibbons, G.W. & Hawking, S.W.; *Physical Review D*; **15**(10):2752–2756; 1977.
- Gillessen, S. et al.; *The Astrophysical Journal*; **692**(2):1075–1109; 2009; [arXiv:0810.4674](#).
- Glampedakis, K.; *Classical and Quantum Gravity*; **22**(15):S605–S659; 2005; [arXiv:gr-qc/0509024](#).
- Glampedakis, K., Hughes, S. & Kennefick, D.; *Physical Review D*; **66**(6):064005(12); 2002; [arXiv:gr-qc/0205033](#).
- Glampedakis, K. & Kennefick, D.; *Physical Review D*; **66**(4):044002(33); 2002; [arXiv:gr-qc/0203086](#).
- González, J.A., Sperhake, U., Brügmann, B., Hannam, M. & Husa, S.; *Physical Review Letters*; **98**(9):091101(4); 2007; [arXiv:gr-qc/0610154](#).
- Gradshteyn, I.S. & Ryzhik, I.M.; *Table of Integrals, Series, and Products*; London: Academic Press; sixth edition; 2000.
- Graham, A.W.; *Publications of the Astronomical Society of Australia*; **25**(4):167–175; 2008; [arXiv:0807.2549](#).
- Graham, A.W.; *The Astrophysical Journal*; **746**(1):113(5); 2012; [arXiv:1202.1878](#).
- Graham, A.W. & Driver, S.P.; *The Astrophysical Journal*; **655**(1):77–87; 2007; [arXiv:astro-ph/0607378](#).

- Graham, A.W., Erwin, P., Caon, N. & Trujillo, I.; *The Astrophysical Journal*; **563**(1):L11–L14; 2001; [arXiv:astro-ph/0111152](#).
- Graham, A.W., Onken, C.A., Athanassoula, E. & Combes, F.; *Monthly Notices of the Royal Astronomical Society*; **412**(4):2211–2228; 2011; [arXiv:1007.3834](#).
- Graham, A.W. & Scott, N.; *The Astrophysical Journal*; **764**(2):151(19); 2013; [arXiv:1211.3199](#).
- Greenhill, L.J. et al.; *The Astrophysical Journal*; **590**(1):162–173; 2003; [arXiv:astro-ph/0302533](#).
- Greenhill, L.J., Moran, J.M. & Herrnstein, J.R.; *The Astrophysical Journal*; **481**(1):L23–L26; 1997; [arXiv:astro-ph/9702220](#).
- Grishchuk, L.P.; *Physics-Uspekhi*; **48**(12):1235–1247; 2005; [arXiv:gr-qc/0504018](#).
- Guarnizo, A., Castañeda, L. & Tejeiro, J.M.; *General Relativity and Gravitation*; **42**(11):2713–2728; 2010; [arXiv:1002.0617](#).
- Haario, H., Saksman, E. & Tamminen, J.; *Computational Statistics*; **14**(3):375; 1999.
- Haario, H., Saksman, E. & Tamminen, J.; *Bernoulli*; **7**(2):223–242; 2001.
- Haiman, Z. & Quataert, E.; in A.J. Barger (ed.), *Supermassive Black Holes in the Distant universe*; Astrophysics and Space Science Library; chapter 5, 147–186; Dordrecht: Kluwer Academic Publishers; 2004.
- Hamaus, N. et al.; *The Astrophysical Journal*; **692**(1):902–916; 2009; [arXiv:0810.4947](#).
- Häring, N. & Rix, H.W.; *The Astrophysical Journal*; **604**(2):L89–L92; 2004; [arXiv:astro-ph/0402376](#).
- Harris, F.; *Proceedings of the IEEE*; **66**(1):51–83; 1978.
- Harry, G.M.; *Classical and Quantum Gravity*; **27**(8):084006(12); 2010.
- Hastings, W.K.; *Biometrika*; **57**(1):97–109; 1970.
- Havas, P.; *General Relativity and Gravitation*; **8**(8):631–645; 1977.
- Hawking, S.W.; *Communications in Mathematical Physics*; **25**(2):152–166; 1972a.
- Hawking, S.W.; *Communications in Mathematical Physics*; **25**(2):167–171; 1972b.
- Hellings, R.W. & Downs, G.S.; *The Astrophysical Journal*; **265**(2):L39–L42; 1983.
- Hild, S. et al.; *Classical and Quantum Gravity*; **28**(9):094013(13); 2011; [arXiv:1012.0908](#).
- Hinshaw, G. et al.; 31; 2012; [arXiv:1212.5226](#).
- Hioki, K. & Maeda, K.; *Physical Review D*; **80**(2):024042(9); 2009; [arXiv:0904.3575](#).
- Hlavacek-Larrondo, J., Fabian, A.C., Edge, A.C. & Hogan, M.T.; *Monthly Notices of the Royal Astronomical Society*; **424**(1):224–231; 2012; [arXiv:1204.5759](#).
- Hobbs, G. et al.; *Classical and Quantum Gravity*; **27**(8):084013(10); 2010; [arXiv:0911.5206](#).
- Hobson, M.P., Efstathiou, G. & Lasenby, A.; *General Relativity: An Introduction for Physicists*; Cambridge: Cambridge University Press; 2006.
- Hopman, C., Freitag, M. & Larson, S.L.; *Monthly Notices of the Royal Astronomical Society*; **378**(1):129–136; 2007; [arXiv:astro-ph/0612337](#).
- Hoyle, C.D. et al.; *Physical Review D*; **70**(4):042004(31); 2004; [arXiv:hep-ph/0405262](#).
- Hu, W. & Sawicki, I.; *Physical Review D*; **76**(6):064004(13); 2007; [arXiv:0705.1158](#).
- Hu, W. & White, M.; *New Astronomy*; **2**(4):323–344; 1997; [arXiv:astro-ph/9706147](#).
- Huerta, E.A. & Gair, J.R.; *Physical Review D*; **79**(8):84021(22); 2009; [arXiv:0812.4208](#).
- Hughes, S.; *Physical Review D*; **61**(8):084004(28); 2000; [arXiv:gr-qc/9910091](#).
- Hughes, S.A. & Blandford, R.D.; *The Astrophysical Journal*; **585**(2):L101–L104; 2003; [arXiv:astro-ph/0208484](#).
- Hulse, R.A. & Taylor, J.H.; *The Astrophysical Journal*; **195**(2):L51–L53; 1975.
- Iben, Jr., I. & Tutukov, A.V.; *The Astrophysical Journal Supplement Series*; **54**(2):335–372; 1984.
- Isaacson, R.; *Physical Review*; **166**(5):1263–1271; 1968a.
- Isaacson, R.; *Physical Review*; **166**(5):1272–1280; 1968b.
- Israel, W.; *Physical Review*; **164**(5):1776–1779; 1967.
- Israel, W.; *Communications in Mathematical Physics*; **8**(3):245–260; 1968.

- Israel, W.; in S.W. Hawking & W. Israel (eds.), *Three Hundred Years of Gravitation*; chapter 7, 199–276; Cambridge: Cambridge University Press; 1987.
- Ivanova, N. et al.; *The Astronomy and Astrophysics Review*; **21**(1):59(73); 2013; arXiv:1209.4302.
- Jackson, J.D.; *Classical Electrodynamics*; New York: John Wiley & Sons, Inc.; third edition; 1999.
- Jahnke, K. & Macciò, A.V.; *The Astrophysical Journal*; **734**(2):92(11); 2011; arXiv:1006.0482.
- Jani, K.P., Finn, L.S. & Benacquista, M.J.; 24; 2013; arXiv:1306.3253.
- Jaranowski, P. & Królak, A.; *Living Reviews in Relativity*; **15**(4); 2012.
- Jarosik, N. et al.; *The Astrophysical Journal Supplement Series*; **192**(2):14(15); 2011; arXiv:1001.4744.
- Jaynes, E.T.; *Probability Theory: The Logic of Science*; Cambridge: Cambridge University Press; 2003.
- Jennrich, O. et al.; ‘NGO Revealing a hidden Universe: opening a new chapter of discovery’; Technical report; European Space Agency; Noordwijk; 2011.
- Johannsen, T. & Psaltis, D.; *The Astrophysical Journal*; **716**(1):187–197; 2010a; arXiv:1003.3415.
- Johannsen, T. & Psaltis, D.; *The Astrophysical Journal*; **718**(1):446–454; 2010b; arXiv:1005.1931.
- Johannsen, T. et al.; *The Astrophysical Journal*; **758**(1):30(7); 2012; arXiv:1201.0758.
- Kaiser, J. & Schafer, R.; *IEEE Transactions on Acoustics, Speech and Signal Processing*; **28**(1):105–107; 1980.
- Kamionkowski, M. & Stebbins, A.; *Physical Review D*; **55**(12):7368–7388; 1997; arXiv:astro-ph/9611125.
- Kapner, D. et al.; *Physical Review Letters*; **98**(2):021101(4); 2007; arXiv:hep-ph/0611184.
- Karachentsev, I.D., Karachentseva, V.E., Huchtmeier, W.K. & Makarov, D.I.; *The Astronomical Journal*; **127**(4):2031–2068; 2004.
- Karachentsev, I.D. et al.; *The Astronomical Journal*; **133**(2):504–517; 2007; arXiv:astro-ph/0603091.
- Kato, Y., Miyoshi, M., Takahashi, R., Negoro, H. & Matsumoto, R.; *Monthly Notices of the Royal Astronomical Society*; **403**(1):L74–L78; 2010; arXiv:0906.5423.
- Kawamura, S. et al.; *Classical and Quantum Gravity*; **28**(9):094011(12); 2011.
- Kawamura, S. et al.; *Classical and Quantum Gravity*; **23**(8):S125–S131; 2006.
- Kerner, R., van Holten, J.W. & Colistete, Jr., R.; *Classical and Quantum Gravity*; **18**(22):4725–4742; 2001; arXiv:gr-qc/0102099.
- Kerr, R.; *Physical Review Letters*; **11**(5):237–238; 1963.
- Khoury, J.; 19; 2013; arXiv:1306.4326.
- Khoury, J. & Weltman, A.; *Physical Review D*; **69**(4):044026(15); 2004a; arXiv:astro-ph/0309411.
- Khoury, J. & Weltman, A.; *Physical Review Letters*; **93**(17):171104(4); 2004b; arXiv:astro-ph/0309300.
- King, A.R. & Pringle, J.E.; *Monthly Notices of the Royal Astronomical Society*; **373**(1):L90–L92; 2006; arXiv:astro-ph/0609598.
- King, A.R., Pringle, J.E. & Hofmann, J.A.; *Monthly Notices of the Royal Astronomical Society*; **385**(3):1621–1627; 2008; arXiv:0801.1564.
- King, A. & Nixon, C.; 12; 2013; arXiv:1307.3255.
- Kittel, C.; *Elementary Statistical Physics*; New York: John Wiley & Sons; 1958.
- Koivisto, T.; *Classical and Quantum Gravity*; **23**(12):4289–4296; 2006; arXiv:gr-qc/0505128.
- Komatsu, E. et al.; *The Astrophysical Journal Supplement Series*; **192**(2):18(47); 2011; arXiv:1001.4538.
- Kormendy, J. & Richstone, D.; *Annual Review of Astronomy and Astrophysics*; **33**(1):581–624; 1995.
- Kotake, K., Sato, K. & Takahashi, K.; *Reports on Progress in Physics*; **69**(4):971–1143; 2006.
- Kramer, M. et al.; *New Astronomy Reviews*; **48**(11-12):993–1002; 2004; arXiv:astro-ph/0409379.
- Kramer, M. & Stairs, I.; *Annual Review of Astronomy and Astrophysics*; **46**(1):541–572; 2008.
- Kuroda, K.; *Classical and Quantum Gravity*; **27**(8):084004(8); 2010.
- Kuroda, K. et al.; *International Journal of Modern Physics D*; **08**(05):557–579; 1999.
- Lackey, B.D., Kyutoku, K., Shibata, M., Brady, P.R. & Friedman, J.L.; *Physical Review D*;

- 85(4):044061(21); 2012; [arXiv:1109.3402](#).
- Landau, L.D. & Lifshitz, E.M.; *The Classical Theory of Fields*; Course of Theoretical Physics; Oxford: Butterworth-Heinemann; fourth edition; 1975.
- Langer, N.; *Annual Review of Astronomy and Astrophysics*; 50(1):107–164; 2012; [arXiv:1206.5443](#).
- Larson, S.L., Hellings, R.W. & Hiscock, W.A.; *Physical Review D*; 66(6):062001(7); 2002; [arXiv:gr-qc/0206081](#).
- Larson, S.L., Hiscock, W.A. & Hellings, R.W.; *Physical Review D*; 62(6):062001(10); 2000; [arXiv:gr-qc/9909080](#).
- Lattimer, J.M.; *Annual Review of Nuclear and Particle Science*; 62(1):485–515; 2012; [arXiv:1305.3510](#).
- Le Verrier, U.; *Recherches sur les mouvements de la Planète Herschel (dite Uranus)*; Paris: Bachelier; 1846.
- Le Verrier, U.; *Recherches Astronomiques*; volume V; Paris: Mallet-Bachelier; 1859.
- Li, B. & Barrow, J.D.; *Physical Review D*; 75(8):084010(13); 2007; [arXiv:0701111](#).
- Liddle, A.R. & Lyth, D.H.; *Physics Reports*; 231(1-2):1–105; 1993; [arXiv:astro-ph/9303019](#).
- Lightman, A.P. & Shapiro, S.L.; *The Astrophysical Journal*; 211(1):244–262; 1977.
- Lohfink, A.M. et al.; *The Astrophysical Journal*; 772(2):83(13); 2013; [arXiv:1305.4937](#).
- Lohfink, A.M. et al.; *The Astrophysical Journal*; 758(1):67(11); 2012; [arXiv:1209.0468](#).
- Longair, M.S.; *The Cosmic Century*; Cambridge: Cambridge University Press; 2006.
- Lovelock, D.; *Aequationes Mathematicae*; 4(1-2):127–138; 1970.
- Lovelock, D.; *Journal of Mathematical Physics*; 12(3):498; 1971.
- Lovelock, D.; *Journal of Mathematical Physics*; 13(6):874; 1972.
- Lubini, M., Tortora, C., Näf, J., Jetzer, P. & Capozziello, S.; *The European Physical Journal C*; 71(12):1834(7); 2011; [arXiv:1104.2851](#).
- Lynden-Bell, D.; *Nature*; 223(5207):690–694; 1969.
- Lynden-Bell, D. & Rees, M.J.; *Monthly Notices of the Royal Astronomical Society*; 152(4):461–475; 1971.
- Macchetto, F. et al.; *The Astrophysical Journal*; 489(2):579–600; 1997; [arXiv:astro-ph/9706252](#).
- MacKay, D.J.C.; *Information Theory, Inference and Learning Algorithms*; Cambridge: Cambridge University Press; 2003.
- Madsen, M.S. & Barrow, J.D.; *Nuclear Physics B*; 323(1):242–252; 1989.
- Magorrian, J. et al.; *The Astronomical Journal*; 115(6):2285–2305; 1998; [arXiv:astro-ph/9708072](#).
- Malbon, R.K., Baugh, C.M., Frenk, C.S. & Lacey, C.G.; *Monthly Notices of the Royal Astronomical Society*; 382(4):1394–1414; 2007; [arXiv:astro-ph/0607424](#).
- Marconi, A. & Hunt, L.K.; *The Astrophysical Journal*; 589(1):L21–L24; 2003; [arXiv:astro-ph/0304274](#).
- Martel, K.; *Physical Review D*; 69(4):044025(20); 2004; [arXiv:gr-qc/0311017](#).
- McClintock, J.E. et al.; *Classical and Quantum Gravity*; 28(11):114009(17); 2011; [arXiv:1101.0811](#).
- McKechan, D.J.A., Robinson, C. & Sathyaprakash, B.S.; *Classical and Quantum Gravity*; 27(8):084020(11); 2010; [arXiv:1003.2939](#).
- McWilliams, S.T., Ostriker, J.P. & Pretorius, F.; 11; 2012; [arXiv:1211.5377](#).
- Merritt, D.; 2013; [arXiv:1307.3268](#).
- Merritt, D., Alexander, T., Mikkola, S. & Will, C.M.; *Physical Review D*; 81(6):062002(17); 2010; [arXiv:0911.4718](#).
- Metropolis, N., Rosenbluth, A.W., Rosenbluth, M.N., Teller, A.H. & Teller, E.; *The Journal of Chemical Physics*; 21(6):1087–1092; 1953.
- Metzger, B.D. et al.; *Monthly Notices of the Royal Astronomical Society*; 406(4):2650–2662; 2010; [arXiv:1001.5029](#).
- Meyer, L. et al.; *Science*; 338(6103):84–87; 2012; [arXiv:1210.1294](#).
- Michell, J.; *Philosophical Transactions of the Royal Society of London*; 74:35–57; 1784.
- Miller, J.M.; *Annual Review of Astronomy and Astrophysics*; 45(1):441–479; 2007.

- Miller, M.C.; *Classical and Quantum Gravity*; **26**(9):094031(6); 2009; [arXiv:0812.3028](#).
- Miniutti, G. et al.; *Monthly Notices of the Royal Astronomical Society*; **398**(1):255–262; 2009.
- Misner, C.W., Thorne, K.S. & Wheeler, J.A.; *Gravitation*; New York: W. H. Freeman; 1973.
- Miyoshi, M. et al.; *Nature*; **373**(6510):127–129; 1995.
- Näf, J. & Jetzer, P.; *Physical Review D*; **81**(10):104003(8); 2010; [arXiv:1004.2014](#).
- Näf, J. & Jetzer, P.; *Physical Review D*; **84**(2):024027(7); 2011; [arXiv:1104.2200](#).
- Nakar, E. & Piran, T.; *Nature*; **478**(7367):82–84; 2011; [arXiv:1102.1020](#).
- Nardini, E., Fabian, A.C., Reis, R.C. & Walton, D.J.; *Monthly Notices of the Royal Astronomical Society*; **410**(2):1251–1261; 2011; [arXiv:1008.2157](#).
- Nelemans, G.; *Classical and Quantum Gravity*; **26**(9):094030(10); 2009; [arXiv:0901.1778](#).
- Newman, E.T. et al.; *Journal of Mathematical Physics*; **6**(6):918–919; 1965.
- Newton, I.; *The Principia*; London: University of California Press; 1999.
- Nojiri, S. & Odintsov, S.D.; *International Journal of Geometric Methods in Modern Physics*; **4**(1):115–145; 2007; [arXiv:hep-th/0601213](#).
- Nomoto, K.; *The Astrophysical Journal*; **322**(1):206; 1987.
- Nordström, G.; *Koninklijke Nederlandsche Akademie van Wetenschappen Proceedings*; **20**(7):1076–1091; 1918.
- Nowak, N. et al.; *Monthly Notices of the Royal Astronomical Society*; **403**(2):646–672; 2010; [arXiv:0912.2511](#).
- Nutku, Y.; *The Astrophysical Journal*; **158**(3):991–996; 1969.
- Nuttall, A.; *IEEE Transactions on Acoustics, Speech and Signal Processing*; **29**(1):84–91; 1981.
- Olmo, G.J.; *Physical Review Letters*; **95**(26):261102(4); 2005; [arXiv:gr-qc/0505101](#).
- Olmo, G.J.; *Physical Review D*; **75**(2):023511(8); 2007; [arXiv:gr-qc/0612047](#).
- Olver, F.W.J., Lozier, Daniel, W., Boisvert, R.F. & Clark, C.W. (eds.); *NIST Handbook of Mathematical Functions*; Cambridge: Cambridge University Press; 2010.
- Oppenheimer, J.R. & Volkoff, G.M.; *Physical Review*; **55**(4):374–381; 1939.
- Özel, F. & Psaltis, D.; *Physical Review D*; **80**(10):103003(7); 2009; [arXiv:0905.1959](#).
- Özel, F., Psaltis, D., Narayan, R. & McClintock, J.E.; *The Astrophysical Journal*; **725**(2):1918–1927; 2010; [arXiv:1006.2834](#).
- Özel, F., Psaltis, D., Narayan, R. & Santos Villarreal, A.; *The Astrophysical Journal*; **757**(1):55(13); 2012; [arXiv:1201.1006](#).
- Park, M., Zurek, K.M. & Watson, S.; *Physical Review D*; **81**(12):124008(18); 2010; [arXiv:1003.1722](#).
- Patrick, A.R., Reeves, J.N., Lobban, A.P., Porquet, D. & Markowitz, A.G.; *Monthly Notices of the Royal Astronomical Society*; **416**(4):2725–2747; 2011a; [arXiv:1106.2135](#).
- Patrick, A.R. et al.; *Monthly Notices of the Royal Astronomical Society*; **411**(4):2353–2370; 2011b; [arXiv:1010.2080](#).
- Pechlaner, E. & Sexl, R.; *Communications in Mathematical Physics*; **2**(1):165–175; 1966.
- Peebles, P.J.E. & Ratra, B.; *Reviews of Modern Physics*; **75**(2):559–606; 2003; [arXiv:astro-ph/0207347](#).
- Peng, C.Y.; *The Astrophysical Journal*; **671**(2):1098–1107; 2007; [arXiv:0704.1860](#).
- Perlmutter, S. et al.; *The Astrophysical Journal*; **517**(2):565–586; 1999a; [arXiv:astro-ph/9812133](#).
- Perlmutter, S., Turner, M. & White, M.; *Physical Review Letters*; **83**(4):670–673; 1999b; [arXiv:astro-ph/9901052](#).
- Peskin, M.E. & Schroeder, D.V.; *An Introduction to Quantum Field Theory*; Boulder, Colorado: Westview Press; 1995.
- Peters, P.C.; *Physical Review*; **136**(4B):B1224–B1232; 1964.
- Peters, P.C. & Mathews, J.; *Physical Review*; **131**(1):435–440; 1963.
- Peterson, B.M. et al.; *The Astrophysical Journal*; **632**(2):799–808; 2005; [arXiv:astro-ph/0506665](#).
- Pitjeva, E.V.; in S.A. Klioner, P.K. Seidelmann & M.H. Soffel (eds.), *Proceedings of the International*

- Astronomical Union*; volume 5; 170–178; Cambridge: Cambridge University Press; 2009.
- Pitkin, M., Reid, S., Rowan, S. & Hough, J.; *Living Reviews in Relativity*; **14**(5); 2011; [arXiv:1102.3355](#).
- Poelarends, A.J.T., Herwig, F., Langer, N. & Heger, A.; *The Astrophysical Journal*; **675**(1):614–625; 2008; [arXiv:0705.4643](#).
- Postnov, K.A. & Yungelson, L.R.; *Living Reviews in Relativity*; **9**(6); 2006; [arXiv:astro-ph/0701059](#).
- Press, W.; *Physical Review D*; **15**(4):965–968; 1977.
- Preto, M. & Amaro-Seoane, P.; *The Astrophysical Journal*; **708**(1):L42–L46; 2010; [arXiv:0910.3206](#).
- Prix, R.; in W. Becker (ed.), *Neutron Stars and Pulsars*; Astrophysics and Space Science Library; chapter 24, 651–685; Berlin: Springer; 2009.
- Psaltis, D.; *Living Reviews in Relativity*; **11**(9); 2008; [arXiv:0806.1531](#).
- Psaltis, D., Perrodin, D., Dienes, K.R. & Mocioiu, I.; *Physical Review Letters*; **100**(9):091101(4); 2008; [arXiv:0710.4564](#).
- Punturo, M. et al.; *Classical and Quantum Gravity*; **27**(8):084007(23); 2010.
- Read, J.S. et al.; *Physical Review D*; **79**(12):124033(12); 2009; [arXiv:0901.3258](#).
- Rees, M.J.; *Annual Review of Astronomy and Astrophysics*; **22**(1):471–506; 1984.
- Reid, M.J., Readhead, A.C.S., Vermeulen, R.C. & Treuhaft, R.N.; *The Astrophysical Journal*; **524**(2):816–823; 1999; [arXiv:astro-ph/9905075](#).
- Reid, M.J. et al.; *Astronomische Nachrichten*; **324**(S1):505–511; 2003; [arXiv:astro-ph/0304095](#).
- Reissner, H.; *Annalen der Physik*; **355**(9):106–120; 1916.
- Rekola, R. et al.; *Monthly Notices of the Royal Astronomical Society*; **361**(1):330–336; 2005.
- Rezzolla, L. et al.; *The Astrophysical Journal*; **732**(1):L6(6); 2011; [arXiv:1101.4298](#).
- Riess, A.G. et al.; *The Astronomical Journal*; **116**(3):1009–1038; 1998; [arXiv:astro-ph/9805201](#).
- Riles, K.; *Progress in Particle and Nuclear Physics*; **68**:1–54; 2013; [arXiv:1209.0667](#).
- Riley, K.F., Hobson, M.P. & Bence, S.J.; *Mathematical Methods for Physics and Engineering*; Cambridge: Cambridge University Press; second edition; 2002.
- Rindler, W.; *Relativity: Special, General, and Cosmological*; Oxford: Oxford University Press; second edition; 2006.
- Risaliti, G. et al.; *Nature*; **494**(7438):449–451; 2013.
- Roberts, G.O., Gelman, A. & Gilks, W.R.; *The Annals of Applied Probability*; **7**(1):110–120; 1997.
- Roberts, G.O. & Rosenthal, J.S.; *Statistical Science*; **16**(4):351–367; 2001.
- Roberts, G.O. & Rosenthal, J.S.; *Journal of Applied Probability*; **44**(2):458–475; 2007.
- Robinson, D.C.; *Physical Review Letters*; **34**(14):905–906; 1975.
- Rodríguez-Rico, C.A., Goss, W.M., Zhao, J.H., Gomez, Y. & Anantharamaiah, K.R.; *The Astrophysical Journal*; **644**(2):914–923; 2006; [arXiv:astro-ph/0603023](#).
- Rosquist, K., Bylund, T. & Samuelsson, L.; *International Journal of Modern Physics D*; **18**(03):429–434; 2009; [arXiv:0710.4260](#).
- Rubbo, L.J., Holley-Bockelmann, K. & Finn, L.S.; *The Astrophysical Journal*; **649**(1):L25–L28; 2006; [arXiv:astro-ph/0602445](#).
- Ruffini, R. & Sasaki, M.; *Progress of Theoretical Physics*; **66**(5):1627–1638; 1981.
- Ryan, F.D.; *Physical Review D*; **53**(6):3064–3069; 1996.
- Sathyaprakash, B. et al.; *Classical and Quantum Gravity*; **29**(12):124013(16); 2012; [arXiv:1206.0331](#).
- Sathyaprakash, B. & Schutz, B.F.; *Living Reviews in Relativity*; **12**(2); 2009; [arXiv:0903.0338](#).
- Savorgnan, G. et al.; *12*; 2013; [arXiv:1306.2679](#).
- Scheel, M.A., Shapiro, S.L. & Teukolsky, S.A.; *Physical Review D*; **51**(8):4236–4249; 1995; [arXiv:gr-qc/9411026](#).
- Schmidt, H.J.; *Astronomische Nachrichten: A Journal on all Fields of Astronomy*; **307**(5):339–340; 1986; [arXiv:gr-qc/0106037](#).
- Schmoll, S. et al.; *The Astrophysical Journal*; **703**(2):2171–2176; 2009.

- Schnittman, J.D.; 2013; [arXiv:1307.3542](#).
- Schutz, B.F.; *American Journal of Physics*; **52**(5):412–419; 1984.
- Schutz, B.F.; *Classical and Quantum Gravity*; **28**(12):125023(31); 2011; [arXiv:1102.5421](#).
- Schwarzschild, K.; *Sitzungsberichte der Königlich-Preussischen Akademie der Wissenschaften*; **1916**(7):189–196; 1916.
- Seigar, M.S., Kennefick, D., Kennefick, J. & Lacy, C.H.S.; *The Astrophysical Journal*; **678**(2):L93–L96; 2008; [arXiv:0804.0773](#).
- Sesana, A.; 26; 2013a; [arXiv:1307.4086](#).
- Sesana, A.; *Monthly Notices of the Royal Astronomical Society*; **433**(1):L1–L5; 2013b; [arXiv:1211.5375](#).
- Sesana, A., Vecchio, A. & Colacino, C.N.; *Monthly Notices of the Royal Astronomical Society*; **390**(1):192–209; 2008; [arXiv:0804.4476](#).
- Shapiro, S.L. & Teukolsky, S.A.; *Black holes, white dwarfs and neutron stars*; New York: John Wiley & Sons; 1983.
- Sidery, T., Gair, J.R. & Mandel, I.; ‘in preparation’; 2013.
- Sikora, M., Stawarz, Ł. & Lasota, J.; *The Astrophysical Journal*; **658**(2):815–828; 2007; [arXiv:astro-ph/0604095](#).
- Sołtan, A.; *Monthly Notices of the Royal Astronomical Society*; **200**(1):115–122; 1982.
- Somiya, K.; *Classical and Quantum Gravity*; **29**(12):124007(12); 2012; [arXiv:1111.7185](#).
- Sotiriou, T. & Liberati, S.; *Annals of Physics*; **322**(4):935–966; 2007a; [arXiv:gr-qc/0604006](#).
- Sotiriou, T.P. & Faraoni, V.; *Reviews of Modern Physics*; **82**(1):451–497; 2010; [arXiv:0805.1726](#).
- Sotiriou, T.P. & Faraoni, V.; *Physical Review Letters*; **108**(8):081103(4); 2012; [arXiv:1109.6324](#).
- Sotiriou, T.P. & Liberati, S.; *Journal of Physics: Conference Series*; **68**(1):012022(7); 2007b; [arXiv:gr-qc/0611040](#).
- Springel, V., Frenk, C.S. & White, S.D.M.; *Nature*; **440**(7088):1137–44; 2006; [arXiv:astro-ph/0604561](#).
- Stabile, A.; *Physical Review D*; **82**(6):064021(12); 2010; [arXiv:1004.1973](#).
- Stairs, I.H.; *Living Reviews in Relativity*; **6**(5); 2003; [arXiv:astro-ph/0307536](#).
- Starobinskii, A.A.; *Soviet Astronomy Letters*; **9**(5):302–304; 1983.
- Starobinskii, A.A.; *Soviet Astronomy Letters*; **11**(3):133–136; 1985.
- Starobinsky, A.A.; *Physics Letters B*; **91**(1):99–102; 1980.
- Starobinsky, A.A.; *JETP Letters*; **86**(3):157–163; 2007; [arXiv:0706.2041](#).
- Stein, L.C. & Yunes, N.; *Physical Review D*; **83**(6):064038(19); 2011; [arXiv:1012.3144](#).
- Stelle, K.S.; *General Relativity and Gravitation*; **9**(4):353–371; 1978.
- Stroerer, A. & Vecchio, A.; *Classical and Quantum Gravity*; **23**(19):S809–S817; 2006; [arXiv:astro-ph/0605227](#).
- Tan, Y., Wang, J.X., Shu, X.W. & Zhou, Y.; *The Astrophysical Journal*; **747**(1):L11; 2012; [arXiv:1202.0400](#).
- Tanaka, T., Shibata, M., Sasaki, M., Tagoshi, H. & Nakamura, T.; *Progress of Theoretical Physics*; **90**(1):65–83; 1993.
- Tauris, T.M., Langer, N. & Kramer, M.; *Monthly Notices of the Royal Astronomical Society*; **416**(3):2130–2142; 2011; [arXiv:1103.4996](#).
- Taylor, J.H.; *Classical and Quantum Gravity*; **10**(S):S167; 1993.
- Teyssandier, P.; *Astronomische Nachrichten*; **311**(4):209–212; 1990.
- Teyssandier, P. & Tourrenc, P.; *Journal of Mathematical Physics*; **24**(12):2793–2799; 1983.
- Thim, F. et al.; *The Astronomical Journal*; **127**(4):2322–2343; 2004; [arXiv:astro-ph/0401558](#).
- Thorne, K.S.; *The Astrophysical Journal*; **191**(2):507–519; 1974.
- Thorne, K.S.; in S.W. Hawking & W. Israel (eds.), *Three Hundred Years of Gravitation*; chapter 9, 330–458; Cambridge: Cambridge University Press; 1987.
- Thorne, K.S. & Dykla, J.J.; *The Astrophysical Journal*; **166**(2):L35–L38; 1971.

- Timmes, F.X., Woosley, S.E. & Weaver, T.A.; *The Astrophysical Journal*; **457**(2):834; 1996; [arXiv:astro-ph/9510136](#).
- Tolman, R.C.; *Physical Review*; **55**(4):364–373; 1939.
- Tonry, J.L. et al.; *The Astrophysical Journal*; **546**(2):681–693; 2001; [arXiv:astro-ph/0011223](#).
- Tremaine, S. et al.; *The Astrophysical Journal*; **574**(2):740–753; 2002; [arXiv:astro-ph/0203468](#).
- Trippé, S. et al.; *Monthly Notices of the Royal Astronomical Society*; **375**(3):764–772; 2007; [arXiv:astro-ph/0611737](#).
- Turner, M.; *The Astrophysical Journal*; **216**(2):610–619; 1977.
- Unnikrishnan, C.S.; *International Journal of Modern Physics D*; **22**(1):1341010(18); 2013.
- Vallisneri, M.; *Physical Review D*; **77**(4):042001(20); 2008; [arXiv:gr-qc/0703086](#).
- van der Marel, R.P., Cretton, N., de Zeeuw, P.T. & Rix, H.; *The Astrophysical Journal*; **493**(2):613–631; 1998; [arXiv:astro-ph/9705081](#).
- Vanderveld, R.A., Caldwell, R.R. & Rhodes, J.; *Physical Review D*; **84**(12):123510(10); 2011; [arXiv:1109.3189](#).
- Verolme, E.K. et al.; *Monthly Notices of the Royal Astronomical Society*; **335**(3):517–525; 2002; [arXiv:astro-ph/0201086](#).
- Vilenkin, A.; *Physical Review D*; **32**(10):2511–2521; 1985.
- Volonteri, M.; *The Astronomy and Astrophysics Review*; **18**(3):279–315; 2010; [arXiv:1003.4404](#).
- Volonteri, M., Haardt, F. & Madau, P.; *The Astrophysical Journal*; **582**(2):559–573; 2003; [arXiv:astro-ph/0207276](#).
- Volonteri, M., Madau, P., Quataert, E. & Rees, M.J.; *The Astrophysical Journal*; **620**(1):69–77; 2005; [arXiv:astro-ph/0410342](#).
- Volonteri, M. & Natarajan, P.; *Monthly Notices of the Royal Astronomical Society*; **400**(4):1911–1918; 2009; [arXiv:0903.2262](#).
- Volonteri, M., Sikora, M. & Lasota, J.P.; *The Astrophysical Journal*; **667**(2):704–713; 2007; [arXiv:0706.3900](#).
- Wagner, T.A., Schlamming, S., Gundlach, J.H. & Adelberger, E.G.; *Classical and Quantum Gravity*; **29**(18):184002(15); 2012; [arXiv:1207.2442](#).
- Wald, R.M.; *General Relativity*; Chicago: University Of Chicago Press; 1984.
- Walton, D.J., Nardini, E., Fabian, A.C., Gallo, L.C. & Reis, R.C.; *Monthly Notices of the Royal Astronomical Society*; **428**(4):2901–2920; 2013; [arXiv:1210.4593](#).
- Wands, D.; *Classical and Quantum Gravity*; **11**(1):269–279; 1994; [arXiv:gr-qc/9307034](#).
- Watson, G.N.; *A Treatise on the Theory of Bessel Functions*; Cambridge Mathematical Library; Cambridge: Cambridge University Press; second edition; 1995.
- Webbink, R.F.; *The Astrophysical Journal*; **277**(1):355–360; 1984.
- Weinberg, M.D.; *Bayesian Analysis*; **7**(3):737–770; 2012; [arXiv:0911.1777](#).
- Weisberg, J.M., Nice, D.J. & Taylor, J.H.; *The Astrophysical Journal*; **722**(2):1030–1034; 2010; [arXiv:1011.0718](#).
- White, S.D.M. & Rees, M.J.; *Monthly Notices of the Royal Astronomical Society*; **183**:341–358; 1978.
- Wilkins, D.; *Physical Review D*; **5**(4):814–822; 1972.
- Will, C.M.; *Theory and experiment in gravitational physics*; Cambridge: Cambridge University Press; revised edition; 1993.
- Will, C.M.; *Living Reviews in Relativity*; **9**(3); 2006; [arXiv:gr-qc/0510072](#).
- Williams, J.G., Turyshev, S.G. & Boggs, D.H.; *Classical and Quantum Gravity*; **29**(18):184004(11); 2012; [arXiv:1203.2150](#).
- Willke, B. et al.; *Classical and Quantum Gravity*; **23**(8):S207–S214; 2006.
- Willke, B. et al.; *Classical and Quantum Gravity*; **19**(7):1377–1387; 2002.
- Woosley, S.E., Heger, A. & Weaver, T.A.; *Reviews of Modern Physics*; **74**(4):1015–1071; 2002.

- Yagi, K. & Seto, N.; *Physical Review D*; **83**(4):044011(14); 2011; [arXiv:1101.3940](https://arxiv.org/abs/1101.3940).
- Yang, L., Lee, C.C. & Geng, C.Q.; *Journal of Cosmology and Astroparticle Physics*; **2011**(08):029(15); 2011; [arXiv:1106.5582](https://arxiv.org/abs/1106.5582).
- York, J.W.; *Physical Review Letters*; **28**(16):1082–1085; 1972.
- Yu, Q. & Tremaine, S.; *Monthly Notices of the Royal Astronomical Society*; **335**(4):965–976; 2002; [arXiv:astro-ph/0203082](https://arxiv.org/abs/astro-ph/0203082).
- Yunes, N. & Siemens, X.; 119; 2013; [arXiv:1304.3473](https://arxiv.org/abs/1304.3473).
- Yunes, N.N., Sopuerta, C.F., Rubbo, L.J. & Holley-Bockelmann, K.; *The Astrophysical Journal*; **675**(1):604–613; 2008; [arXiv:0704.2612](https://arxiv.org/abs/0704.2612).
- Yusef-Zadeh, F., Choate, D. & Cotton, W.; *The Astrophysical Journal*; **518**(1):L33–L35; 1999; [arXiv:astro-ph/9904142](https://arxiv.org/abs/astro-ph/9904142).
- Zhao, G.B., Li, B. & Koyama, K.; *Physical Review Letters*; **107**(7):071303(4); 2011; [arXiv:1105.0922](https://arxiv.org/abs/1105.0922).
- Zoghbi, A. et al.; *Monthly Notices of the Royal Astronomical Society*; **401**(4):2419–2432; 2010; [arXiv:0910.0367](https://arxiv.org/abs/0910.0367).
- Zwicky, F.; *The Astrophysical Journal*; **86**(3):217–246; 1937.